DOE- NFE-14-6423

SORPTION MODELING AND VERIFICATION FOR OFF-GAS TREATMENT

Final Report: For the period October 1, 2014- September 30, 2016

Prepared for:

U.S. Department of Energy Nuclear Energy University Program
NEUP Integration Office
Center for Advanced Energy Studies
P.O. Box 1625
Idaho Falls, ID 83415

Contract No.: NFE-14-6423
Program Manager: R.T. Jubin

Prepared by:

Lawrence L. Tavlarides
Yue Nan
Department of Biomedical and Chemical Engineering
Syracuse University

Sotira Yiacoumi
Costas Tsouris
Austin Ladshaw
School of Civil and Environmental Engineering
Georgia Institute of Technology

Jorge Gabitto
Chemical Engineering Department
Prairie View A&M University

David DePaoli
Nuclear Security and Isotope Technology Division
Oak Ridge National Laboratory

December 20, 2016

SUMMARY

This project was successfully executed to provide valuable adsorption data and improve a comprehensive model developed in previous work by the authors. Data obtained were used in an integrated computer program to predict the behavior of adsorption columns. The model is supported by experimental data and has been shown to predict capture of off gas similar to that evolving during the reprocessing of nuclear waste. The computer program structure contains (a) equilibrium models of off-gases with the adsorbate; (b) mass-transfer models to describe off-gas mass transfer to a particle, diffusion through the pores of the particle, and adsorption on the active sites of the particle; and (c) incorporation of these models into fixed bed adsorption modeling, which includes advection through the bed. These models are being connected with the MOOSE (Multiphysics Object-Oriented Simulation Environment) software developed at the Idaho National Laboratory through DGOSPREY (Discontinuous Galerkin Off-gas SeParation and REcoverY) computer codes developed in this project.

Experiments for iodine and water adsorption have been conducted on reduced silver mordenite (Ag^0Z) for single layered particles. Adsorption apparatuses have been constructed to execute these experiments over a useful range of conditions for temperatures ranging from ambient to 250 ^oC and water dew points ranging from -69 to 19 ^oC. Experimental results were analyzed to determine mass transfer and diffusion of these gases into the particles and to determine which models best describe the single and binary component mass transfer and diffusion processes. The experimental results were also used to demonstrate the capabilities of the comprehensive models developed to predict single-particle adsorption and transients of the adsorption-desorption processes in fixed beds.

Models for adsorption and mass transfer have been developed to mathematically describe adsorption kinetics and transport via diffusion and advection processes. These models were built on a numerical framework for solving conservation law problems in one-dimensional geometries such as spheres, cylinders, and lines. Coupled with the framework are specific models for adsorption in commercial adsorbents, such as zeolites and mordenites. Utilizing this modeling approach, the authors were able to accurately describe and predict adsorption kinetic data obtained from experiments at a variety of different temperatures and gas phase concentrations. A demonstration of how these models, and framework, can be used to simulate adsorption in fixed-bed columns is provided.

The CO_2 absorption work involved modeling with supportive experimental information. A dynamic model was developed to simulate CO_2 absorption using high alkaline content water solutions. The model is based upon transient mass and energy balances for chemical species commonly present in CO_2 absorption. A computer code was developed to implement CO_2 absorption with a chemical reaction model. Experiments were conducted in a laboratory scale column to determine the model parameters. The influence of geometric parameters and operating variables on CO_2 absorption was studied over a wide range of conditions. Continuing work could employ the model to control column operation and predict the absorption behavior under various input conditions and other prescribed experimental perturbations.

The value of the validated models and numerical frameworks developed in this project is that they can be used to predict the sorption behavior of off-gas evolved during the reprocessing of nuclear waste and thus reduce the cost of the experiments. They can also be used to design sorption processes based on concentration limits and flow-rates determined at the plant level.

Contents

ADSORPTION.....1

1. EXPERIMENTAL STUDIES ON REMOVAL OF RADIOACTIVE IODINE AND TRITIATED WATER SURROGATES FROM OFF-GASES BY SILVER MORDENITE.1

1.1 KEY PERSONNEL.....1
1.2 SCOPE.....1
1.3 I_2 ADSORPTION ON SILVER MORDENITE.....1
1.3.1 Introduction.....1
1.3.2 Experimental setup and materials.....2
1.3.3 Experimental conditions and procedure.....5
1.3.4 Determination of reduction conditions.....5
1.3.5 Adsorption isotherms for I_2 adsorption on Ag^0Z.....8
1.3.6 Adsorption kinetics for I_2 adsorption on Ag^0Z.....11
1.3.6.1 Iodine uptake curves.....11
1.3.6.2 The Shrinking Core Model.....12
1.3.6.3 The effect of superficial gas velocity.....14
1.3.6.4 Modeling Results.....16
1.4 WATER ADSORPTION ON SILVER MORDENITE.....19
1.4.1 Introduction.....19
1.4.2 Experimental setup.....20
1.4.3 Isotherms of water adsorption on Ag^0Z.....21
1.4.4 Kinetics of water adsorption on Ag^0Z.....*25*
1.4.4.1 The uptake curves.....25
1.4.4.2 The Shrinking Core Model and Linear Driving Force Model.....25
1.4.4.2 Modeling results.....26
1.5 CO-ADSORPTION OF I_2 AND H_2O ON SILVER MORDENITE.....29
1.5.1 Experimental system and conditions......29
1.5.2 Uptake curves and isotherms of iodine and water co-adsorption.....30
1.5.3 Impact of water on I_2 adsorption capacity of Ag^0Z.....32
1.6 CONCLUSIONS.....33
1.7 ACKNOWLEDGMENTS.....34
1.8 REFERENCES.....34

2. MODELING OF ADSORPTION PROCESSES FOR OFF-GAS TREATMENT.....39

2.1 KEY PERSONNEL.....39
2.2 SCOPE.....39
2.3 MODELING APPROACH.....39
2.3.1 Introduction.....39

2.3.2 Model Framework 41
2.3.3 Models for Specific Systems 46
2.3.3.1 Bi-porous Pellet Kinetics 46
2.3.3.2 Mass and Energy Transport in Fixed Beds 47
2.3.4 Estimating Model Parameters 49
2.3.5 Equilibria Isotherm Model 51
2.4 KINETIC ADSORPTION DATA ACQUISITION AT SU 51
2.4.1 Adsorbents 51
2.4.2 Description of experimental systems and procedure 52
2.5 MODELING RESULTS 53
2.5.1 Kinetics of H_2O on MS3A: Optimization and Prediction 53
2.5.2 Kinetics of I_2 on Ag^0Z: Model Predictions 55
2.5.3 Fixed-bed Column Modeling 57
2.6 DISCUSSION 60
2.6.1 Kinetics of H_2O on MS3A 60
2.6.2 Kinetics of I_2 on Ag^0Z 62
2.6.3 Fixed-bed Column Modeling 62
2.7 CONCLUSIONS 63
2.8 ACKNOWLEDGMENTS 63
2.9 REFERENCES 63

ABSORPTION 68

3. CARBON DIOXIDE ABSORPTION 68

3.1 KEY PERSONNEL 68
3.2 SCOPE 68
3.3 TASK AND DESCRIPTION OF MAJOR MILESTONES: 68
3.4 THEORETICAL DERIVATION 68
3.4.1 Introduction 68
3.4.2 Kinetic Studies 69
3.4.2.1 Reaction Scheme 71
3.4.2.2 Mass Transfer Model 76
3.5 RESULTS AND DISCUSSION 78
3.5.1 Simulation Results 78
3.6 CONCLUSIONS 85
3.7 REFERENCES 85

ADSORPTION

Experiments and model development were conducted in parallel by the Syracuse University and Georgia Institute of Technology teams, respectively, in collaboration with Oak Ridge National Laboratory and Idaho National Laboratory scientists. Experimental work is discussed in the first section of the report and followed by model development and verification using some of the experimental results generated herein and other data in the literature.

1. Experimental studies on removal of radioactive iodine and tritiated water surrogates from off-gases by silver mordenite

1.1 Key personnel

Lawrence L. Tavlarides (PI), Yue Nan (Ph.D Student), Syracuse University

1.2 Scope

The objective of this portion of the project was to obtain fundamental equilibrium and kinetic data for model development of adsorption of radioactive iodine and tritiated water by reduced silver mordenite (Ag^0Z). Adsorption experiments were conducted to collect fundamental data for mechanisms to incorporate and parameters to utilize in dynamic models. Single-component adsorption equilibrium data were obtained to determine the saturation capacity and evaluate the thermodynamic parameters. Kinetic data were obtained to determine the intraparticle mass transfer and reaction parameters for the complex adsorption models. Desorption studies were performed to distinguish the chemisorption and physisorption capabilities of the reduced silver mordenite. Data acquisition was closely coordinated with the collaborating team and transmitted to them as the data became available for parameter evaluation and model development and refinement.

1.3 I_2 adsorption on silver mordenite (this material has been published[35])

1.3.1 Introduction

Radioactive iodine (^{129}I) is one of the major volatile radionuclides released in the off-gas streams of spent nuclear fuel reprocessing facilities.[1-7] The adverse impact of its radioactivity on human health and long half-life (15.7 million years) make the removal and immobilization of gaseous ^{129}I crucial. The U.S. Environment Protection Agency (EPA) and Nuclear Regulatory Commission (NRC) have issued regulatory emission limits of radioactive elements.

The use of solid adsorbents to remove gaseous iodine has been studied for decades. Compared to liquid scrubbers for iodine removal, solid adsorbent systems have a less complicated system design and lower maintenance costs. Studies on activated carbon, macro reticular resins, silver impregnated alumina silicates, silver nitrate impregnated silicic acid (AC-6120) and silver exchanged molecular sieves have shown potential as alternatives to liquid

scrubbers.[8-19] However, not all of these adsorbents are good options for iodine retention under off-gas conditions. For example, activated carbon does not perform well at high temperatures as it has a relatively low ignition point, and it loses iodine adsorption capacity with the presence of NO and NO_2 in off-gas streams. In addition, the reaction of carbon with NO_x may form unstable and explosive compounds which are totally undesired.[11-12,20] Among these studied systems, hydrogen-reduced silver-exchanged mordenite (Ag^0Z) was reported as state-of-art for iodine retention and unreduced AgZ is commercially available. Mordenite has a high silicon-aluminum ratio (typically 5:1), and therefore is thermally stable at high temperatures and resistant to acidic off-gas streams. Even though studies[21-22] have shown that other chemical forms exist in addition to the major form (AgI), when iodine is adsorbed into Ag zeolites, the stronger Ag-I chemical bond makes AgZ preferred over adsorbents that adsorb iodine molecules physically.

The removal of iodine with Ag^0Z has been studied since the 70's, however the micro-scale adsorption process and detailed kinetics remain unexplored. Staple et al.[23] and Thomas et al.[24] first investigated the maximum iodine loading capacity of the reduced and unreduced AgZ via column tests, and found that the reduced Ag^0Z performed better than the unreduced form. They also reported the optimal adsorption temperature of 423 K. A number of investigations have been performed at U.S. National Laboratories[13-18, 21-28] and significant data were obtained. Adsorption capabilities and decontamination factors (DF) of Ag^0Z deep beds were determined at various conditions. The results show that Ag^0Z columns are able to achieve the DFs that meet the regulatory requirements.

To gain further understanding of the system, iodine adsorption experiments were conducted on single-layer Ag^0Z pellets in continuous-flow adsorption systems of high precision at temperatures of 373 – 523 K and iodine concentrations of 9 – 52 ppmv. Equilibrium and kinetic data of adsorption were obtained for capacity evaluation and studying the kinetics of the adsorption process. Desorption data obtained were used to distinguish the contribution of physisorption and chemisorption. The impact of temperature on the equilibrium iodine loading was evaluated. Kinetic data were analyzed by the Shrinking Core kinetic model and the model parameters associated with mass transfer and reaction processes were determined. In addition, the primary controlling mechanisms were determined based on the modeling results. Obtained data and model parameters were also sent to the collaborating research group at GIT for modelling development and verification.

1.3.2 Experimental setup and materials

The IONEX-TYPE AgZ (Ag-900 E16, Lot# 111515-1) was purchased from Molecular Products, Inc. The AgZ pellets are cylindrical extrudates with an average diameter of 1.6 mm as indicated by the supplier. The actual size of the pellets as received distributed between 10 and 16 mesh, and was further narrowed down with a 12-mesh stainless steel screen to 1.8 mm (average equivalent spherical diameter). The diameter was obtained by calculating the diameter of a sphere of equivalent volume to the cylindrical AgZ pellet. The Ag^0Z was prepared by reduction in 4% H_2 /96% Argon. The physical properties and characteristics of the Ag^0Z reduced at optimal conditions are shown in **Table 1**. The average silver content as indicated by the supplier was 11.9 wt. %, which is 12.0 wt.% (1.10 mmol Ag/g) on dry basis, and the result of the inductively coupled plasma optical emission spectrometer (ICP-OES) performed in this study indicated the approximate formula of $Ag_{4.09}Na_{0.64}Ca_{0.31}K_{0.70}Fe_{0.65}(AlO_2)_{8.21}(SiO_2)_{43.26} \cdot xH_2O$. In theory, if all

of the 12.0 wt. % (1.10 mmol Ag/g) silver was reacted with iodine through the reaction $2Ag + I_2 \rightarrow 2AgI$ to form AgI, the theoretical maximum iodine adsorption capacity of the Ag^0Z would be 14.1 wt. % (1.10 mmol I /g). It is noted that before reduction Ag is largely in the crystalline framework of AgZ as $Ag^+_x (AlO_4)^{-1}_x (SiO_2)_{5x}$ and that after reduction in hydrogen at 673 K for 24 hours or more severe conditions, Ag was shown to be reduced to Ag^0 by XRD and XAFS analysis.[29-33]

Table 1. Properties and characteristics of Ag^0Z

Property/Characteristic	Value
Moisture in AgZ as received (wt. %)	1.2[a]
Silver content as received (wt. %)	11.9[a]
Theoretical maximum iodine capacity (wt. %)	14.0
Equivalent diameter of pellets (mm)	1.8[b]
Porosity	0.384[b]
Pellet density (g/cm^3)	3.057±0.06[b]

[a] Provided by supplier
[b] Measured in this study

Scanning electron microscopy (SEM) (JEOL 5600, JEOL, Dearborn, MA) was performed to observe the changes in the morphology of AgZ crystals by hydrogen reduction. Images of AgZ and Ag^0Z using secondary electron imaging (SEI) were obtained at high magnifications. Energy dispersive X-ray spectroscopy (EDX) analysis was also performed with the SEM system to obtain qualitative information of elemental compositions of AgZ and Ag^0Z surfaces. The porosity and density were determined by mercury porosimetry analysis at Porous Materials, Inc. Ithaca, NY.

The iodine uptake experiments were performed in two identical continuous-flow adsorption systems described previously.[34, 35] A schematic diagram of one system is shown in **Figure 1**. Each of the systems was comprised of an iodine generation unit, a microbalance unit, a furnace and a data acquisition system. Molecular iodine vapors were generated by the dynacalibrators (VICI, Model 450 and 500). By varying the temperature of the dynacalibrator and flow rates of the carrier and dilution streams, the concentrations of iodine in the gas stream (9 – 52 ppmv) were precisely controlled. A microbalance with a sensitivity of 0.1 ug was used in each system to measure the mass change of adsorbents. A stainless steel screen tray inside a glass adsorption column was suspended from the microbalance and loaded with a single-layer of Ag^0Z pellets. The glass column (I.D.: 30mm) was wrapped with glass coils, through which the flowing gas stream was pre-heated. There were two thermocouples both inside and outside of the column to ensure the gas was preheated to the desired adsorption temperature. A furnace with an accuracy of 0.1 K was used in each system for desired temperatures. Photographs of the iodine adsorption systems, and details of the adsorption column and the screen tray with Ag^0Z loaded are shown in **Figure 2**. More details of the microbalance and adsorption column were described previously.[36, 37]

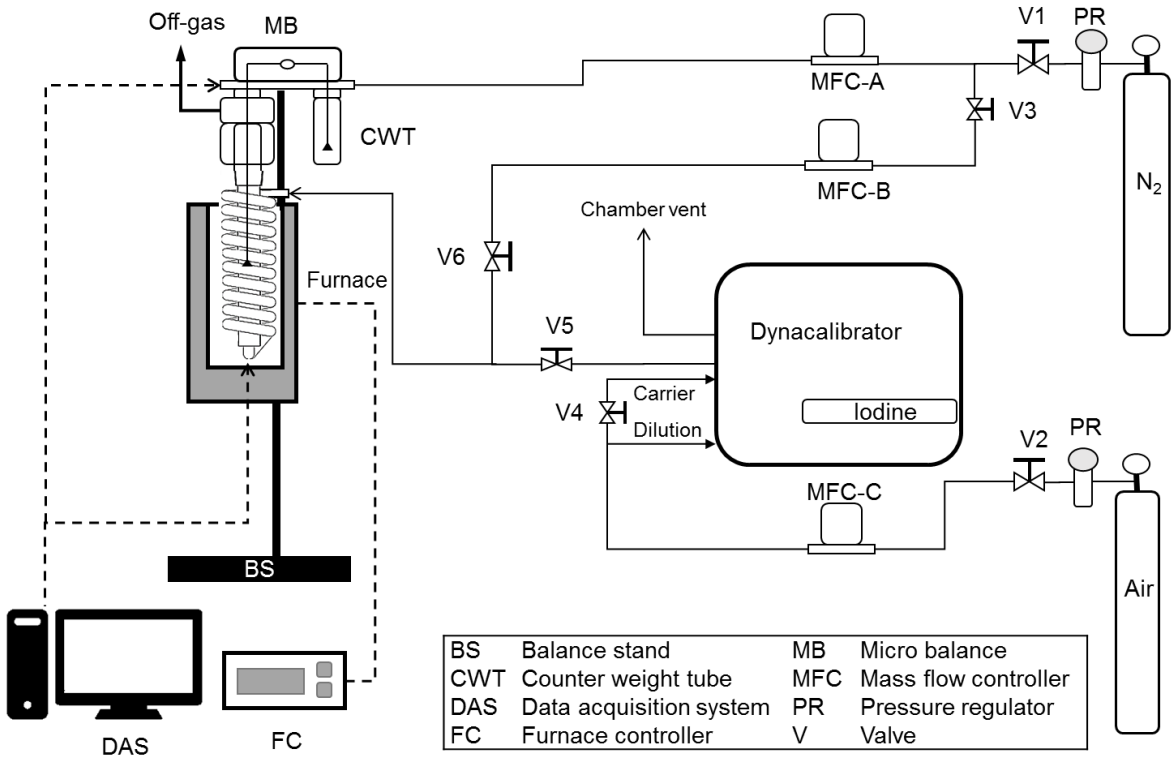

Figure 1. Schematic diagram of the continuous-flow iodine adsorption system.

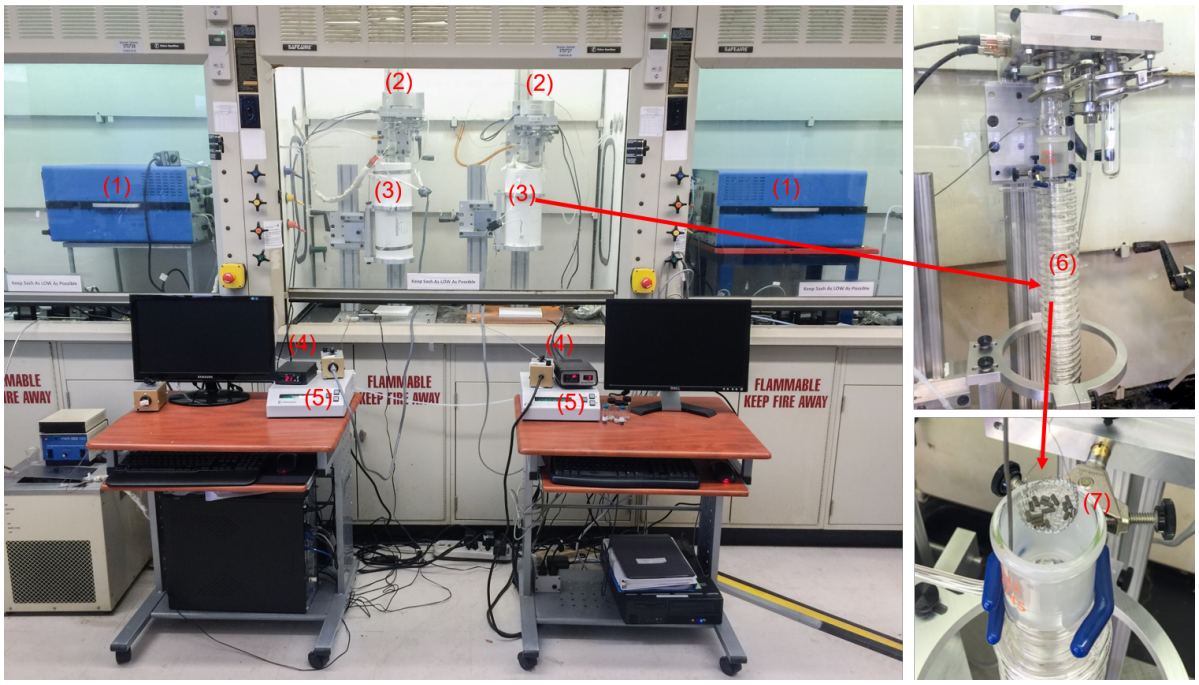

Figure 2. Photographs of the iodine adsorption systems. (1). Dynacalibrator; (2). Microbalance; (3). Furnace; (4). Temperature controller; (5). Data collection system; (6). Adsorption column with preheating coil inside the furnace; (7). Stainless steel screen tray with Ag^0Z loaded.

1.3.3 Experimental conditions and procedure

Wide ranges of reduction temperatures (443 – 773 K) and reduction times (24 – 336 hours) were studied to determine the optimal reduction conditions. At each set of conditions, about 10 g of AgZ were first pretreated with N_2 (500 ml/min) for 4 hours at the reduction temperature to remove the residual moisture in the pellets, and then reduced with 4% H_2/96% Argon at the same flow rate for the desired period of time. After reduction, the pellets were purged with N_2 to remove the residual H_2 inside the pellets and cooled down.

The iodine capacities of Ag^0Z reduced at different conditions were determined and compared using two batch experimental systems. The two systems had unique humidity and temperature. Ag^0Z samples were first equilibrated with water (moisture in the air) in one system, and then were transferred to the other system for iodine adsorption. There were four stainless steel screen trays suspended in each system which are resistant to I_2 adsorption. Therefore, four samples could be compared in each experiment. Before batch experiments, the Ag^0Z samples were degassed using an ASAP 2020 Physisorption Analyzer under vacuum at 473 K for 8 hours to remove residual water prior to the experiments. Samples were weighed initially and loaded onto the screen trays in one of the batch systems for pre-equilibration with water. They were weighed every 24 hours until no further weight gain was observed, and then were transferred to the other batch system for iodine adsorption.

The iodine adsorption experiments were conducted at conditions: I_2 concentration of 9-52 ppmv and temperature of 373 - 523 K. The gas flow rate studied was between 0.25 to 2 L/min, and the corresponding gas velocity passed through the adsorption column was between 0.55 to 4.4 m/min. About 0.2 g Ag^0Z pellets were carefully loaded not to touch one another. Before iodine adsorption, the pellets were pre-equilibrated in cylinder dry air (with dew point of 203 K) at desired experiment conditions. Then the iodine vapor was introduced to the dry air stream and the total flow rate was adjusted to maintain the same value as before. Desorption experiments subsequently followed by stopping the iodine vapor from the gas stream to determine the amount of physisorbed iodine. The iodine that was not strongly bonded (chemically bonded) to the sorbent was desorbed.

1.3.4 Determination of reduction conditions

The iodine and water loading capacity of Ag^0Z reduced at different conditions were determined by batch experiments for comparison. **Figure 3** shows the water and iodine uptake of one experiment as an example. Ag^0Z samples reduced at 443, 503, 573 and 673 K for 24 hours were first loaded with about 4 wt. % water, and subsequently loaded with iodine. The samples achieved similar weight gain due to the adsorption of water, but the sample reduced at 673 K had the highest iodine loading capacity among the four samples. Similar experiments were performed to determine and compare the capacities of all samples. It was found that all the Ag^0Z samples reduced at different conditions had similar water adsorption capacity.

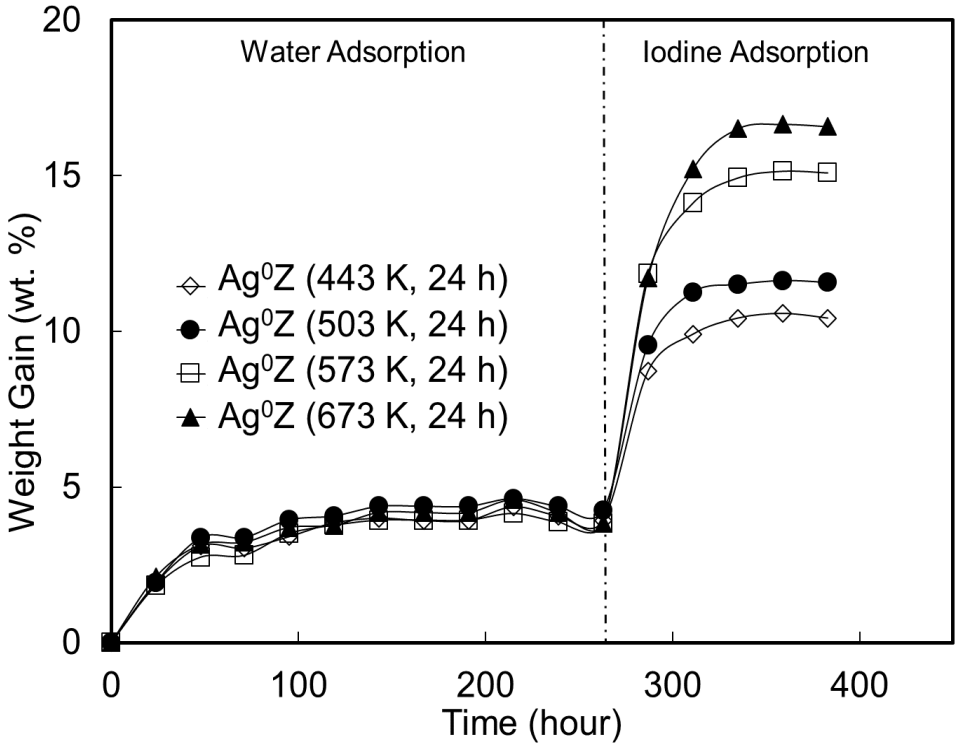

Figure 3. Adsorption of water and iodine on Ag^0Z reduced at 443, 503, 573 and 673 K for 24 hours in the batch experimental system.

The effects of reduction temperature and time on the iodine adsorption capacity are shown in **Figure 4**. As shown in the plots, given the reduction time of 24 hours, the iodine loading capacity of Ag^0Z increased as reduction temperature increased from 443 to 673 K, which indicated that high temperature favors the conversion of Ag^+ to Ag^0 in hydrogen. Further increasing the temperature to 773 K did not increase the capacity. The same tendencies were observed at reduction times of 120 and 336 hours that the increase of iodine loading capacity also leveled off at 673 K. It is also noted that a longer reduction time is needed at low reduction temperatures to achieve the maximum iodine capacity, which is due to the low transformation rate of Ag^+ to Ag^0 rate at low temperatures. The curves indicate that there is no further increase in iodine loading capacity beyond the reduction conditions of 673 K and 24 hours, which indicated that, at these optimal conditions, the AgZ was fully reduced. Therefore, this set of conditions is the optimal reduction conditions for the AgZ used in the current study and is supported by similar studies in the literature.[31, 32]

Previous studies[38, 39] also reported that high temperatures up to 1173 K was required to reduce the Ag in AgZ crystals. The AgZ used in these studies was prepared by ion exchange of commercial NaZ (Si/Al: 6.5:1) in $AgNO_3$ solution, which had different properties to the commercial AgZ pellets (Si/Al: 5:1) used in this study. It is noted that the physisorbed iodine on the samples in the batch experiments at room temperature and saturated iodine vapor pressure, should be more than that in the later continuous-flow experiments at 373 – 523 K and 9 – 52 ppmv under which conditions chemisorption occurs mostly. So the equilibrium iodine loading of the batch experiments is not comparable with that of the continuous-flow experiments.

As mentioned above, silver inside the mordenite crystals migrates to the surface of the crystals and forms silver nanoparticles during the reduction in hydrogen.[31] Since the Ag^0Z in this study was completely reduced at the optimal reduction conditions, the silver is mostly in the form of nanoparticles located on the surface of the mordenite crystals. Therefore, iodine molecules are expected to react with the silver nanoparticles to produce AgI nanoparticles by diffusion through the macro pores between the modenite crystals rather than the micro pores in the mordenite crystals. The microstructure of an Ag^0Z pellet is depicted in **Figure 5**.

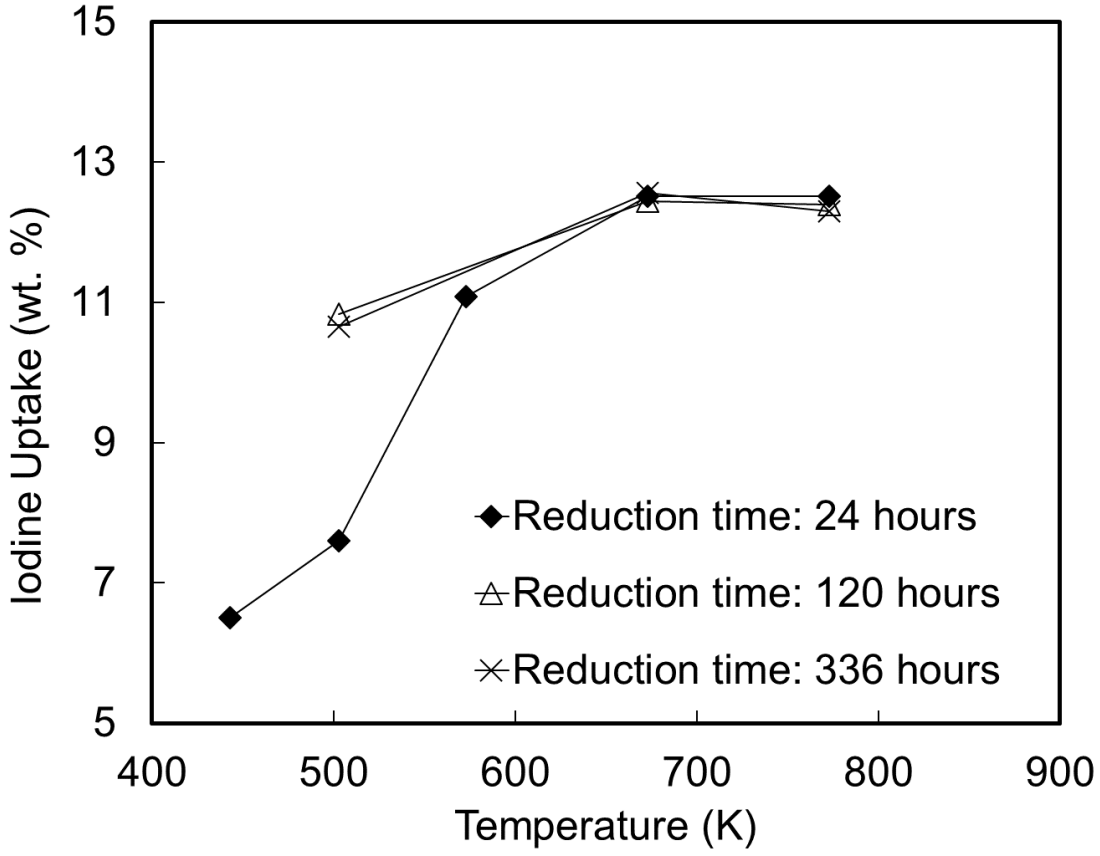

Figure 4. Effect of reduction conditions on the iodine adsorption capacity of Ag0Z.

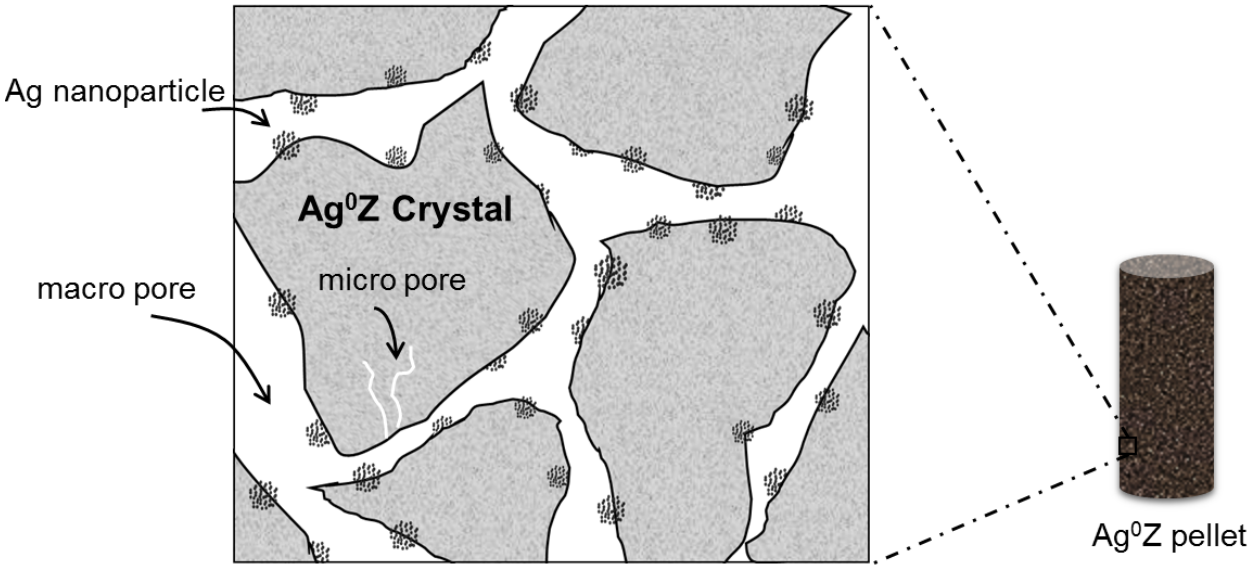

Figure 5. Depiction of silver nanoparticles on the surface of the Ag0Z crystals. Iodine molecules mainly diffuse through the macro pores between the crystals to react with silver nanoparticles.

1.3.5 Adsorption isotherms for I_2 adsorption on Ag^0Z

The equilibrium data of iodine adsorption on Ag^0Z are plotted in **Figure 6**. **Figure 6a** displays the isotherms of total adsorption of iodine with contributions by both physisorption and chemisorption. An average total iodine loading of 13.5 wt. % was achieved at the optimal temperature of 423 K. This optimal adsorption temperature agreed with previous studies. [11-18, 20-24] The linear isotherms show a slight slope, which is mostly due to the increase of physisorbed iodine as the iodine concentration in the gas stream increased. The isotherms of chemisorption shown in **Figure 6b** are almost constant lines that are only affected by the adsorption temperature rather than iodine concentration. The average chemisorption at 423 K is 12.3 wt. %, corresponding to an 88% silver utilization efficiency. The incomplete Ag utilization could be due to the unavailability of the silver in the channels and pores of the crystals that were closed or blocked, so that the silver could not move to the surface of mordenite during the reduction. In addition, the reaction may have reached an equilibrium, so the forward Ag-I reaction is not 100% complete.

It is found that temperature affects the iodine loading capacity of Ag^0Z through the impact on chemisorption (Ag-I reaction). However, the effect of temperature on the iodine loading capacity is not linear. The equilibrium iodine adsorption capacity of Ag^0Z increased as the temperature increased from 373 to 423 K, but decreased when further increased the temperature to 473 K. Theoretically, the equilibrium adsorption capacity is expected to decrease with increasing temperature. The opposite change of iodine loading capacity from 373 K to 423 K could be due to the impact of the water existing in the mordenite structure. Previous studies of iodine adsorption with Ag^0Z[11-16,19,20] have shown that water adsorbed in Ag^0Z has an adverse effect on the iodine capacity of Ag^0Z. They reported that at high temperatures such as 423 K,

there is less adverse effect of water in the off-gas streams compared to low temperatures (room temperature), because the relative vapor pressure of water is lower. Consequently, there is less water present to react with Ag and AgI forming Ag_2O or AgOH. Also water content in the zeolite will be lower permitting I_2 to enter pores or pass between crystals. Accordingly, the negative effect of water at 423K should be lower than that at 373 K. In the single-layer adsorption experiments of this study, the Ag^0Z was pre-equilibrated at desired adsorption conditions in the gas stream without iodine to remove the moisture in the pellets before starting iodine adsorption. In other words, for experiments at 373 K, the Ag^0Z was pre-equilibrated at 373 K, and for experiments at 423 K, the Ag^0Z was pre-equilibrated at 423 K. Therefore, the pre-equilibration at 373 K gave more moisture remaining in Ag^0Z than that at 423 K, and consequently a stronger effect by the water. **Figure 7** shows the desorption (removal) of water when Ag^0Z was equilibrated in the gas stream without iodine at 373, 423 and 473 K, sequentially. As the temperature was increased more water was desorbed, resulted in less effect of the water. Therefore, the iodine capacity at 423 K was higher than 373 K.

However, the less adverse effect of water at a lower temperature cannot explain the decrease in iodine capacity when increasing the temperature from 423 K to 473 K. Extended experiments were conducted at 523K, and a different behavior (**Figure 8**) to those at 373 – 473 K was observed. As anticipated, the iodine capacity at 523K further decreased, but the uptake curve started to drop at the 35-hour point without stopping the iodine in the gas stream. The weight loss was a slow process that took about 200 hours to drop from 7.5 wt. % to 6.5 wt. %. Similar results were obtained from a replicate experiment. Since there were no changes in dew point and iodine concentration in the gas stream during the experiments, desorption of water or iodine should not occur. Therefore, the weight loss should be due to the decomposition of AgI formed on Ag^0Z to release iodine and silver. And this silver may be in some chemical form that could not react with iodine to form AgI again. As more AgI was formed, the rate of decomposition became faster than formation, resulting in the weight loss of adsorbents. After about 200 hours, the formation and decomposition of AgI reached equilibrium. The decomposition also explains the decrease in iodine capacity of Ag^0Z when the temperature was increased from 423 to 473 K. The decrease in iodine capacity due to the decomposition of AgI overcame the increase due to the effect of less water in the Ag^0Z pellets.

However, this observation of decomposition at 523 K varies from those reported in previous studies that bulk AgI and AgI inside zeolite crystals decomposed at temperatures above 773 K.[40-42] In addition, by thermodynamic calculations, equilibrium vapor pressures of I_2 over bulk AgI for the Ag-I reaction at 473 and 523 K in terms of concentration are 0.049 and 0.245 ppm, respectively, which means that AgI decomposition should not occur at the experimental conditions performed where the iodine concentrations were 9- 52 ppmv. The reason could be that the AgI nanoparticles formed on the mordenite crystal surface by iodine reacting with silver nanoparticles are more susceptible to decomposition than bulk AgI and AgI formed inside zeolite crystals. However, future work including chemical analyses is needed to confirm the AgI decomposition in Ag^0Z.

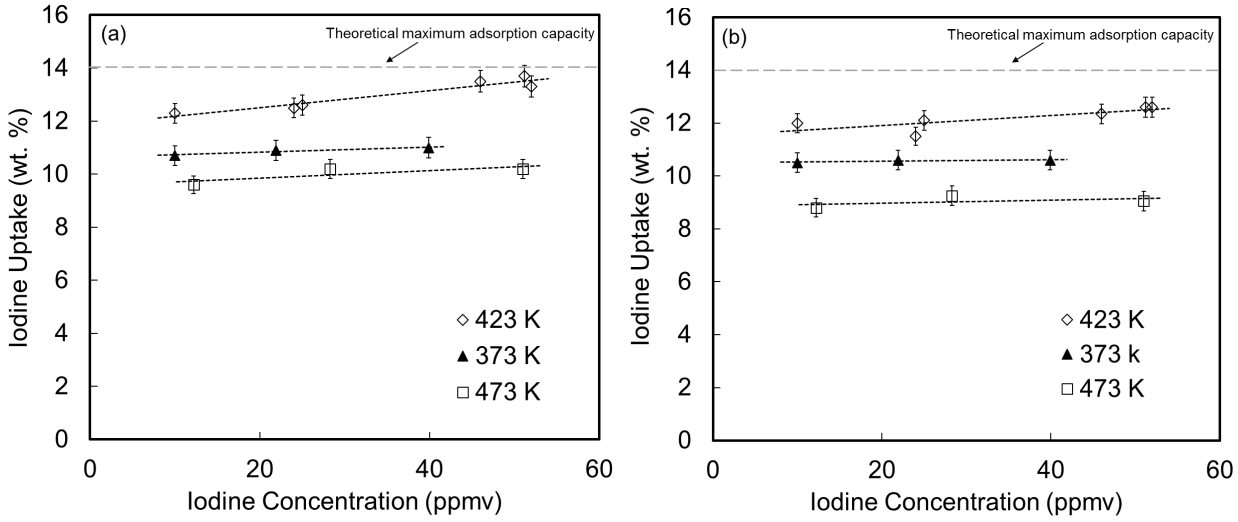

Figure 6. Isotherms of iodine adsorption on Ag0Z. a) Total adsorption; b) Chemisorption.

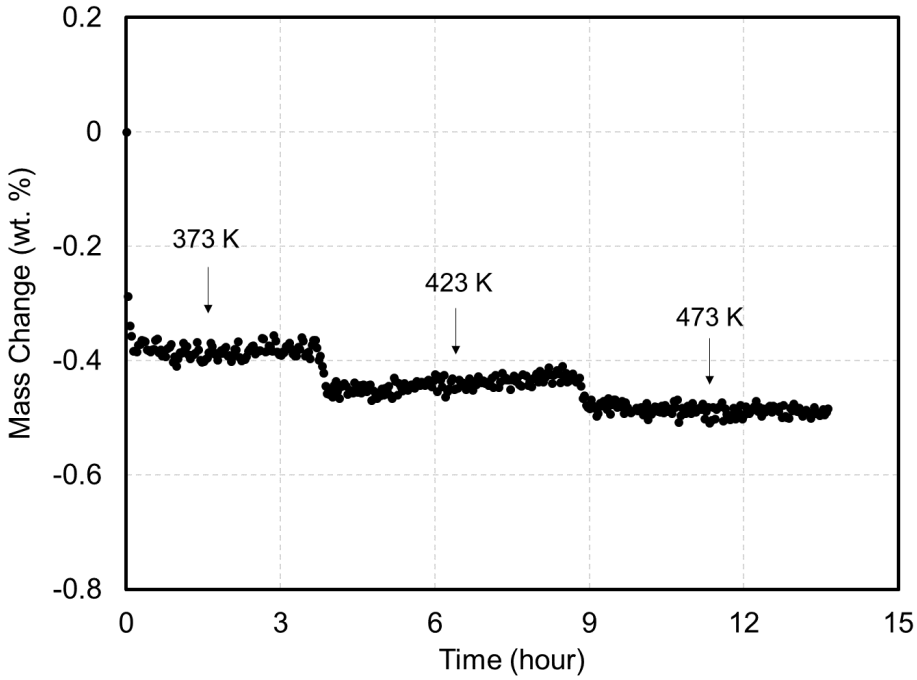

Figure 7. Desorption of water when Ag0Z is equilibrated in the dry air stream (dew point: ~203 K) at 373, 423 and 473 K, sequentially.

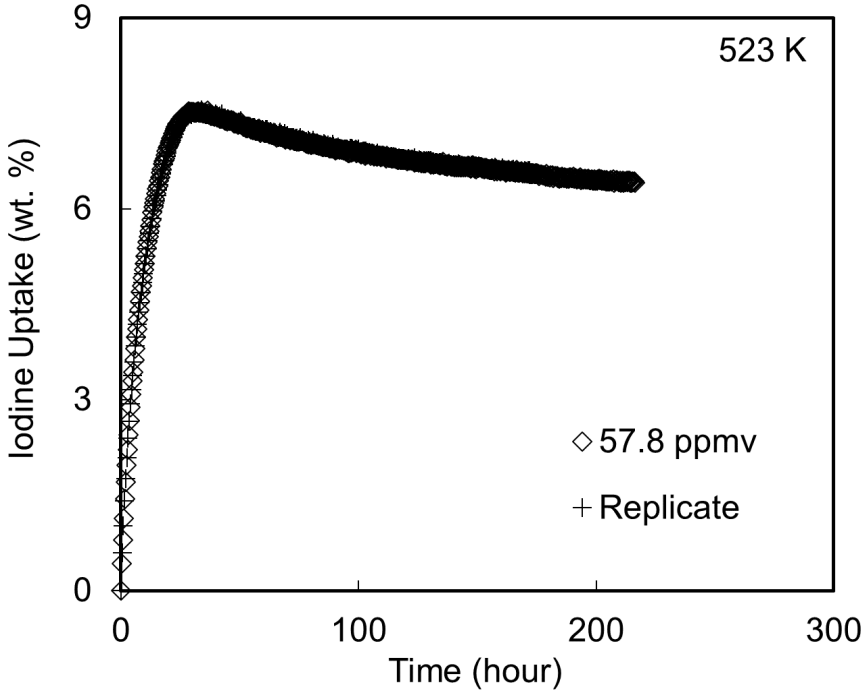

Figure 8. Uptake curves of iodine adsorption on Ag^0Z at 523 K. A decrease in mass is observed from 35 hours without stopping iodine in the gas stream which is due to possible decomposition of AgI.

1.3.6 Adsorption kinetics for I_2 adsorption on Ag^0Z

1.3.6.1 Iodine uptake curves

The iodine uptake curves obtained with the continuous-flow adsorption systems at 373, 423 and 473 K are plotted in **Figure 9**, which take up to 500 hours to reach equilibrium. The iodine uptake rate increased as the iodine concentration increased, but the equilibrium iodine loading did not vary significantly. For instance, at 373 K, the adsorption at 39.9 ppmv took about 130 hours to reach equilibrium while it took about 400 hours at 10 ppmv. However, both adsorptions achieved about 11 wt. % iodine loading at equilibrium, which indicated the adsorption was mostly chemisorption. The color of the pellets changed from gray to yellow which, also indicated that iodine was chemisorbed. At 423 K and with similar iodine concentrations, the iodine loadings were more than 12 wt. %, which indicated that the capacity of the Ag^0Z was mainly impacted by temperature. It is noted that at 423 K there are differences in equilibrium iodine loading at similar iodine concentrations. The deviations could be due to the heterogeneity of the sorbents in pellet size and possible differences in physical/chemical structure between single extruded pellets. Even through multiple pellets were used in the experiments to minimize this impact, minor variations may still exist.

The amount of physisorbed iodine was estimated by desorption experiments assuming that the physisorbed iodine was not strongly bonded with silver and thus was desorbed in the clean

dry air. The fraction of physisorbed iodine to the total adsorbed iodine was found the range from 3% to 9%, which indicated that the adsorption of iodine on Ag^0Z was mostly chemisorption. As expected, the amount of physisorbed iodine increased with iodine concentration.

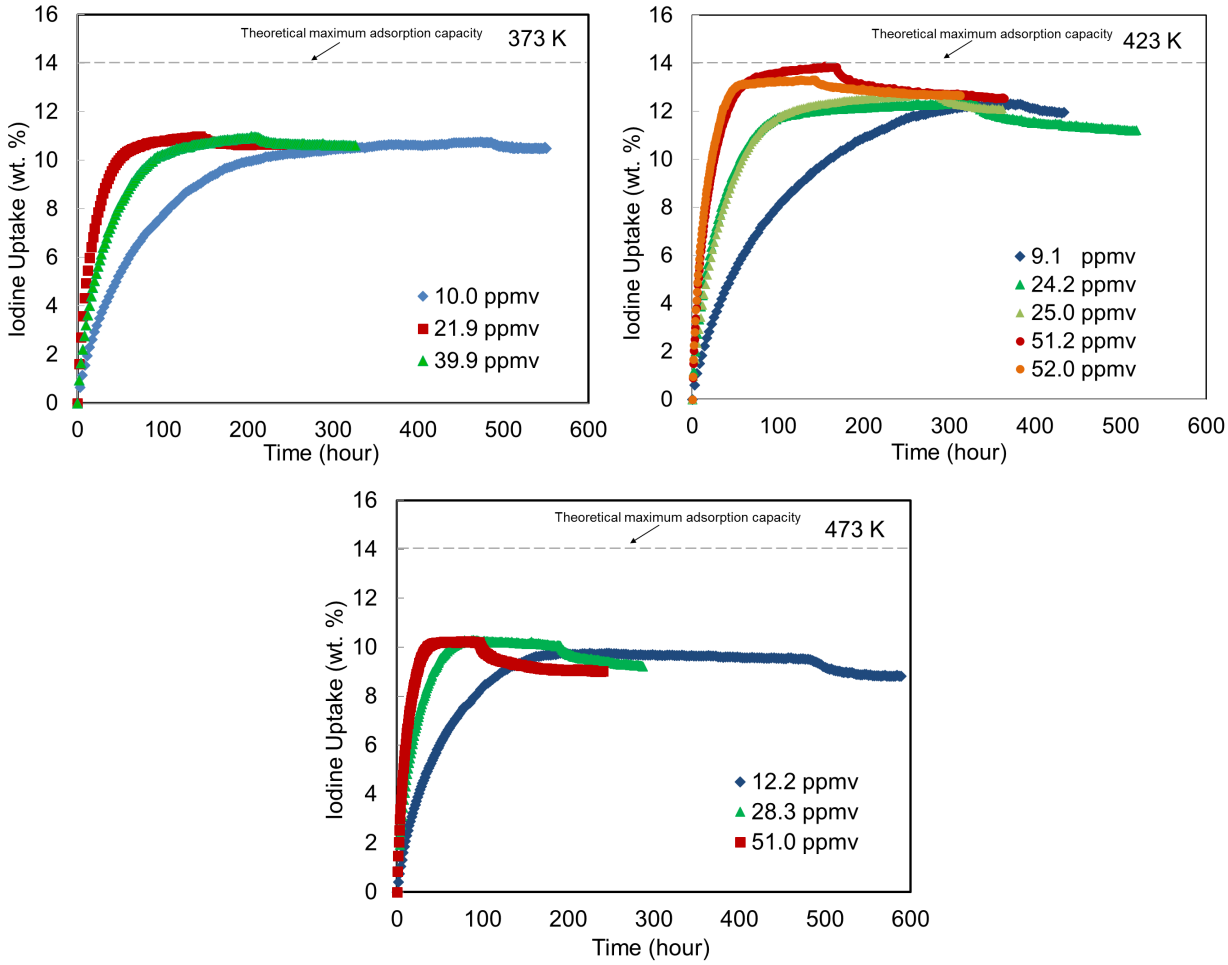

Figure 9. Uptake curves of iodine adsorption on Ag0Z at 373, 423 and 473 K, over iodine concentration between 9 - 52 ppmv.

1.3.6.2 The Shrinking Core Model

Since the iodine adsorption process undergoes both mass transfer and chemical reaction, the Shrinking Core (SC) model was employed to describe the kinetics of iodine adsorption on Ag^0Z. This model has been widely used to describe gas-solid adsorption systems.[37, 43-46] In a previous study,[37] the SC model described adsorption of water on molecular sieves 3A by diffusion through the external gas film and the saturated adsorbent shell. Also, Jubin[46] used this model to predict the adsorption of methyl iodide on Ag^0Z which involved both mass transfer and reaction processes.

The adsorption process described by the SC model includes a) diffusion through the external gas film, b) diffusion through the reacted shell, and c) reaction on the surface of the

unreacted core.[43-45] As adsorption proceeds, the diameter of the unreacted core shrinks. In addition, this model assumes the reaction rate is relatively fast so that there was no significant sorbate concentration gradient near the reacting surface. The model can be expressed in terms of adsorption time, t, by the following Eq. (1):

$$t = \frac{q}{q_e}\tau_1 + \left(1 + 2\left(1 - \frac{q}{q_e}\right) - 3\left(1 - \frac{q}{q_e}\right)^{2/3}\right)\tau_2 + \left(1 - \left(1 - \frac{q}{q_e}\right)^{1/3}\right)\tau_3 \quad (1)$$

where q_e and q are the equilibrium and average transient sorbate concentration (mol/g) in the adsorbent, respectively, and τ_1, τ_2 and τ_3 are the time required to reach equilibrium if the adsorption is controlled by the external gas film mass transfer, pore diffusion and gas-solid reaction, respectively, given by:

$$\tau_1 = \frac{r_a q_e \rho_p}{3bk_g C_A} \quad (2)$$

$$\tau_2 = \frac{r_a^2 q_e \rho_p}{6bD_p C_A} \quad (3)$$

$$\tau_3 = \frac{r_a q_e \rho_p}{bk_s C_A} \quad (4)$$

where r_a and ρ_p denote radius (cm) and density (g/cm^3) of the pellets, respectively, C_A is the bulk gas-phase concentration (mol/cm^3), k_g is the gas film mass transfer coefficient, D_p is the pore diffusivity, k_s is the reaction rate constant assuming the Ag-I reaction is a simple first-order reaction, and b is stoichiometric coefficient of solid reactant in the gas-solid reaction:

$$aA(g) + bB(s) \rightarrow cC(s) + dD(g) \quad (5)$$

which equals 2 in the Ag-I reaction.

To demonstrate the shrinking core process of Ag^0Z adsorbing iodine, a short time adsorption experiment was conducted, which results are shown and compared with a complete adsorption experiment in **Figure 10**. As shown in the figure, the adsorption was performed for about 50 hours and followed with a 50-hour desorption. Then the Ag^0Z was taken out from the experimental system and cut open axially. A comparison of the particles is shown in the inset of **Figure 10**. The particle of the short-time adsorption experimental shows an unreacted core in the center of the particle surrounded by a reached layer/shell. In contrast, the particle from the complete adsorption experiment displays a unique color, which means it was fully reacted. This result demonstrated the shrinking core process with the adsorption going on, which indicated that using the shrinking core model was appropriate.

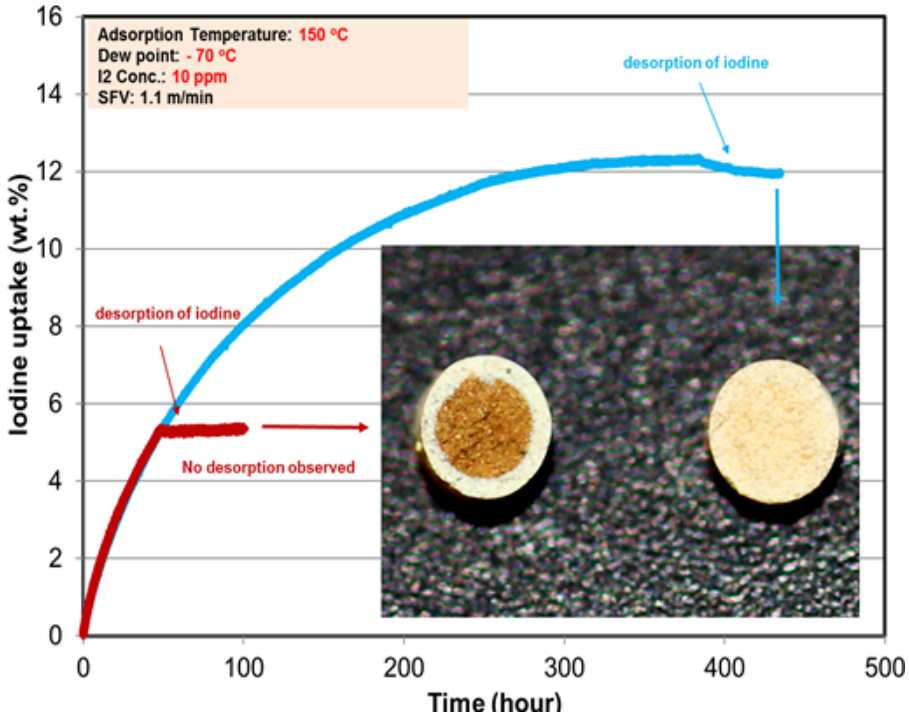

Figure 10. Observation of the shrinking core process during iodine adsorption on Ag^0Z particles.

In order to determine the dominating rate controlling mechanisms, the obtained kinetic data were fitted by the SC model with different combinations of controlling terms: mass transfer (external mass transfer and diffusion) controlling using Eq. (6), reaction controlling using Eq. (7), and all three controlling terms using Eq. (1).

$$t = \frac{q}{q_e}\tau_1 + \left(1 + 2\left(1 - \frac{q}{q_e}\right) - 3\left(1 - \frac{q}{q_e}\right)^{2/3}\right)\tau_2 \qquad (6)$$

$$t = \left(1 - \left(1 - \frac{q}{q_e}\right)^{1/3}\right)\tau_3 \qquad (7)$$

It was assumed that the iodine adsorption process was isothermal since the process took tens to hundreds of hours to reach equilibrium, so the heat of adsorption was generated slowly and dissipated into the passing gas stream. This dissipation was facilitated with the experimental single-layer of adsorbent particles exposed to the gas stream.

1.3.6.3 The effect of superficial gas velocity

The superficial gas velocity affects the adsorption kinetics through influencing the external gas film mass transfer resistance. To evaluate the effect of gas velocity, experiments with a single layer of Ag^0Z particles were conducted at 423 K at varying gas velocities ranged from

0.55 to 4.4 m/min. The uptake curves plotted in **Figure 11** show that there is no significant difference in uptake rate when the gas velocity is in the range of 1.1 – 4.4 m/min. The uptake of iodine with ~25 ppmv iodine over gas velocities of 1.1 and 2.2 m/min, and with ~9 ppmv iodine over gas velocities of 1.1 and 4.4 m/min are very close. However, the iodine uptake with 50.9 ppmv iodine over gas velocity of 0.55 m/min is significantly slower compared to that with 51.2 ppmv over gas velocity of 1.1 m/min. Despite the minor difference of iodine concentration in the comparisons, these results suggest that the effect of external mass transfer resistance at gas velocities of 1.1 – 4.4 m/min on the adsorption process is not significant, while at low gas velocity such as 0.55 m/min the impact of the external mass transfer resistance cannot be ignored. **Figure 12** compares the uptake rates of the curves in **Figure 11**, which also indicates that there is no significant impact of gas velocity until it is decreased to 0.55 m/min. Accordingly, the single-layer adsorption experiments were conducted with the gas velocities of 1.1 m/min.

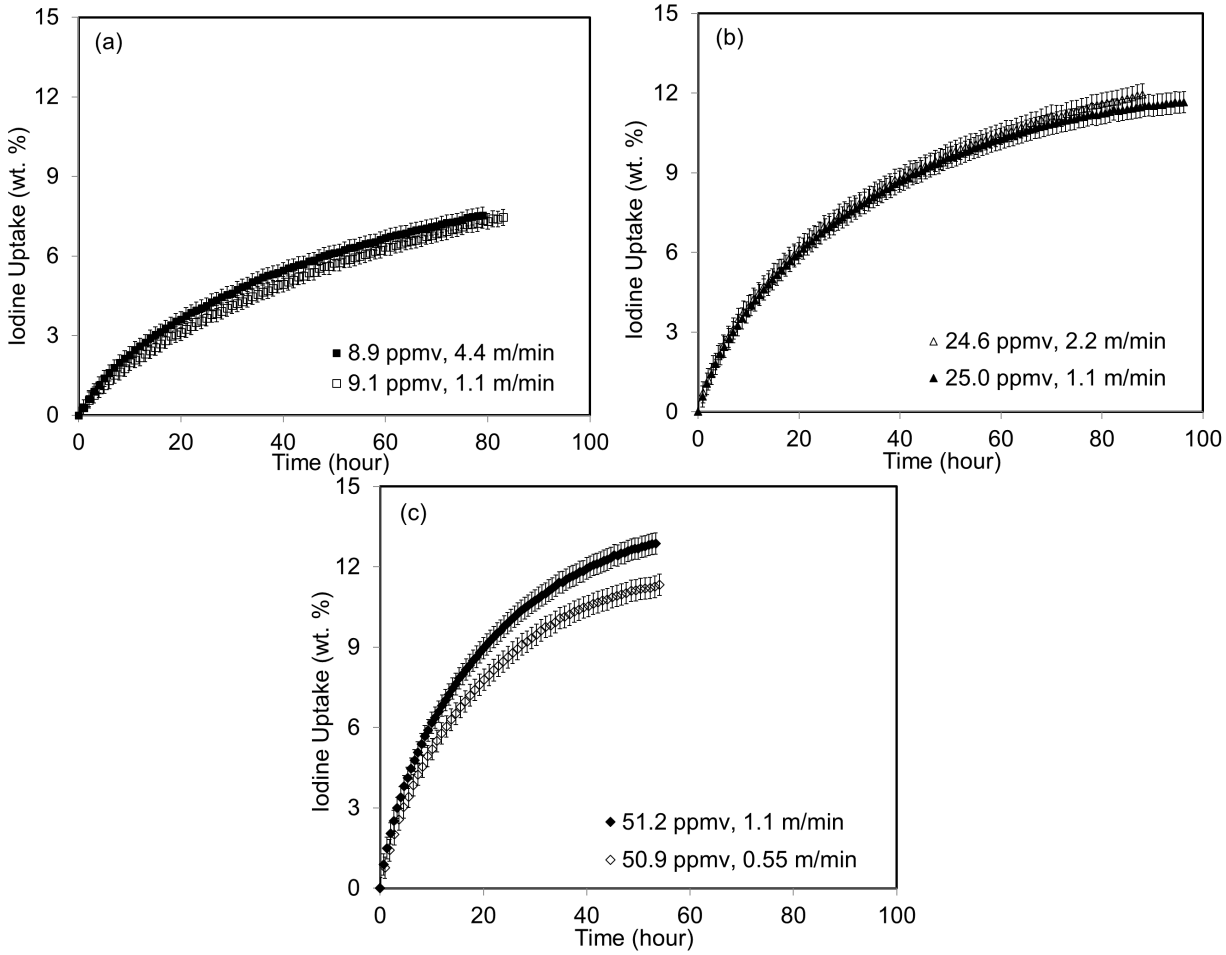

Figure 11. Effect of gas velocity on the uptake rate of iodine on Ag^0Z at 423 K with different iodine concentrations in the gas stream.

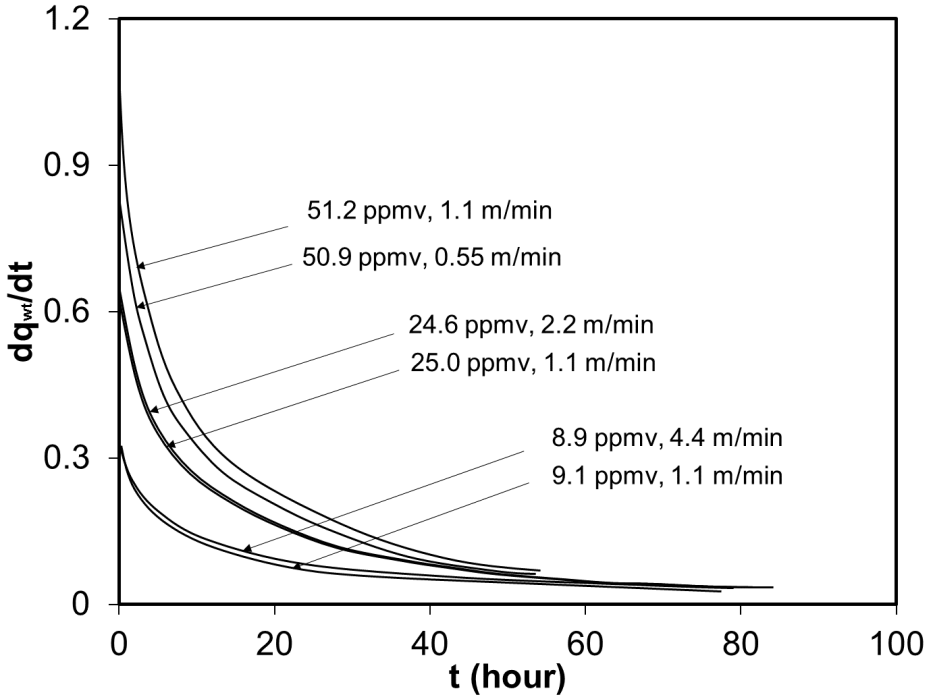

Figure 12. Comparison of the uptake rates of uptake curves in Figure 7. q_{wt} (wt. %) is the concentration of iodine in Ag^0Z.

1.3.6.4 Modeling Results

The kinetic data were fitted by the SC model with different combinations of controlling terms as shown in Eq. (1), (6) and (7) and model parameters were evaluated. Since the external gas film mass transfer resistance did not have significant impact on the uptake kinetics under the conditions studied, the gas film mass transfer coefficient (k_f) in τ_1 was estimated by the Ranz and Marshall correlation: [48]

$$Sh = 2 + 0.6Sc^{1/3}\,\mathrm{Re}^{0.5} \qquad (8)$$

where *Sh*, *Sc* and *Re* are the dimensionless Sherwood number, Schmidt number and Reynolds number. The effect of the pellet-supporting screen on k_f is assumed negligible.

The iodine molecular diffusivity was estimated by the Fuller et al.[49] correlation,

$$D_{AB} = \frac{0.00143T^{1.75}}{PM_{AB}^{1/2}\left[\left(\sum\nu\right)_A^{1/3} + \left(\sum\nu\right)_B^{1/3}\right]^2} \qquad (9)$$

where the subscripts *A* and *B* denote iodine and air, respectively, *P* is the pressure in bar, M_{AB} is the average molecular weight defined by $M_{AB} = \dfrac{2}{1/M_A + 1/M_B}$, and ν is the atomic diffusion

volume. For the iodine-air system, P = 1 bar, $M_{AB} = 52.0$ g/mol, $\left(\sum \nu\right)_A = 59.6$ and $\left(\sum \nu\right)_B = 19.7$.[49] The kinematic viscosity of air needed for estimating the gas film mass transfer coefficient were estimated by REFPROP.[50]

Average values of the pore diffusivity (D_p) and reaction constant (k_s) were estimated by least-square fitting of the uptake curves, and were substituted into Eq. (1), (6) and (7) to predict the iodine adsorption on Ag^0Z. **Figure 13** shows the comparison of the predictions by the three equations at 473 K. The SC model with all controlling terms showed a very good capability to fit the experimental data, while the model with only mass transfer or reaction controlling terms could not describe the iodine adsorption process well. This result suggests that both mass transfer and reaction control the adsorption process of iodine on Ag^0Z.

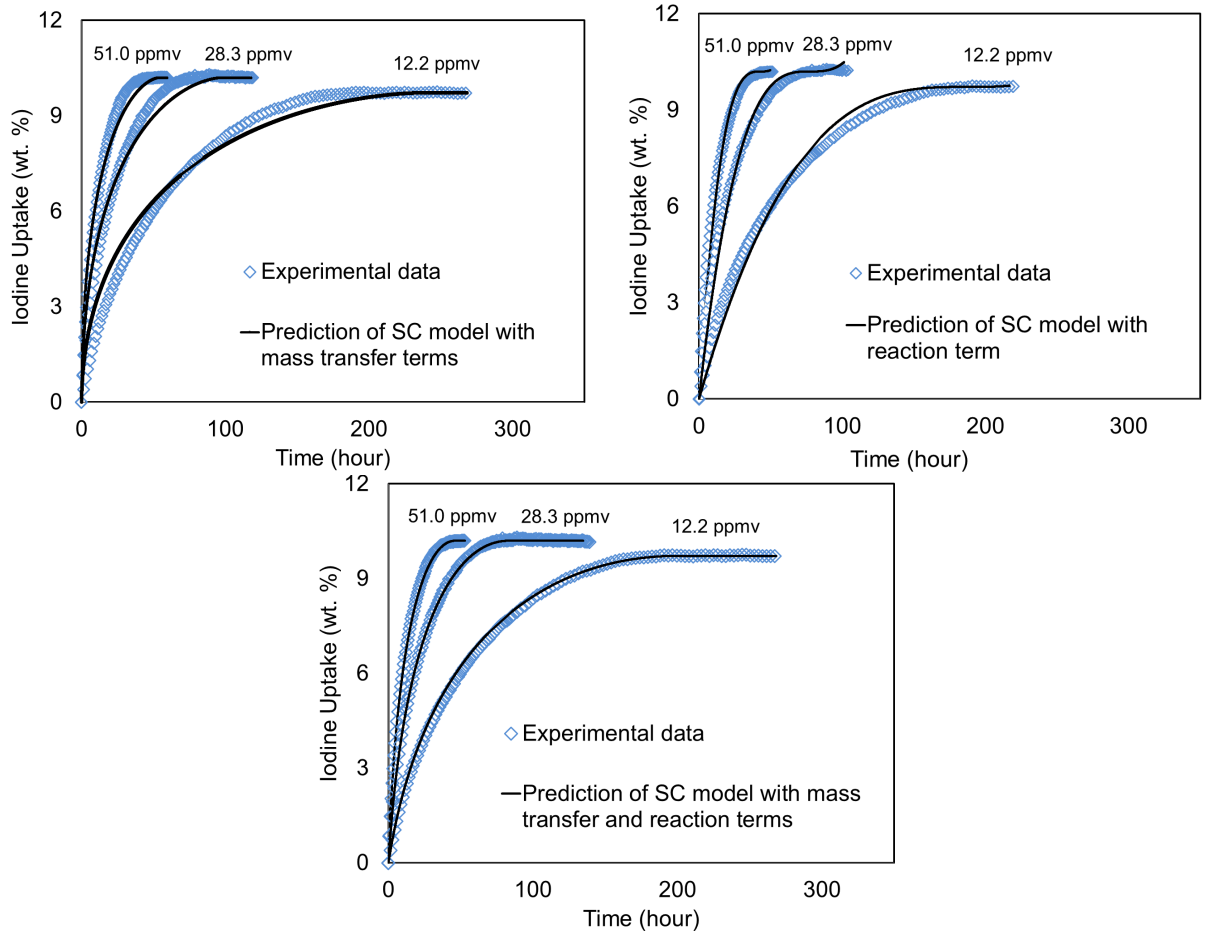

Figure 13. Comparison of the prediction of the SC model with different combinations of rate controlling terms.

The curve-fitting error was estimated by the average absolute relative deviation (AARD) expressed as following Eq. (10).

$$AARD(\%) = \sum_{i=1}^{n} \left| \frac{y_i^{\exp} - y_i^{mol}}{y_i^{\exp}} \right| \times 100 \qquad (10)$$

where the subscript i indicates the i^{th} data point of the total n data points, and superscripts *exp* and *mol* represent the experimental data and model prediction, respectively. The comparison of fitting results using the AARD and calculated parameters for the different models is shown in **Table 2**. The average AARD of 1.57% indicates that the SC model with all rate controlling terms can describe the iodine adsorption better than the models with only mass transfer or reaction controlling terms, which have average AARDs beyond the acceptable range. The coefficients and the reaction constant increase with temperature, which implies that high temperature favors the rate of mass transfer and Ag-I reaction.

The model parameters of all sets of conditions obtained for the SC model with mass transfer and reaction terms of Eq. (1) are listed in **Table 3**. The good agreement of D_p and k_s values at each temperature and the very small AARD at all sets of conditions confirm the good capability of the model to predict the iodine uptake process. As mentioned above, the silver nanoparticles in Ag^0Z locate on the surface of the mordenite crystals. Therefore, the obtained pore diffusion (D_p) mainly describes the diffusion of iodine molecules through the macro pores between the modenite crystals rather than the micro pores in the mordenite crystals. As expected, the values of D_p and k_s increased with temperature as the rates of diffusion and reaction would be faster at a higher temperature. The values of τ_2 and τ_3 are of the same order, and both are about two orders of magnitude greater than τ_1, indicating the effects of pore diffusion resistance and reaction resistance on the iodine uptake rate are much more significant than that of external gas film mass transfer resistance. Therefore, the major mechanisms of iodine adsorption on Ag^0Z under the studied conditions are pore diffusion through the adsorbent and Ag-I reaction.

Table 2. Variables and model parameters for the SC Model

			SC model with mass transfer terms			SC model with reaction term		SC model with mass transfer and reaction terms			
T (K)	v [24] (cm^2/s)	D_{AB} (cm^2/s)	k_f (cm/s)	D_p (cm^2/s)	*AARD (%)*	k_s (cm/s)	*AARD (%)*	k_f (cm/s)	D_p (cm^2/s)	k_s (cm/s)	*AARD (%)*
373	0.232	0.144	6.49	2.41×10^{-3}	6.47	6.08×10^{-2}	7.06	6.49	4.91×10^{-3}	0.132	1.42
437	0.284	0.179	7.45	2.85×10^{-3}	5.23	7.60×10^{-2}	7.22	7.45	5.58×10^{-3}	0.164	2.02
473	0.348	0.218	8.42	3.79×10^{-3}	8.38	9.72×10^{-2}	6.47	8.42	8.07×10^{-3}	0.196	1.26
Ave.					6.69		6.92				1.57

Table 3. Experimental results and model parameters for the SC Model with mass transfer and reaction controlling terms.

$[I_2]$ (ppmv)	Iodine loading (kg/100kg)	SC						
		τ_1 (h)	τ_2 (h)	τ_3 (h)	k_f (cm/s)	D_p (cm^2/s)	k_s (cm/s)	AARD%
				373K				
10.0	10.62	2.70	1.71×10^{2}	1.38×10^{2}	6.49	4.96×10^{-3}	1.27×10^{-1}	1.29
21.9	10.85	1.26	7.85×10^{1}	6.42×10^{1}	6.49	5.04×10^{-3}	1.27×10^{-1}	1.21
39.9	11	7.00×10^{-1}	4.65×10^{1}	3.19×10^{1}	6.49	4.73×10^{-3}	1.42×10^{-1}	1.76
Avg					6.49	4.91×10^{-3}	1.32×10^{-1}	1.42
				423K				
9.1	12.3	3.43	2.13×10^{2}	1.73×10^{2}	7.45	5.81×10^{-3}	1.48×10^{-1}	1.43
24.2	12.3	1.29	7.93×10^{1}	5.37×10^{1}	7.45	5.85×10^{-3}	1.78×10^{-1}	1.80
25.0	12.5	1.26	8.13×10^{1}	5.71×10^{1}	7.45	5.52×10^{-3}	1.35×10^{-1}	2.83
51.2	13.7	6.74×10^{-1}	4.36×10^{1}	3.06×10^{1}	7.45	4.85×10^{-3}	1.68×10^{-1}	1.84
52.0	13.25	6.39×10^{-1}	3.94×10^{1}	2.50×10^{1}	7.45	5.86×10^{-3}	1.91×10^{-1}	2.20
Avg					7.45	5.84×10^{-3}	1.72×10^{-1}	2.02
				473K				
12.2	9.72	1.98	1.12×10^{2}	9.90×10^{1}	8.42	7.83×10^{-3}	1.83×10^{-1}	2.05
28.3	10.2	0.496	2.48×10^{1}	2.09×10^{1}	8.42	8.15×10^{-3}	2.00×10^{-1}	1.14
51.1	10.2	8.95×10^{-1}	4.44×10^{1}	3.68×10^{1}	8.42	8.22×10^{-3}	2.05×10^{-1}	0.58
Avg					8.42	8.07×10^{-3}	1.96×10^{-1}	1.26

1.4 Water adsorption on silver mordenite

1.4.1 Introduction

In a real off gas adsorption system, the presence of water in the off-gas streams may impact the performance of Ag^0Z for iodine capture. Therefore, it is of importance to understand the mechanisms of water adsorption on Ag^0Z and how the adsorption of water impacts the performance of Ag^0Z for iodine. In this work, both single-component adsorption of water including both kinetic and equilibrium, and co-adsorption of water and iodine on Ag^0Z at potential operation conditions were studied experimentally. Wide experimental condition ranges were investigated: temperatures from 25 to 200 ^oC, and dew points from -70 to 20 ^oC. The kinetics of water adsorption on Ag^0Z was studied to obtained the intraparticle mass transfer and reactions involved in the adsorption process at a micro scale. The uptake curves of water were well described by kinetic models such as Shrinking Core and Linear Driving Force models. The GSTA (Generalized Statistical Thermodynamic Adsorption) model was used to describe the adsorption equilibria of iodine and water, and isotherm parameters of single-component adsorption were determined. Iodine and water co-adsorption experiments are being performed to obtain both kinetics and equilibrium data. Obtained data and model parameters were also sent to the collaborating research group at GIT for modelling development and verification.

1.4.2 Experimental setup

A photograph of the water adsorption system is shown in **Figure 14**. The key parts in the system are the same as the iodine adsorption system shown in **Figure 2,** except that a water vapor generation system is used instead of the Dynacalibrators. Water vapor was generated by bubbling water in a controlled manner. Dry air from a gas cylinder was split into two streams, the carrier stream and the makeup stream, controlled by two mass flow controllers. The carrier stream passed through 1-3 glass tubes containing deionized water. The glass tubes were immersed in a water bath, the temperature of which was controlled at a value between 4-20 ^{o}C. By controlling the gas flow rates of the two streams and water temperature, desired water concentrations were produced. The water vapor pressures (dew points) were measured by a hygrometer (Easidew Online, Michell Instruments) by passing the gas stream through a gas sampler (Easidew Sampler, Michell Instruments). Adsorption temperature was controlled by a second water bath.

Water adsorption experiments were conducted at dew points of -69 - 20 ^{o}C and temperatures of 25 - 200 ^{o}C. The gas flow rate studied was between 1 L/min. According to the previous studies of water adsorption on MS3A and the iodine adsorption study discussed above, this flow rate is high enough to minimize the gas film mass transfer resistance. Increasing the flow rate would not lower the gas film resistance further. Similar to the iodine adsorption experiments, about 0.2 g $Ag^{0}Z$ pellets were carefully loaded not to touch one another. Before water adsorption, the samples were degassed at 150 ^{o}C for 8 hours under vacuum to remove any moisture in the samples.

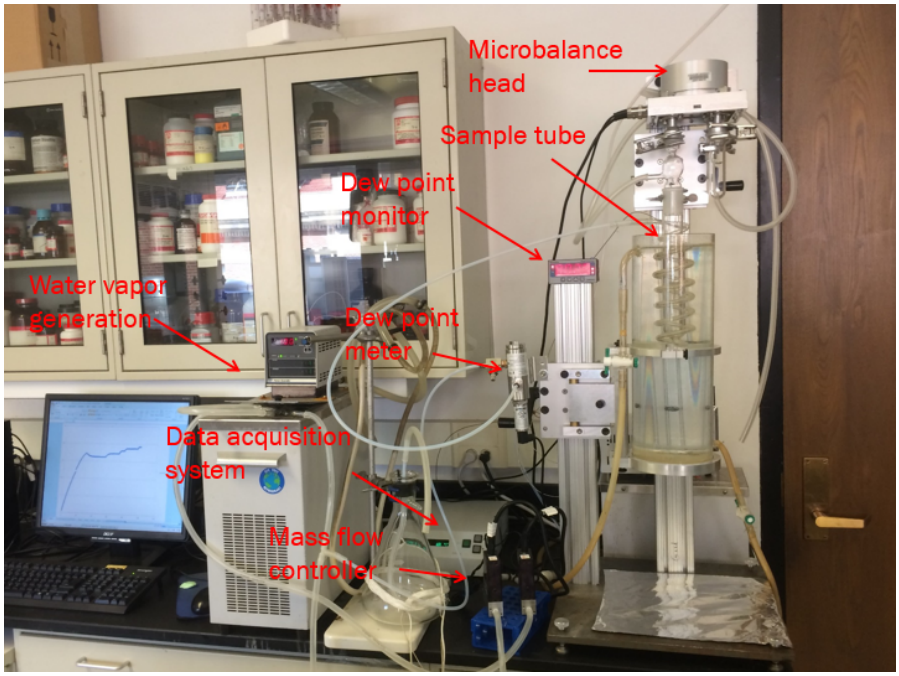

Figure 14. A photograph of the water adsorption system.

1.4.3 Isotherms of water adsorption on Ag^0Z

Water adsorption isotherms were measured at adsorption temperatures of 25, 40, 60, 80, 100, 150 and 200 °C and over water dew points from -70 to 20 °C (or water vapor pressure from 0.001 to 1.6 kPa). Results shown in **Figure 15** indicate that the water uptake capacity increases with water vapor pressure but decreases with adsorption temperature. It was found that the water adsorption isotherm on Ag^0Z is a Type IV isotherm per the IUPAC (international union of pure and applied chemistry), which indicated the formation of monolayer followed by multilayer. **Figure 16** shows a comparison of the isotherm of water on Ag^0Z with the isotherm of water on MS3A at 25 °C, which is a typical Langmuir adsorption isotherm (Type I) for monolayer adsorption.

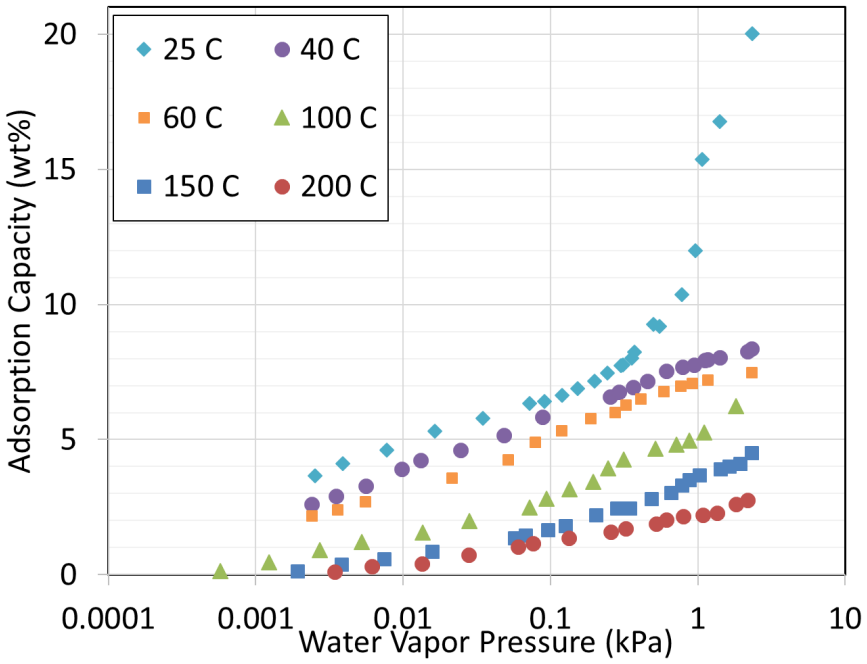

Figure 15. Adsorption isotherms for water adsorption on Ag^0Z at 25, 40, 60, 80, 100,150 and 200 °C.

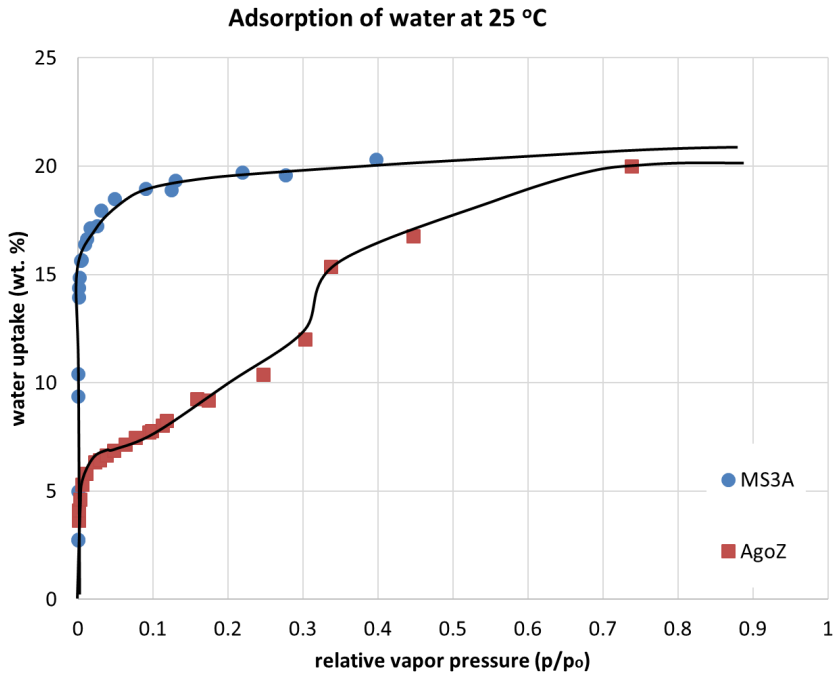

Figure 16. Comparison of the isotherm of water on Ag^0Z (Type IV Isotherm) with the isotherm of water on MS3A at 25 °C (Type I Isotherm).

As discussed in the iodine adsorption study above, Section 1.3, the capture of iodine with Ag^0Z would be at an optimal temperature of 150 °C in order to reach the best performance of the adsorbent. At such relatively high temperature, the relative vapor pressure of water in a real off-gas treatment system would be lower than 0.05, since the saturate water pressure at 150 °C is about 1.52 MPa. The adsorption of water on Ag^0Z would always be in the monolayer adsorption range. Therefore, to understand the impact of water on the iodine adsorption performance of Ag^0Z, the study adsorption of water on Ag^0Z should be focused on the monolayer adsorption range.

To determine the maximum monolayer water adsorption capacity of Ag^0Z, the BET adsorption model was used, which is expressed as Eq. (11):

$$\frac{1}{v\left[(p_0/p)-1\right]} = \frac{c-1}{v_{\mathrm{m}}c}\left(\frac{p}{p_0}\right) + \frac{1}{v_m c} \tag{11}$$

where p and p_0 are the equilibrium and the saturation pressure of adsorbates at the temperature of adsorption, v is the adsorbed gas quantity, and v_m is the monolayer adsorbed gas quantity. C is the BET constant.

The monolayer capacity was estimated by plotting a straight line with $p/v(p_0-p)$ on the y-axis and p/p_0 on the x-axis with the experimental data in the range of $0.05<p/p_0<0.35$, which is the effective range for the BET theory. The results are shown in **Figure 17**. The calculated maximum monolayer capacity for water on Ag^0Z is 8.56 wt.%. **Figure 18** shows a good fitness of the BET model with the experimental data in the effective relative pressure range of $0.05<p/p_0<0.35$.

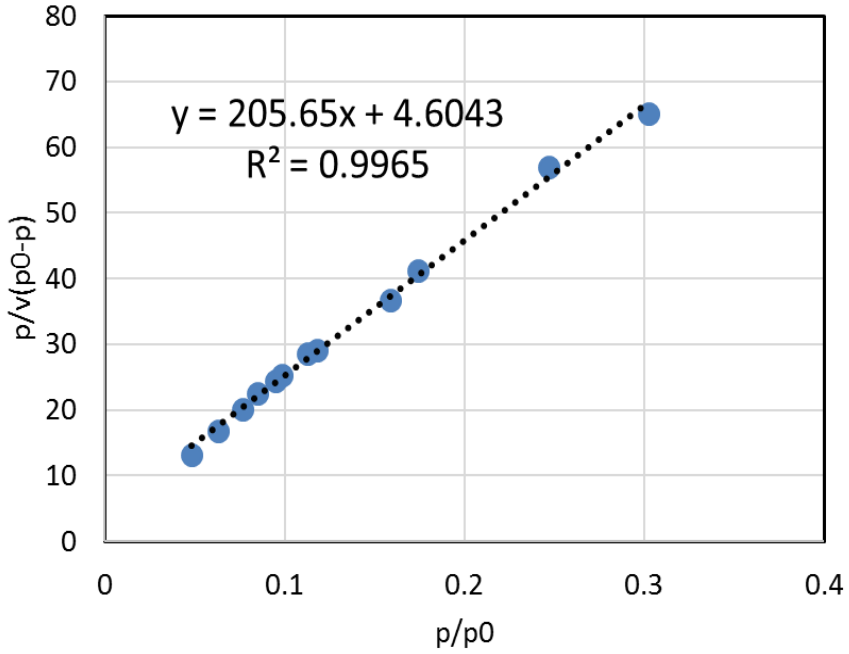

Figure 17. The BET plot of water adsorption on Ag0Z using the data obtained at 25 ^{o}C and in the relative vapor pressure range of 0.05 - 0.3.

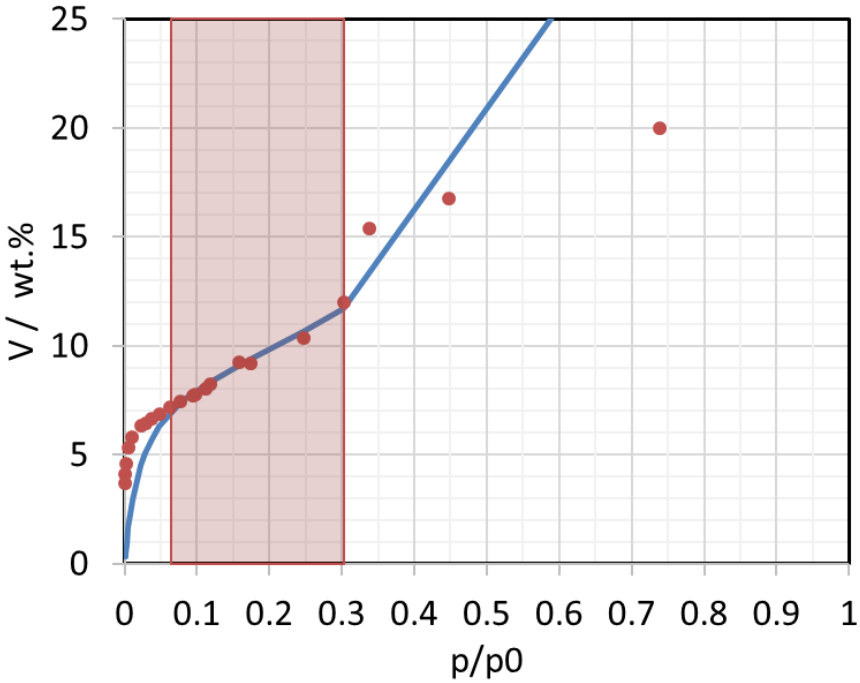

Figure 18. Good fitness of the BET model to the experimental data of water adsorption on $Ag^{0}Z$ at 25^{o}C and in $0.05<p/p_0<0.35$

The equilibrium data obtained are analyzed with the GSTA model to determine the model parameters. The GSTA model is summarized below:

$$\phi = \frac{q}{q_{\max}} = \frac{1}{m}\frac{\sum_{n=1}^{m} nK_n^o\left(p/P^o\right)^n}{1+\sum_{n=1}^{m} K_n^o\left(p/P^o\right)^n} \qquad (12)$$

$$K_n^o = \exp\left\{-\frac{\Delta H^o{}_n}{RT}+\frac{\Delta S_n^o}{R}\right\} \qquad (13)$$

In Eq. (12), $q_{\max}$ is the theoretical maximum adsorption capacity, m is the number of adsorption sites, K_n is the equilibrium constant for the adsorption of n molecules in a network of m available adsorption sites, K_n^o is the dimensionless equilibrium constant, $P°$ is standard state pressure (100 kPa), ΔH_n is the standard enthalpy of adsorption of n molecules in a network of sites, and ΔS_n is the standard entropy of adsorption of n molecules in a network of sites. $2 + m$ parameters ($q_{\max}$, m, and K_n) must be determined using equilibrium data. After the equilibrium model parameters are obtained, kinetic models will be evaluated for modeling the adsorption dynamics.

The GSAT was demonstrated in our previous studies capable of describing the water on MS3A system and other systems in the literature.[50] In addition, the parameters obtained by GSTA model can be applied to the equilibrium model for predicting multi-component adsorption systems.[51] Therefore, the GSTA model was used in this study for water adsorption isotherms and incorporated into the column adsorption model being developed. **Figure 19** shows the modeling of water adsorption isotherms with the GSTA model. A very good agreement between the prediction and experimental data is shown in the plot.

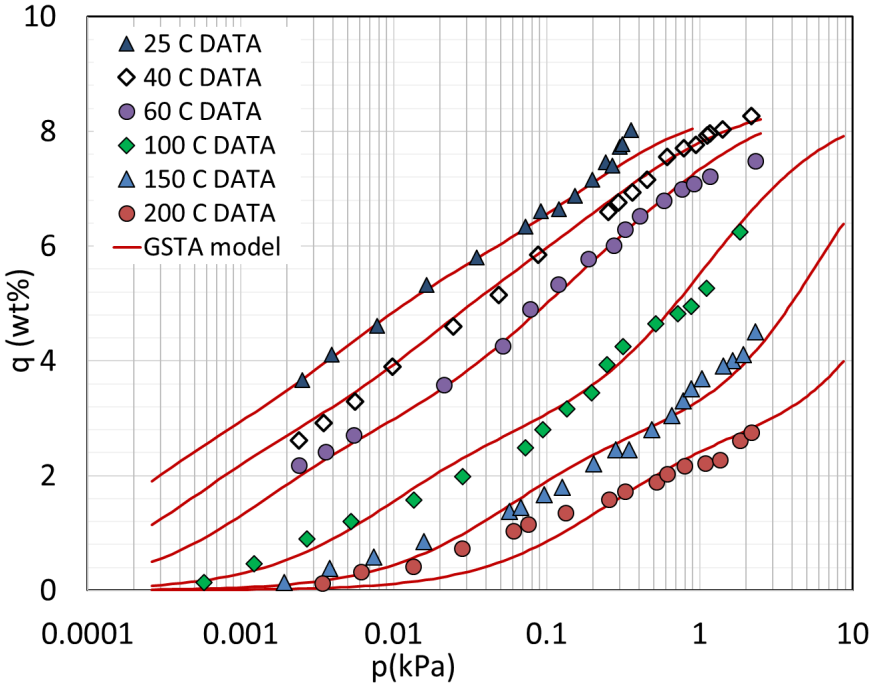

Figure 19. Prediction of water adsorption capacity by GSTA model. Dots are experimental data and solid lines are model prediction.[52]

1.4.4 Kinetics of water adsorption on Ag^0Z

1.4.4.1 The uptake curves

Kinetic data of water adsorption on Ag^0Z at 25, 40, 100, 150 and 200 ^oC have been obtained at varying water dew points from -50 to 12 ^oC. As shown in **Figure 20**, adsorption takes less than 10 hours to reach equilibrium at studied temperatures. The uptake rate increases with increasing temperature and water concentrations of the gas stream, which is due to faster mass transfer and diffusion rates. Experiments are in progress to obtain kinetic data at low-temperature range: 25 – 80 ^oC. The obtained kinetic data are analyzed with kinetic models including shrinking core (SC) model and linear driving force (LDF) model.

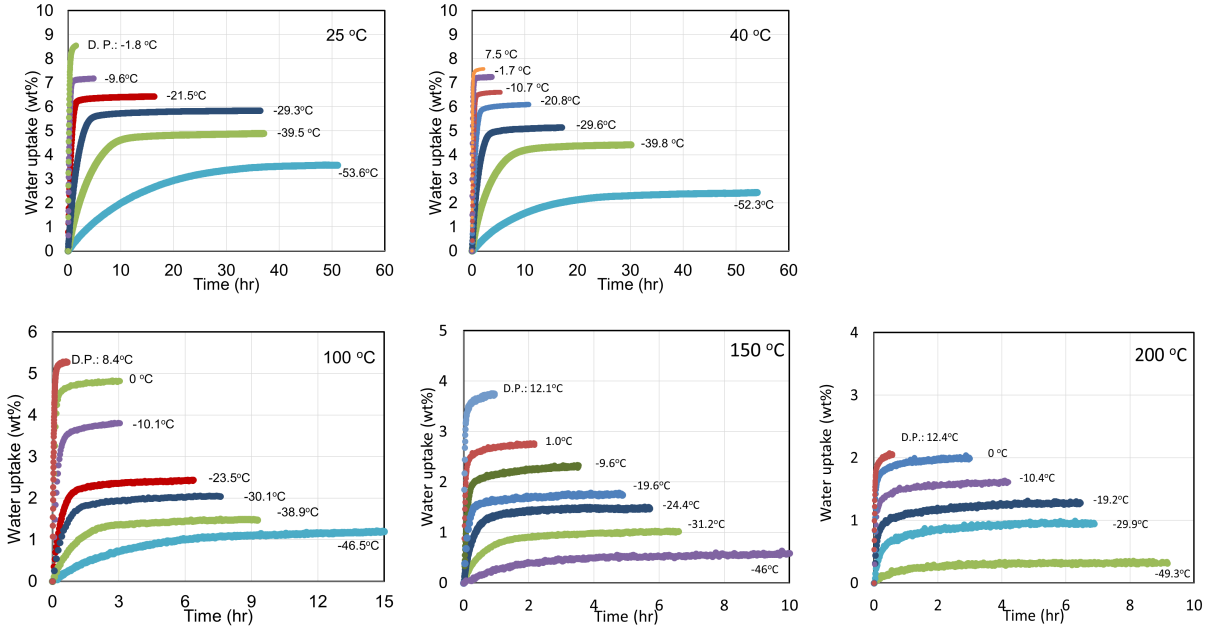

Figure 20. Uptake curves of water adsorption on Ag^0Z at temperatures from 25 to 200 ^oC and duw point from -53.6 to 12.4 ^oC. [53]

1.4.4.2 The Shrinking Core Model and Linear Driving Force Model

For the SC model, since the water adsorption on AgZ is a physical process, it is assumed that there is no reaction going on during the adsorption process. Therefore, Eq. (6) without the reaction term is used, which only has an external mass transfer term and a pore diffusion term. For comparison, the coefficient k_{LDF} in the LDF model is simplified to two terms, which also has an external mass transfer term and a macropore diffusion term as shown by Eq (6). τ_1 and τ_2 can be expressed as Eq. (14) and (15).

$$\tau_1 = \frac{R_p}{3\varepsilon_p k_f}\frac{q_e \rho_p}{C_b} \qquad (14)$$

$$\tau_2 = \frac{R_p^2}{6\varepsilon_p D_p}\frac{q_e \rho_p}{C_b} \qquad (15)$$

The LDF model, originally proposed by Gleuckauf and Coates in 1947,[54] has been widely used in modeling adsorption kinetics due to its analytical simplicity. According to this model, the average sorbate uptake rate is given by the product of the amount required to reach equilibrium and the so-called LDF mass transfer coefficient, as given by Eq. (16):

$$\frac{d\bar{q}}{dt} = k_{LDF}\left(q_e - \bar{q}\right) \qquad (16)$$

where $\bar{q}$ and q_e are the transient average sorbate concentration in sorbents and the equilibrium sorbate concentration in sorbents, respectively, and k_{LDF} is the LDF mass-transfer coefficient. Integrating Eq. (16) results in Eq. (17), and k_{LDF} can then be obtained from the $\ln\left(\frac{q_e - \bar{q}}{q_e}\right)$ vs t plot.

$$\ln\left(\frac{q_e - \bar{q}}{q_e}\right) = -k_{LDF}t \qquad (17)$$

Assuming a linear isotherm, it can be shown that the LDF mass transfer resistance has the following expression:[54]

$$\frac{1}{k_{LDF}} = \frac{R_p}{3k_f}\frac{q_e\rho_p}{C_b} + \frac{R_p^2}{15\varepsilon_p D_p}\frac{q_e\rho_p}{C_b} + \frac{R_c^2}{15D_c} \qquad (18)$$

where, C_b is the bulk gas-phase concentration, D_c is the micropore diffusivity, D_p is the macropore diffusivity, k_f is the film mass transfer coefficient, R_c is the radius of micropore, R_p is the radius of pellet, ε_p is the porosity of pellet, and ρ_p is the density of pellet. The three terms in the right-hand side of Eq. (4), from left to right, are external film resistance, macropore resistance and micropore resistance, respectively. C_b can be calculated from water vapor pressure assuming ideal gas behavior.

1.4.4.2 Modeling results

Water uptake curves were fitted by the SC and LDF models. The film mass transfer coefficient (k_f) can be estimated by the Ranz and Marshall correlation as mentioned in the iodine adsorption section. The diffusion parameter D_p was determined by least-square fitting of the experimental data. For the SC model, the macropore and micropore diffusivity is lumped into one term D_p. However, for the LDF model, the overall mass transfer resistance is a combination of the external film resistance, the macropore resistance and the micropore resistance. To determine the mechanism of water diffusion in the Ag^0Z and the dominating resistance between the macropore resistance and the micropore resistance, adsorption experiments with different particle sizes are conducted.

Figure 21 shows the experimental results of water adsorption on Ag^0Z particles of 0.9 mm and 0.8 mm radius. Each experiment was conducted twice and the results agreed well with each other. As shown in **Figure 21**, the adsorption rate with small particles was faster than that of large particles, which indicates that the first term and second term are rate controlling since there is a R_p these terms and no R_p in the third term. Furthermore, since the flow rate of the experiments was high and the k_f in the first term is much higher comparing to the D_p in the

magnitude in the second term, the change of R_p in the first term will not contribute much to the overall adsorption rate. Therefore, the second term, macropore diffusion resistance, is dominating the adsorption rate.

In addition, the uptake curves with both the 0.9 and 0.8 mm particles were well fitted by the LDF force model by only varying the R_p in the equation (**Figure 21**), which is a strong proof of that the macropore diffusion is the rate controlling diffusion. Therefore, the equation for overall mass transfer resistance is simplified to Eq. (19)

$$\frac{1}{k_{LDF}} = \frac{R_p}{3k_f}\frac{q_e\rho_p}{C_b} + \frac{R_p^2}{15\varepsilon_p D_p}\frac{q_e\rho_p}{C_b} \qquad (19)$$

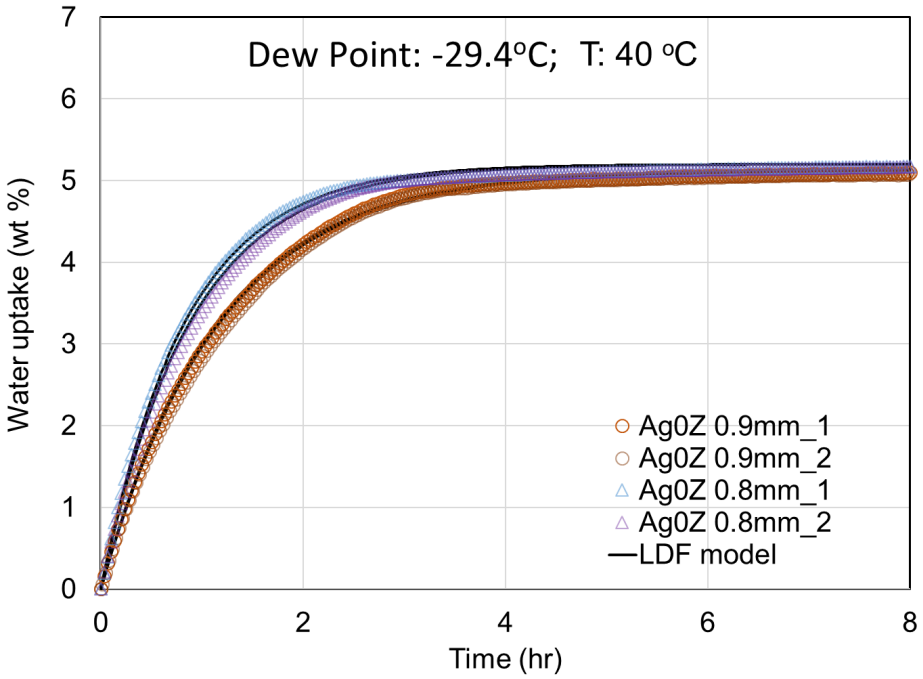

Figure 21. Fitting of LDF model to the water adsorption experimental data with different size of Ag^0Z particles. The model is able to describe data obtained with both small and large particles by just changing the R_p value in Eq. (18), indicating that macropore diffusion is the rate controlling term, and thus micro diffusion term in Eq. (18) can be ignored.

Both models were found able to describe kinetic processes of water adsorption on Ag^0Z, and the average AARD of curve-fitting with SC and LDF model are 3.29 % and 3.09 %, respectively. **Figure 22** shows the curve-fittings with the two models with the experimental data at 25°C as an example. The excellent fittings indicate the good capability of the models to describe the adsorption processes. The estimated $D_{AB,}$ k_f and D_p values, as well as the AARD, at all temperatures studied are listed in **Table 4**. The values indicated that water adsorption on Ag^0Z at the studied experimental conditions was controlled by both external film resistance and macropore resistance. The k_f values are much larger compared to D_p , which indicated that the gas film mass transfer resistance was smaller than the diffusion resistance in the particles.

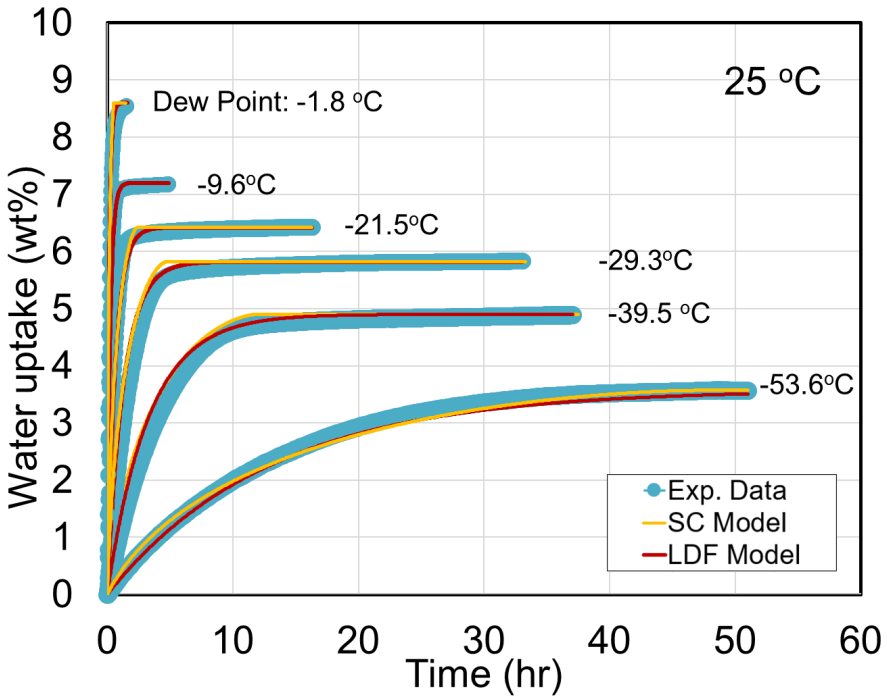

Figure 22. Curve-fitting of a water uptake curves by the SC model and LDF Model. Adsorption temperature: 25 °C; dew point: -53.6 to -1.8 °C.

Table 4. Properties and model parameters for the SC and LDF Models (P= 0.1 MPa).

			SC Model		*LDF Model*	
T (°C)	D_{AB} (cm²/s)	k_f (m/s)	D_p (cm²/s)	*AARD (%)*	D_p (cm²/s)	*AARD (%)*
25	0.253	10.416	0.106	2.66	0.167	2.79
40	0.276	10.992	0.105	2.58	0.170	2.50
100	0.375	13.364	0.118	3.34	0.200	2.60
150	0.468	15.453	0.116	3.82	0.201	3.45
200	0.569	17.572	0.059	4.08	0.169	4.09
average				3.29		3.09

Figure 23 illustrates a comparison of D_p obtained for the LDF and SC models. The D_p values obtained with the SC model were comparable with but smaller than those obtained with the LDF model. Also, it was found that considering experimental uncertainties, D_p generally increases as temperature increases, which is due to a faster molecular motion at higher temperatures resulting in a higher diffusion rate. It was noticed that when the temperature was increased from 150 to 200 °C the diffusivity decreased. The reason would be a possible physical or chemical structure change of the adsorbents at temperatures above 150 °C. However, more studies are needed to confirm this assumption.

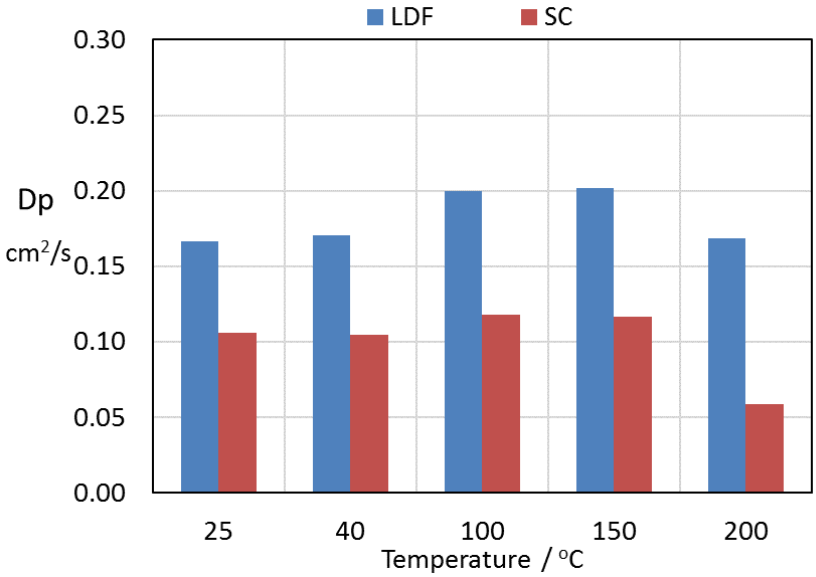

Figure 23. Comparison of the macropore diffusion coefficient obtained for the LDF and SC models

1.5 Co-adsorption of I_2 and H_2O on silver mordenite

1.5.1 Experimental system and conditions.

The experiments of iodine and water co-adsorption on Ag^0Z were performed with a modified system similar to the iodine adsorption system shown in **Figure 2**. A water vapor generating unit was added to the system so that iodine and water vapor can be generated and passed through the adsorption column simultaneously. A flow diagram of the modified system is shown in **Figure 24**. The experiment procedure is similar to the iodine and water adsorption experiments described above. The experiments were performed at 150 ^oC which is the optimal temperature for iodine adsorption, with iodine concentrations of 10 - 50 ppmv and water concentrations (in terms of dew points) of -18 and 0.6 ^oC. Experiments with different sequences of iodine and water adsorption were also performed to study how the adsorption of water impacts the iodine adsorption capacity of Ag^0Z.

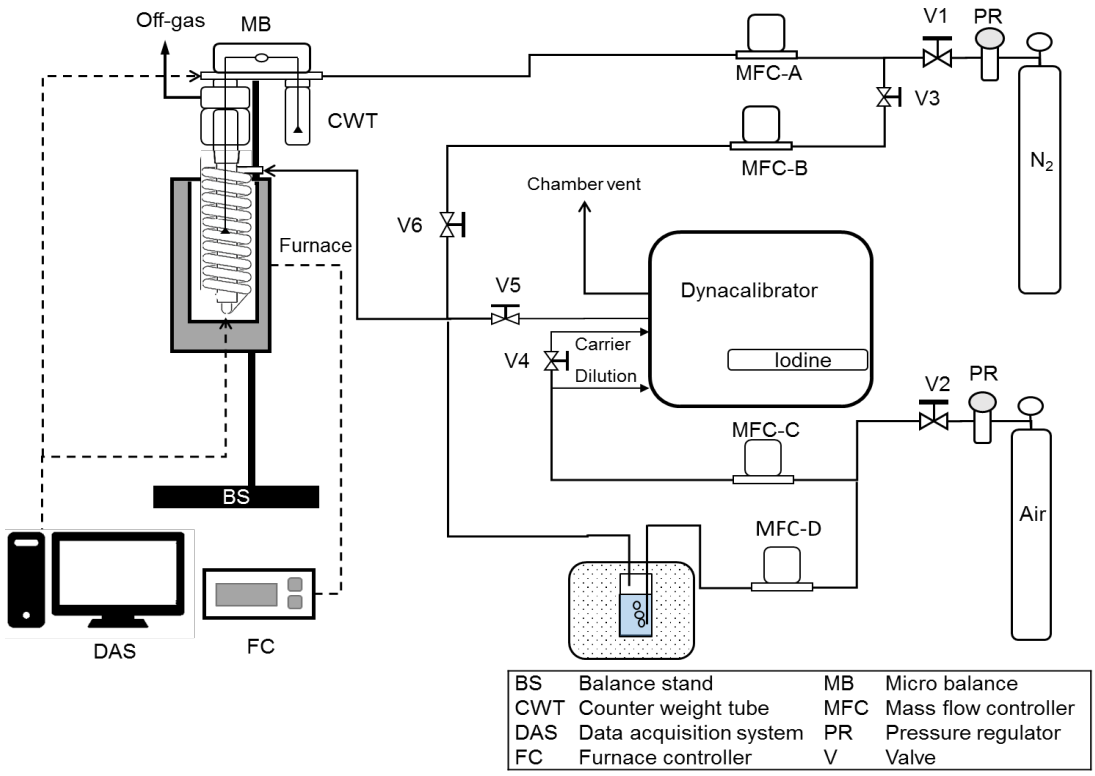

Figure 24. Schematic diagram of the continuous-flow iodine and water co-adsorption system.

1.5.2 Uptake curves and isotherms of iodine and water co-adsorption

The uptake curves of iodine and water co-adsorption on Ag^0Z at 150 ^oC, iodine concentrations of 10, 25, and 50 ppmv, and dew point of -18 ^oC are shown in **Figure 25**. The total weight gain of the adsorbents due to water and iodine adsorption is between 9 - 11 wt.%. The amount of iodine adsorbed was determined by desorbing the water from the adsorbents. According to the water adsorption isotherms in **Figure 15**, the equilibrium water capacity at 150^oC and dew point of -18 ^oC is about 1.8 wt.%. The desorbed water in **Figure 25** showed close to the amount of 1.8 wt.%, which means most of the water was removed from the adsorbents and the resulting weight gain after the desorption leveled off was the total adsorbed iodine. It was observed that the iodine capacity decreased significantly with the presence of water in the gas stream. About 40% of capacity was lost when co-adsorbing with water.

The isotherms of iodine adsorption on Ag^0Z in the gas stream of different water concentrations are shown in **Figure 26**. The iodine adsorption capacity decreased with the increasing of water concentration in the gas stream. Similar to the iodine adsorption in dry air, the iodine adsorption capacity also slightly increased with iodine concentration. The data were sent to the research group at G.I.T. for modeling verification.

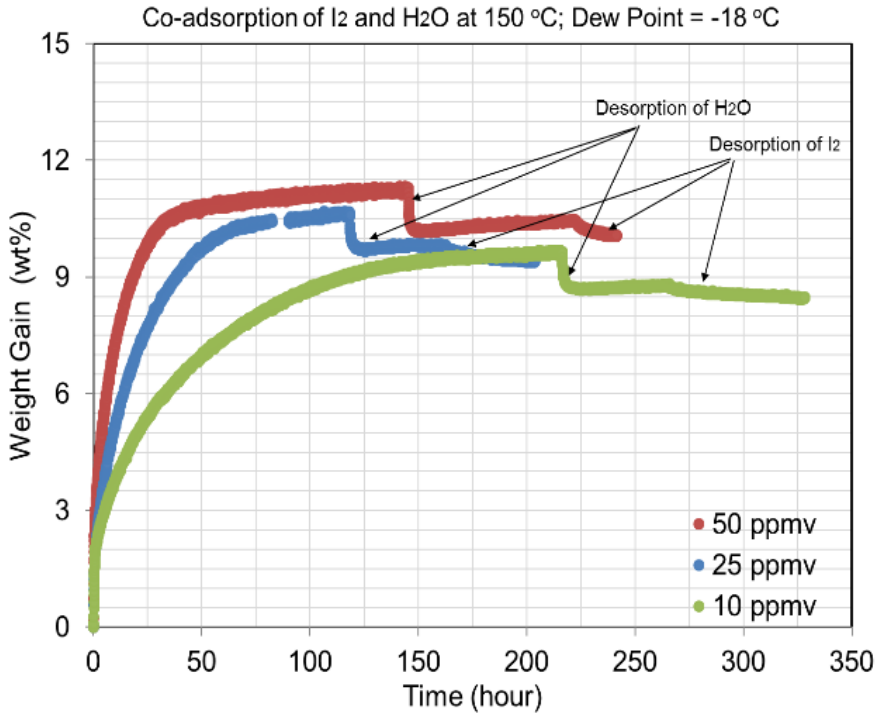

Figure 25. Co-adsorption on iodine and water on Ag^0Z at 150 °C and dew point of -18 °C.

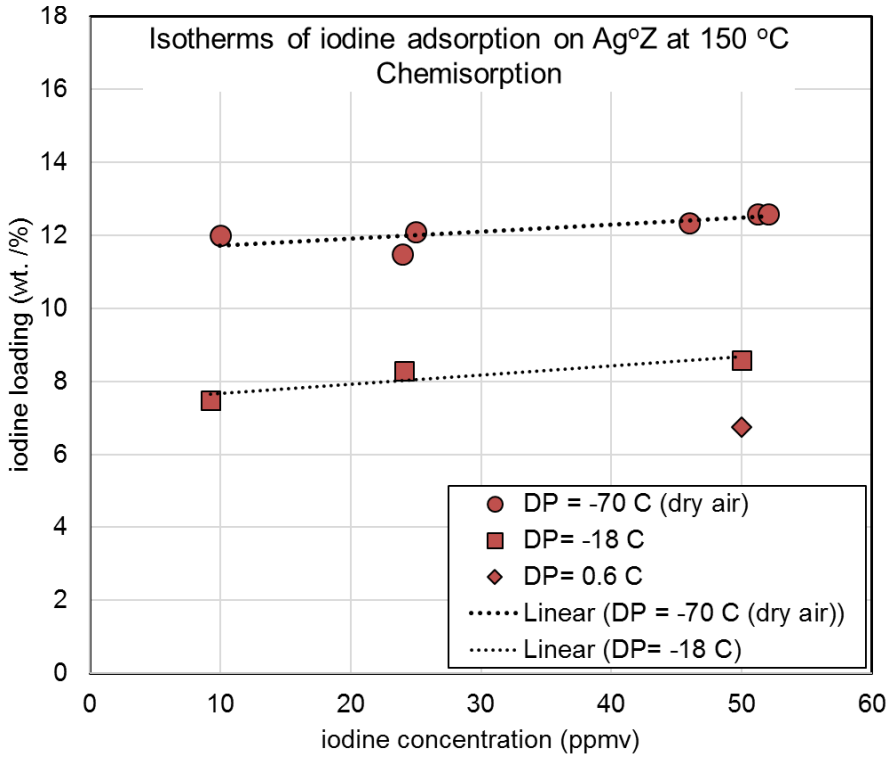

Figure 26. Adsorption of iodine on Ag^0Z at 150 °C over different dew points.

1.5.3 Impact of water on I_2 adsorption capacity of Ag^0Z

To understand the impact of water on the iodine capacity of Ag^0Z, the adsorption experiment of iodine and water were performed in different sequences, and the results are shown in **Figure 27**. The four plots show the adsorption results with iodine concentration of 50 ppmv and water dew point of -70 or -18 ^oC and with different order of experiment: a) adsorption of iodine in dry air and desorption of iodine; b) co-adsorption (simultaneous adsorption) of iodine and water and desorption of water and then iodine; c) adsorption of water followed by iodine adsorption, and then water desorption and finally iodine desorption; d) adsorption and desorption water, followed by adsorption and desorption of iodine. **Figure 27a** shows that, in dry air, the capacity of Ag^0Z almost reached the theoretical maximum capacity of Ag^0Z (14 wt.%). Comparing **Figure 27a** and **27b**, when iodine is co-adsorbed with water at dew point of -18 ^oC, the capacity decreased about 40 %. **Figure 25c** shows that when the particle is pre-equilibrated with water vapor, the capacity for iodine is close to the simultaneous adsorption case (**Figure 27b**). It is noted that, when the water was desorbed, there was no further loading of iodine to reach the capacity in dry air, which indicated that the loss of iodine capacity when water was present was not due to pore blocking by water molecules. The observation on **Figure 27d** further confirmed this conclusion. As shown in the plot, when most of the water is desorbed, the following iodine adsorption did not reach the capacity in the dry air either. Therefore, the impact of the water on the iodine capacity should not be a physical influence. A possible reaction could be the deactivation of silver adsorption sites by water. The silver adsorption sites in the Ag^0Z would be chemically occupied (oxidized) by water, so the site lost the capacity for bonding with iodine.[55] However, future studies including chemical analyses of the water/iodine loaded adsorbents are needed to confirm this conclusion.

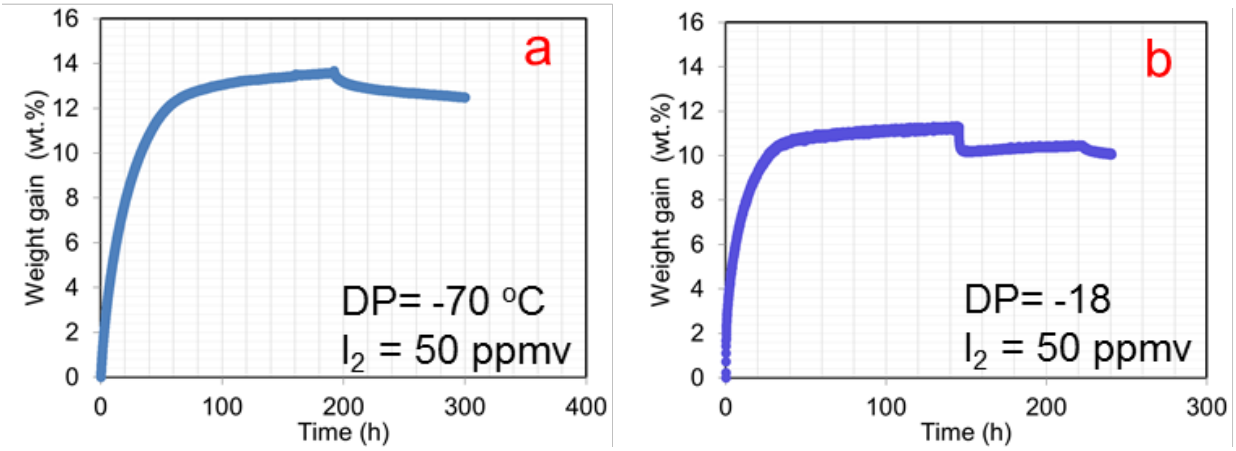

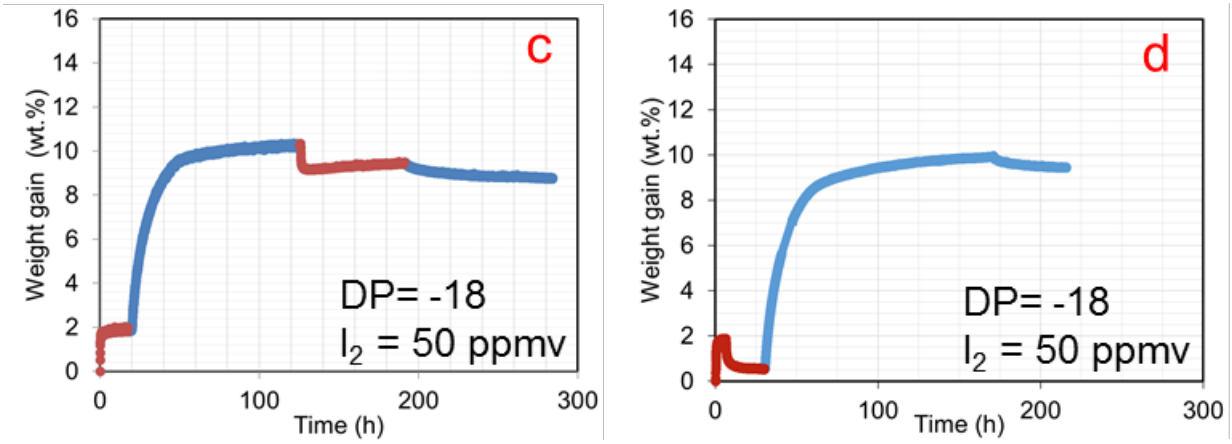

Figure 27. Adsorption of iodine and water in different sequences: a) adsorption of iodine in dry air and desorption of iodine; b) co-adsorption (simultaneous adsorption) of iodine and water and desorption of water and then iodine; c) adsorption of water followed by iodine adsorption, and then water desorption and finally iodine desorption; d) adsorption and desorption water, followed by adsorption and desorption of iodine.[55]

1.6 Conclusions

1) The optimal reduction conditions of Ag^0Z (12.0 wt.% Ag) used in this study were found to be at 400°C and for 24 hours.
2) Based on the equilibrium data from single-layer pellet adsorption experiments, the adsorption of molecular iodine on Ag^0Z is mostly chemisorption through the Ag-I reaction.
3) The optimal adsorption temperature was found to be 150 °C. An average maximum iodine loading of 12.3 wt. % by chemisorption (13.5 wt. % by both chemisorption and physisorption) was achieved at 150 °C, and the corresponding Ag utilization efficiency is 88%.
4) The lower iodine capacity at temperatures 100 °C can be explained by the stronger adverse effect of water in the adsorbents. Future work is needed to study details of water effects. The decrease in iodine capacity at temperatures beyond 150 °C could be due to the decomposition of AgI nanoparticles, according to the experimental observations. More investigations in future studies are needed to confirm this explanation.
5) Furthermore, the Shrinking Core model with mass transfer and reaction controlling terms is capable of describing the kinetics of iodine adsorption on Ag^0Z with an average AARD of 1.57%. The primary controlling mechanisms were found to be diffusion through macro pores of the adsorbent and the Ag-I reaction.
6) For water adsorption, the LDF and SC models are capable of predicting the water uptake, and the AARD is 3.29% and 3.09%, respectively.
7) GSTA model is able to predict the water adsorption isotherms, and isotherm parameters obtained can be applied to models for multi-component adsorption predictions. Therefore, the water in off-gas streams should be removed prior to iodine capture.

8) The presence of water in gas stream significantly affects the iodine adsorption capacity of Ag^0Z. The iodine capacity decreases with increasing water vapor concentrations.

9) The decrease of iodine capacity is not due to the pore blocking by water molecule adsorbed on the adsorbents. It is probably due to the deactivation of the silver adsorption sites in the Ag^0Z. Future chemical analyses are needed to study the mechanisms of the water effect.

1.7 Acknowledgments

This study was supported by the Nuclear Energy University Program, Office of Nuclear Energy, U.S. Department of Energy. We acknowledge David DePaoli and Robert Jubin from Oak Ridge National Laboratory, Jack Law, Amy Welty, and Kevin Lyon from Idaho National Laboratory for providing advises and comments on the project.

1.8 References

1. Mineo H, Iizuka M, Fujisaki S, Hotoku S, Asakura T, Uchiyama G. Study on gaseous effluent treatment for dissolution step of spent nuclear fuel reprocessing. NTIS Reports. 2002; NTIS No: DE2004-828968/XAB.
2. Jubin RT, DelCul GD, Patton BD, Owens RS, Ramey DW, Spencer BB. Advanced fuel cycle initiative coupled end-to-end research, development, and demonstration project: integrated off-gas treatment system design and initial performance-9226. Paper presented at WM2009 Conference, Phoenix, AZ. 2009.
3. Herrmann FJ, Motoi V, Herrmann B, Van Schoor A, Fang D, Fies H. Retention and measurement of iodine-129 and of organoiodine in the off-gas streams of the Karlsruhe reprocessing plant WAK. Proceedings of the 21st DOE/NRC Nuclear Air Cleaning Conference. 1990; 1:222-233.
4. Robens E, Aumann DC. Iodine-129 in the environment of a nuclear fuel reprocessing plant: I. ^{127}I and ^{127}I contents of soils, food crops and animal products. Journal of environmental radioactivity. 1988; 7(2): 159-175.
5. Watanabe Y, Ikoma T, Yamada H, Suetsugu Y, Komatsu Y, Stevens GW, Yusuke M, Tanaka J. Novel long-term immobilization method for radioactive iodine-129 using a zeolite/apatite composite sintered body. ACS applied materials & interfaces. 2009; 1(7): 1579-1584.
6. Mineo H, Gotoh M, Iizuka M, Fujisaki S, Hagiya H, Uchiyama G. Applicability of a model predicting iodine-129 profile in a silver nitrate silica-gel column for dissolver off-gas treatment of fuel reprocessing. Separation science and technology. 2003; 38(9): 1981-2001.
7. Soelberg NR, Garn TG, Greenhalgh MR, Law JD, Jubin R, Strachan DM, Thallapally PK. Radioactive iodine and krypton control for nuclear fuel reprocessing facilities. Science and Technology of Nuclear Installations. 2013.

8. Herrmann FJ, Motoi V, Fies H, Stojanik B, Furrer J, Kaempffer R. Testing an iodine filter for the vessel off-gas of the German industrial-scale reprocessing plant. Proceedings of the 20th Nuclear Air Cleaning Conference. Boston, MA. 1988.
9. Goossens WRA. New trends in the Belgian programme on nuclear air cleaning technology. Proceedings of the 16th Nuclear Air Cleaning Conference, San Diego, CA. 1980.
10. Scheele RD, Burger LL, Halko BT, Waters ED, Orme RM. Performance of some silver sorbents for control of radioiodine from nuclear fuel operations. Proceedings of the 20th Air Cleaning Conference. Boston, MA. 1988.
11. Bhatia SK, Liu F, Arvind G. Effect of pore blockage on adsorption isotherms and dynamics: anomalous adsorption of iodine on activated carbon. Langmuir. 2000; 16(8): 4001-4008.
12. Zhou J, Hao S, Gao L, Zhang Y. Study on adsorption performance of coal based activated carbon to radioactive iodine and stable iodine. Annals of Nuclear Energy. 2014; 72: 237-241.
13. Scheele RD, Burger LL, Matsuzaki C. Methyl iodide sorption by reduced silver mordenite. Pacific Northwest Laboratory, Richland, WA.1983; Technical Report No. PNL-4489.
14. Burger LL, Scheele RD. The status of radioiodine control for nuclear fuel. Pacific Northwest Laboratory, Richland, WA.1983; Technical Report No. PNL-4689.
15. Scheele RD, Burger LL, Halko BT. Comparison of silver sorbents for application to radioiodine control at the PUREX process facility modification. Pacific Northwest Laboratory, Richland, WA. 1988; Technical Report No. PNL-6607.
16. Scheele RD, Burger LL. Evaluation of silver mordenite for radioiodine retention at the PUREX process facility modification. Pacific Northwest Laboratory, Richland, WA. 1987; Technical Report No. PNL-6261.
17. Burger LL, Scheele RD. Recycle of iodine-loaded silver mordenite by hydrogen reduction. Pacific Northwest Laboratory, Richland, WA.1982; Technical Report No. PNL-4490.
18. Pence DT, Duce FA, Maeck WJ. Iodine Adsorbents Program, Idaho Chemical Programs annual technical report, Fiscal Year 1971. Allied Chemical Corporation, Idaho Falls, ID. 1972; Technical Report No. ICP-1006.
19. Wu L, Sawada JA, Kuznicki DB, Kuznicki T, Kuznicki SM. Iodine adsorption on silver-exchanged titania-derived adsorbents. Journal of Radioanalytical and Nuclear Chemistry. 2014; 302(1): 527-532.
20. Scheele RD, Wend CF. Solidification and stabilization of silver mordenite used to control radioiodine emissions from Hanford's Waste Treatment Plant. Annals of Nuclear Energy. 2015; 78:40-48.
21. Burger LL, Scheele RD, Wiemers KD. Selection of a form for fixation of iodine-129. Pacific Northwest Laboratory, Richland, WA.1981; Technical Report No. PNL-4045.
22. Burger LL, Scheele RD. Iodine fixation studies at the Pacific Northwest Laboratory. In Management modes for iodine-129. 1982.
23. Staples BA, Murphy LP, Thomas TR. Airborne elemental iodine loading capacities of metal zeolites and a dry method for recycling silver zeolite. Proceedings of the 14th Air Cleaning Conference. Sun Valley, ID. 1976.

24. Thomas, TR, Staples BA, Murphy LP. Development of $Ag^{o}Z$ for bulk 129-I removal from nuclear fuel reprocessing plants and PbX for 129-I storage. Proceedings of the 15th Nuclear Air Cleaning Conference. Boston, MA. 1978.

25. Bruffey SH, Jubin RT, Anderson KK, Walker Jr. JF. Aging of iodine-loaded silver mordenite in NO_2. Oak Ridge National Lab, TN. 2010; Technical Report No. ORNL/LTR- 2014/153.

26. Soelberg N, Watson T. Iodine sorbent performance in FY 2012 deep bed tests. Idaho National Laboratory, Idaho Falls, ID. 2012; Technical Report No. FCRD-SWF-2012-000278.

27. Braase, L. Material recovery and waste form development FY 2014 accomplishments report. Idaho National Laboratory, Idaho Falls, ID. 2014; Technical Report No. INL/EXT-14-33548.

28. Paviet-Hartmann P, Kerlin W, Bakhtiar S. Treatment of gaseous effluents issued from recycling–a review of the current practices and prospective. 11th Actinide and Fission Product Partitioning and Transmutation Exchange Meeting, Idaho Falls, ID. 2010; INL/CON-10-19961

29. Chapman KW, Chupas PJ, Nenoff TM. Radioactive iodine capture in silver-containing mordenites through nanoscale silver iodide formation. Journal of the American Chemical Society. 2010; 132(26): 8897-8899.

30. Scheele RD, Wend CF, Buchmiller WC, Kozelisky AE, Sell RL. Preliminary evaluation of spent silver mordenite disposal forms resulting from gaseous radioiodine control at Hanford's Waste Treatment Plant. Battelle-Pacific Northwest Division, Richland, WA. 2002; Technical Report No. PNWD-3225.

31. Zhao H, Nenoff TM, Jennings G, Chupas PJ, Chapman KW. Determining quantitative kinetics and the structural mechanism for particle growth in porous templates. The Journal of Physical Chemistry Letters. 2011; 2 (21): 2742-2746.

32. Aspromonte SG, Mizrahi MD, Schneeberger FA, López JM, Boix AV. Study of the nature and location of silver in Ag-exchanged mordenite catalysts. characterization by spectroscopic techniques. The Journal of Physical Chemistry C. 2013; 117(48):25433-42.

33. Jubin RT, Ramey DW, Spencer BB, Anderson KK, Robinson SM. Impact of Pretreatment and Aging on the Iodine Capture Performance of Silver-Exchanged Mordenite-12314. Paper presented at Waste Management 2012 Conference, Tempe, AZ. 2012.

34. Nan Y, DePaoli DW, Tavlarides LL. Adsorption of radioactive I_2 and tritiated water from spent fuel reprocessing off-gases by reduced silver mordenite. Proceedings of AIChE Annual Meeting. Salt Lake City, UT. 2015, p419963**.**

35. Nan, Y., Tavlarides, L. L. "Adsorption of iodine on hydrogen-reduced silver-exchanged mordenite: Experiments and modeling." *AICHE J.* Aug. 2016. (DOI 10.1002/aic.15432).

36. Lin R, Ladshaw A, Nan Y, Liu J, Yiacoumi S, Tsouris C, DePaoli DW, Tavlarides LL. Isotherms for water adsorption on molecular sieve 3A: influence of cation composition. Industrial & Engineering Chemistry Research. 2015; 54(42): 10442-10448.

37. Lin R, Liu J, Nan Y, DePaoli DW, Tavlarides LL. Kinetics of water vapor adsorption on single-layer molecular sieve 3A: Experiments and modeling. Industrial & Engineering Chemistry Research. 2014; 53: 16015-16024.

38. Aspromonte SG, Miró EE, Boix AV. FTIR studies of butane, toluene and nitric oxide adsorption on Ag exchanged NaMordenite. Adsorption. 2012; 18(1):1-2.

39. Aspromonte SG, Serra RM, Miró EE, Boix AV. AgNaMordenite catalysts for hydrocarbon adsorption and deNO x processes. Applied Catalysis A: General. 2011; 407(1):134-44.

40. Reháková M, Sopková A, Šepelák V, Briančin J, Wadsten T. Natural zeolitic material of the clinoptilolite type and its AgI form. Journal of inclusion phenomena and molecular recognition in chemistry. 1995; 23(2): 157-163.

41. Perrott CM, Fletcher NH. Heat capacity of silver iodide. I. Experiments on annealed samples. The Journal of Chemical Physics. 1968; 48(5): 2143-2148.

42. Perrott CM, Fletcher NH. (1968). Heat capacity of silver iodide. II. Theory. The Journal of Chemical Physics. 1968; 48(6): 2681-2688.

43. Ishida M, Wen CY. Comparison of kinetic and diffusional models for solid-gas reactions. AIChE Journal. 1968; 14(2): 311-317.

44. Levenspiel O, Chemical Reaction Engineering, 3rd Edition. Wiley, New York: John Wiley & Son,Inc., 1999.

45. Ruthven, DM. Principles of adsorption and adsorption processes (1st edition). New York: John Wiley & Son,Inc., 1984.

46. Jubin RT. The mass transfer dynamics of gaseous methyl-iodide adsorption by silver-exchanged sodium mordenite. Ph.D dissertation. The University of Tennessee. 1994.

47. Ranz WE, Marshall WR. Evaporation from drops. Chem Eng Progress. 1952; 48: 141-146.

48. Poling BE, Prausnitz JM, O'connell JP. The properties of gases and liquids (5th edition). New York: McGraw-Hill, 2000.

49. Lemmon EW, Huber ML, McLinden MO. NIST standard reference database 23: Reference fluid thermodynamic and transport properties – REFPROP, Version 9.0. 2010.

50. Ladshaw A., Yiacoumi S., Tsouris C. and DePaoli D., Generalized gas–solid adsorption modeling: Single-component equilibria. Fluid Phase Equilibria, 388, pp.169-181. 2015

51. Ladshaw A., Yiacoumi S. and Tsouris C. A generalized procedure for the prediction of multicomponent adsorption equilibria. AIChE Journal, 61(8), pp.2600-2610, 2015

52. Nan Y, Ladshaw AP, Yiacoumi S, Tsouris C, DePaoli DW., Tavlarides, L. L. "Co-adsorption of I2 and H2O on Ag0Z" Proceedings of 2016 AIChE Annual Meeting, San Francisco, CA, November 2016.

53. Nan Y, DePaoli DW, Tavlarides LL. "Adsorption of iodine and water on reduced silver-exchanged mordenite" 19th Symposium on Separation Science and Technology for Energy Applications, Gatlinburg, TN, October 2016.

54. Gleuckauf E.; Coates JI. Theory of chromatography. Part IV. The influence of incomplete equilibrium on the front boundary of chromatograms and on the effectiveness of separation. *J* Chem Soc., 0, 1315-1321 (1947).

55. Nan Y., Ladshaw AP, Yiacoumi S, Tsouris C, DePaoli, DW, Tavlarides, LL. “Co-adsorption of I2 and H2O on Ag0Z and Kinetics of Silver-Iodine Reaction” American Nuclear Society Annual Meeting, New Orleans, LA, June 2016

2. Modeling of adsorption processes for off-gas treatment

2.1 Key personnel

Sotira Yiacoumi (co-PI), Costas Tsouris (co-PI), Austin Ladshaw (Graduate Student), Alexander Wiechert (Graduate Student); Georgia Institute of Technology

2.2 Scope

Adsorption is a complex physicochemical process involving interparticle transport, interphase mass-transfer, intraparticle diffusion, and surface reactions. Although the exact description of the adsorption process will inevitably vary from system to system, it will always be governed by those primary mechanisms. Therefore, by devising a model framework that can inherently include those mechanisms, it would be possible to create a modeling platform on which many different adsorption problems could be solved numerically. To accomplish this task, a generalized conservation law model was created to include the necessary mechanisms of adsorption on several different geometrical domains. That model was then discretized using a high-resolution finite-differences scheme and solved numerically with a non-linear iterative method. Specific model applications for adsorption were developed under that framework and validated using data available in literature. The model demonstrations also highlight the generality and flexibility of the framework approach at modeling other adsorption systems. This modeling platform makes it easier to model various adsorption problems and develop new adsorption models because of the common treatment of the mathematics governing the physical processes.

2.3 Modeling Approach

2.3.1 Introduction

In environmental and chemical engineering applications of adsorption, the majority of the physicochemical processes studied are governed by a conservation law (Tien, 1994; Tóth, 2002). Adsorption modeling typically involves the coupling of mass and energy balances of some material over a given domain. For example, if micro-porous diffusion of adsorbates into an adsorbent particle were to be investigated, the physical process would be described via a mass balance in a spherical coordinate system as in Equation 1 (Tien, 1994):

$$r^2 \varepsilon \frac{\partial C}{\partial t} = \frac{\partial}{\partial r}\left[r^2 D \varepsilon \frac{\partial C}{\partial r} \right] \tag{1}$$

In this system, the concentration of the adsorbate (C) is the conserved quantity, and the micro-pore diffusivity (D) and micro-porosity of the material (ε) are parameters of the model.

Alternatively, if one were interested in observing the axial temperature profile of a gas stream through a column, then the mathematical description of that process would be an energy balance in Cartesian coordinates as in Equation 2:

$$(h\rho)\frac{\partial T}{\partial t}+\frac{\partial}{\partial z}(h\rho vT)=\frac{\partial}{\partial z}\left(K\frac{\partial T}{\partial z}\right) \tag{2}$$

The parameters of this model equation include gas heat capacity (h), gas density (ρ), fluid velocity (v), and thermal conductivity (K) as the physical parameters.

These two equations are mathematically very different, but are formulated from the same governing principles and are very common types of problems that one might encounter in adsorption. To dig deeper into the mathematics, consider the four primary mechanisms of adsorption as depicted in Figure 1. These mechanisms are all common to every type of adsorption problem that one may seek to model.

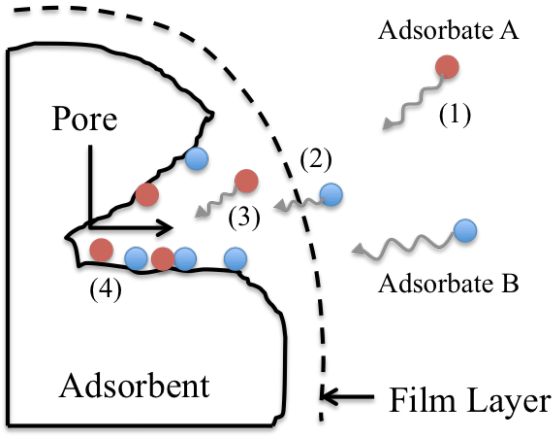

Figure 28: Mechanisms of adsorption: (1) interparticle transport, (2) interphase mass-transfer, (3) intraparticle diffusion, and (4) surface reaction and equilibria. These mechanisms are common to all adsorption problems.

Adsorption, by its nature, is inherently a multi-species and multi-scale process involving (1) interparticle transport, (2) interphase mass transfer, (3) intraparticle diffusion, and (4) surface reactions and equilibria (Tien, 1994). At the macro-scale, the primary interest is in interparticle transport, which is how the adsorbates travel between adsorbent particles. This process is governed primarily by advection and molecular diffusion (Tien, 1994; Simo et al., 2009). For the micro-scale, adsorption is governed by film mass transfer from bulk solution to the outside of the adsorbent, pore and surface diffusion inside the adsorbent domain, and surface reactions or adsorption equilibria (Gorbach et al., 2004; Lin et al., 2014). To model these mechanisms requires a mass balance on each adsorbate as it travels between, around, and inside the particles. In other words, the model is required to include multiple mechanisms on multiple scales for multiple species.

This modeling undertaking is comprised of several parts. First, approaching this problem as generally as possible requires the development of a framework under which the majority of adsorption problems can be placed. For this to be accomplished, the model must be capable of describing the process under various geometrical domains, inherently allow parameters to vary in space and time, and include terms for multiple physical processes that may be present in the system. Then, the model must be discretized into a solvable form using either direct or iterative techniques. Therefore, one must also incorporate linear and non-linear solvers into the framework that can be adapted into the generalized conservation law to solve the resulting system at each time step. The culmination of all these parts will provide a robust mechanistic adsorption model.

2.3.2 Model Framework

A Generalized 1-D Conservation Law Model

There are several terms that one may need to include in a general conservation law: advection, diffusion, reaction, etc. Each of these terms needs to be flexible enough so that they can be allowed to vary in space and time. Additionally, there may also be a variety of spatial domains over which the problems exist in space (e.g., spherical, cylindrical, Cartesian). From Equations 1 and 2, it has been shown that there are cases in which one wants to solve conservation laws in different geometries and may even leave out certain physical terms altogether. Based on these considerations, a Generalized 1-D Conservation Law Model (Equation 3) has been formulated in this work.

$$z^d R\frac{\partial u}{\partial t}+\frac{\partial}{\partial z}\left(z^d v u\right)=\frac{\partial}{\partial z}\left(z^d D\frac{\partial u}{\partial z}\right)-z^d k u-z^d S \tag{3}$$

In this form of the conservation law, the conserved quantity is denoted by the variable u. This can be any conserved quantity that one wants to observe and will depend on a number of space-time dependent parameters, which all have a different physical interpretation. R is a retardation coefficient, v is an advective velocity, D is for dispersion, k is a reaction coefficient, and S can be some generic source/sink term or other forcing function.

The spatial quantity z, along with its exponent portion d, is used to change the geometry of the physical domain upon which observations of u are made. This is shown by a simple inspection: if d=0 in Equation 3 and the reaction and source terms are removed, then the form of the equation is exactly that of Equation 2. Likewise, if the advection term is removed and d=2, then the form of the equation now matches that of Equation 1. Therefore, one can easily switch between Cartesian, polar, and spherical coordinates just by changing the value of a single argument (d) from 0 to 1 to 2.

Similarly, different physical terms from Equation 3 can be neglected or removed simply by setting all space-time values of the corresponding coefficient to zero. For example, if one wanted to solve a steady-state reaction-diffusion problem in a cylindrical geometry, this would be accomplished by setting d=1 and then setting the R, v, and S parameters to all zeros. Solving the resulting system would then show the steady-state profile of u distributed radially in a

cylinder. Therefore, by formulating the equations in this manner, one can set up a simple approach to modeling different adsorption processes.

Discretization of the Conservation Law Problem

Since the problem (Equation 3) is one-dimensional, it will be easiest to use a finite difference approach to numerically solve the conservation law. In order to handle problems that may be advectively dominated, it is advantageous to use a particular finite difference method known as a Monotonic Upstream-centered Scheme for Conservation Laws (MUSCL). These discretization schemes were first introduced by Bram van Leer in 1979, and have since been the leading approach for these types of problems. A particular MUSCL scheme of interest is the Kurganov and Tadmor (KT) scheme for its high accuracy and applicability for both linear and non-linear conservation laws (Kurganov and Tadmor, 2000).

The KT scheme uses the concept of *slope limiting*, or *flux limiting*, to reconstruct the edge fluxes at the boundaries of each cell in the discretized mesh (Figure 2 and Equation 4). By taking this approach, one can ensure that the quantity u is conserved across the entire domain, as overflow from one cell would feed into the next cell. Additionally, to maintain a high resolution and accuracy, the KT scheme also includes a correction term for numerical dispersion, which seeks to penalize the discretization based on the local maximum wave speed (Equation 5). This allows the scheme to better handle shocks and discontinuities that may be present in the solution (Kurganov and Tadmor, 2000).

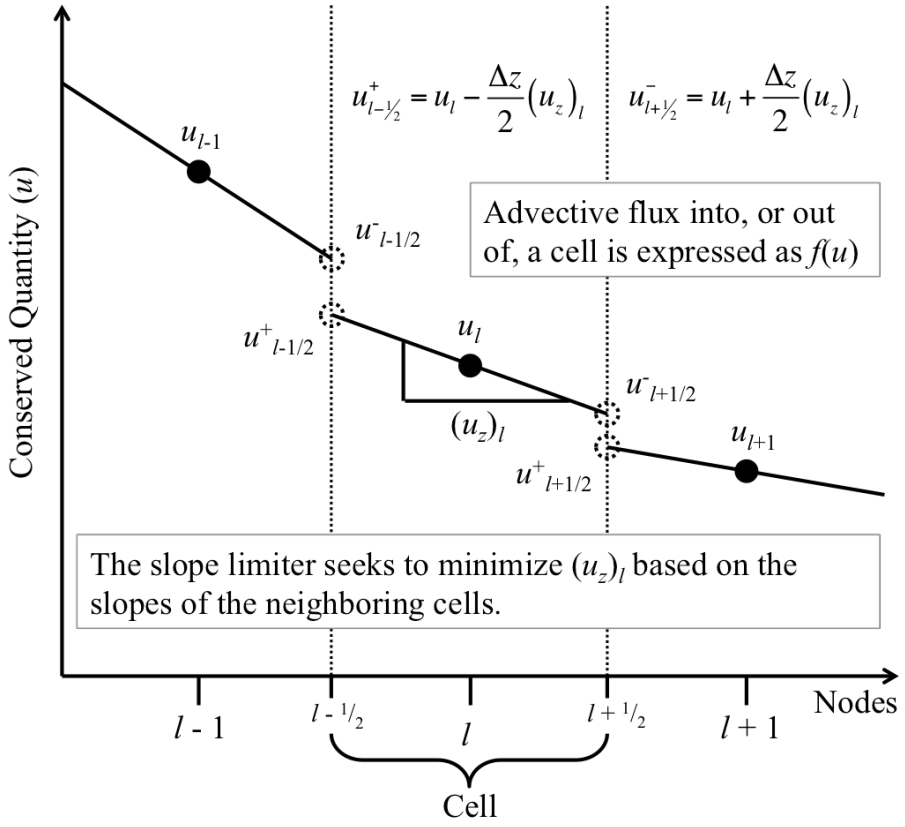

Figure 29: Visualization of the process of flux reconstruction on a 1-D mesh.

$$H_{l+½} = \frac{1}{2}\left[f\left(u^{+}_{l+½}\right) + f\left(u^{-}_{l+½}\right)\right] \tag{4}$$

$$p_{l+½} = \frac{a_{l+½}}{2}\left[u^{+}_{l+½} - u^{-}_{l+½}\right] \tag{5}$$

In the above equations, $H_{l+1/2}$ is the average advective flux leaving cell l from the right, $p_{l+1/2}$ is the penalty term applied for the jump discontinuity at the right boundary of the cell, and $f(u)$ is the advective flux term into or out of the cell. Note that u_z in the figures and equations represents the derivative of u with respect to z (du/dz). The magnitude of that penalty is based on the jump, as well as the local maximum wave speed ($a_{l+1/2}$). Using the same procedure for the left side boundary of the cell, then applying a centered finite difference approximation to the derivative of the advective term will produce the overall advective flux discretization shown in Equation 6 (Kurganov and Tadmor, 2000).

$$\frac{\partial}{\partial z} f(u)_l \cong \frac{\left(H_{l+½} - p_{l+½}\right) - \left(H_{l-½} - p_{l-½}\right)}{\Delta z} \tag{6}$$

According to Kurganov and Tadmor (2000), the maximum local wave speed is equivalent to the maximum spectral radius of the Jacobian of $f(u)$ over all u within the discretized sub-domain. In general, this may be difficult to estimate, especially if $f(u)$ is complex. Therefore, a simpler approximation to this term is provided within this framework. For the application considered here, the advective term is always of the form $f(u) = z^d v u$. From this formulation, one can make a simple observation; if the parameter v is not a function of u, then the Jacobian of the function will be constant with respect to u, and the maximum wave speed will always be of the form $a = z^d v$. This should work well for most of the problems of interest.

After discretizing the advective flux term of Equation 3, one can use a centered-difference discretization for the rest of the terms within the conservation law and develop a simple semi-discrete form, as shown in Equation 7. Note that, since the advective coefficient (v) is a vector, the equations have been discretized in such a way as to allow for the direction of flow in the domain to change between positive and negative. Additionally, the terms in the discretization have been rearranged such that it is easy to differentiate between the nodal quantities (u) and their gradients (u_z). This is done so that it is easier to split the system between its pseudo-linear and non-linear parts, since the gradients of u are where the slope limiters will be applied.

Grouping the terms of Equation 7, one can simplify the semi-discrete form into parameters for left, center, and right side terms for nodal and gradient fluxes (N_L, N_C, N_R, G_L, G_C, and G_R) as shown in Equation 8. From this point, all that is needed is to apply boundary conditions and choose a time integration scheme. For this particular framework application, two different input boundary conditions are allowed: (i) Dirichlet and (ii) Neumann (Equations 9 and 10). Those conditions are applied at the input of the domain, while the output uses the zero flux boundary condition (Equation 11). The time integration scheme will either be Crank-Nicolson

for the accuracy or Backwards Euler for the stability and will be chosen by the framework when a simulation is being run.

$$
\begin{aligned}
& z_l^d R_l \frac{d}{dt}(u_l) = \\
& \left[\frac{z_{l-\frac{1}{2}}^d D_{l-\frac{1}{2}}}{\Delta z^2} + \frac{z_{l-\frac{1}{2}}^d \left(v_{l-\frac{1}{2}} + \left| v_{l-\frac{1}{2}} \right| \right)}{2\Delta z} \right] u_{l-1} \\
& - \left[\frac{z_{l+\frac{1}{2}}^d D_{l+\frac{1}{2}}}{\Delta z^2} + \frac{z_{l-\frac{1}{2}}^d D_{l-\frac{1}{2}}}{\Delta z^2} + \frac{z_{l+\frac{1}{2}}^d \left(v_{l+\frac{1}{2}} + \left| v_{l+\frac{1}{2}} \right| \right)}{2\Delta z} - \frac{z_{l-\frac{1}{2}}^d \left(v_{l-\frac{1}{2}} - \left| v_{l-\frac{1}{2}} \right| \right)}{2\Delta z} + z_l^d k_l \right] u_l - z_l^d S_l \\
& + \left[\frac{z_{l+\frac{1}{2}}^d D_{l+\frac{1}{2}}}{\Delta z^2} - \frac{z_{l+\frac{1}{2}}^d \left(v_{l+\frac{1}{2}} - \left| v_{l+\frac{1}{2}} \right| \right)}{2\Delta z} \right] u_{l+1} \\
& + \left[\frac{z_{l-\frac{1}{2}}^d \left(v_{l-\frac{1}{2}} + \left| v_{l-\frac{1}{2}} \right| \right)}{4} \right] (u_z)_{l-1} \\
& - \left[\frac{z_{l+\frac{1}{2}}^d \left(v_{l+\frac{1}{2}} + \left| v_{l+\frac{1}{2}} \right| \right)}{4} + \frac{z_{l-\frac{1}{2}}^d \left(v_{l-\frac{1}{2}} - \left| v_{l-\frac{1}{2}} \right| \right)}{4} \right] (u_z)_l \\
& + \left[\frac{z_{l+\frac{1}{2}}^d \left(v_{l+\frac{1}{2}} - \left| v_{l+\frac{1}{2}} \right| \right)}{4} \right] (u_z)_{l+1}
\end{aligned}
\tag{7}
$$

$$
\begin{aligned}
z_l^d R_l \frac{d}{dt}(u_l) = & \left[N_L \right]_l u_{l-1} - \left[N_C \right]_l u_l + \left[N_R \right]_l u_{l+1} \\
& + \left[G_L \right]_l (u_z)_{l-1} - \left[G_C \right]_l (u_z)_l + \left[G_R \right]_l (u_z)_{l+1} - z_l^d S_l
\end{aligned}
\tag{8}
$$

$$
u\big|_{z=0} = u_{in} = u_0 \tag{9}
$$

$$
D \frac{\partial u}{\partial z}\bigg|_{z=0} = -v(u_{in} - u_0) \tag{10}
$$

$$
\frac{\partial u}{\partial z}\bigg|_{z=L} = 0 \tag{11}
$$

Applying the Slope Limiters

Slope limiters are functions applied to the gradient of the solution vector u in order to reduce the advent of oscillations around sharp or discontinuous portions of the solution. They are required for any high-resolution scheme for fluid dynamics or advectively dominant conservation laws. Unfortunately, there is no slope limiter function that is linear, thus one must introduce some non-linear portions into this simple scheme.

There are several different kinds of slope limiter functions available, each with their own advantages and disadvantages. Kurganov and Tadmor (2000) used a generalized minmod slope limiter for their own scheme (Equation 12). This slope limiter includes a ϑ parameter that can vary between 1 and 2, 1 being most dispersive and most stable while 2 is least dispersive and least stable. The most attractive feature of this slope limiter is that it is optimal in the sense that it provides the true minimum of the gradient of u for the scheme. However, since this slope limiter is non-differentiable, it may have very poor convergence properties when using an iterative solution method.

$$\left(u_z\right)_l = \text{minmod}\left\{\vartheta\frac{u_l - u_{l-1}}{\Delta z}, \frac{u_{l+1} - u_{l-1}}{2\Delta z}, \vartheta\frac{u_{l+1} - u_l}{\Delta z}\right\} \tag{12}$$

To overcome any potential convergence issues that may arise requires the inclusion of a class of slope limiters that are differentiable and continuous on a given sub-domain. This can be represented by Equations 13 and 14, wherein $\phi(g_l)$ is a slope limiter function that varies between 0 and 1 to convert the scheme from low to high resolution, depending on the slopes of the surrounding cells. If the neighboring slopes are smooth, then the scheme's resolution is high, whereas if the neighboring slopes are sharp or discontinuous, the scheme reverts to a lower order, upwind-like scheme to reduce oscillations around the sharp wave. For this particular application, both the minmod slope limiter (Equation 12) and the van Albada slope limiter (van Albada et al., 1982) will be considered (Equation 15).

$$(u_z)_l = \begin{cases} \left(1-\phi(g_l)\right)\left(\frac{u_l - u_{l-1}}{\Delta z}\right) + \phi(g_l)\left(\frac{u_{l+1} - u_{l-1}}{2\Delta z}\right) & v_l > 0 \\ \left(1-\phi(g_l)\right)\left(\frac{u_{l+1} - u_l}{\Delta z}\right) + \phi(g_l)\left(\frac{u_{l+1} - u_{l-1}}{2\Delta z}\right) & v_l \le 0 \end{cases} \tag{13}$$

$$g_l = \frac{u_l - u_{l-1}}{u_{l+1} - u_l} \tag{14}$$

$$\phi(g) = \frac{g^2 + g}{g^2 + 1} \tag{15}$$

Solution Methodology

After formulating the semi-discrete form (Equation 8) and choosing a slope limiter, one must still solve the resulting system of equations. Depending on the particular problem and the presence of, or lack thereof, an advective term, the resulting problem may be linear or non-linear. The exact form of the problem, however, will never actually be known until a particular

simulation case is chosen. Therefore, it is best to solve the system numerically with a non-linear scheme, which is the most generic approach.

For multi-physics problems derived from spatial discretizations, Newton methods can be computationally inexpensive and effective iterative approaches for non-linear problems (Knoll and Keyes, 2004). This class of methods is particularly useful for the problem of interest because the linear iterations can be preconditioned, or solved approximately, based on the linearization of the semi-discrete model (Equation 8) in order to accelerate convergence. In essence, what the framework does is solve the system linearly and use the linear solution as the basis for the non-linear iterations.

2.3.3 Models for Specific Systems

2.3.3.1 Bi-porous Pellet Kinetics

One of the most common configurations for commercial adsorbent pellets is a two-phase, heterogeneous structure composed of a macro-porous binder material holding together a collection of micro-porous adsorbent crystals. The binder material typically behaves as an inert conduit by which adsorbates can travel through the pellet to reach the adsorption sites on the adsorbent crystals. Upon reaching the crystals, the adsorbates can adsorb and travel deeper into the crystals via a surface diffusion mechanism (Tien, 1994). An idealized bi-porous adsorbent pellet is shown in Figure 3 below.

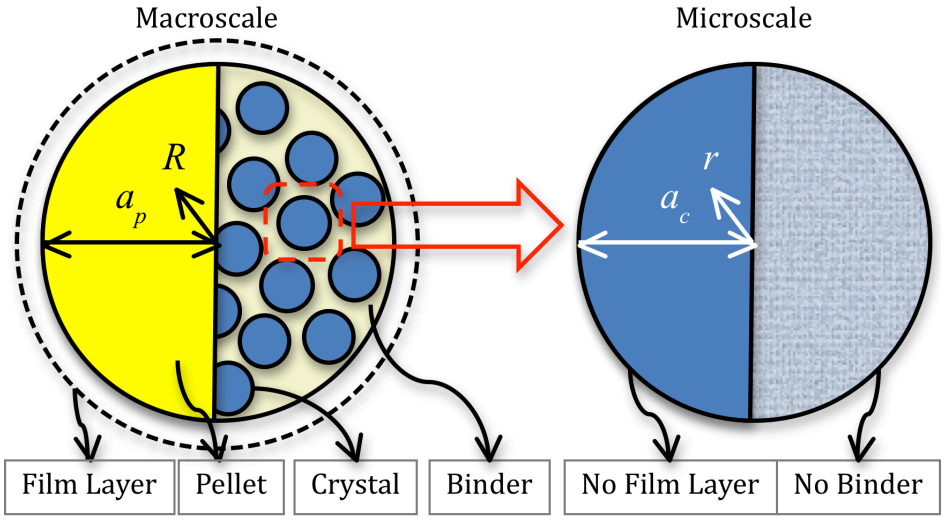

Figure 30: Diagram showing the idealization of a commercial, bi-porous adsorbent made up of a collection of micro-porous adsorbent crystals held together by an inert, macro-porous binder.

The mechanisms involved with these types of adsorbents include (i) mass transfer across the film layer, (ii) macro-pore diffusion through the binder material, (iii) adsorption on the crystals, and (iv) surface diffusion through the micro-porous adsorbent crystals (Tien, 1994). Because the different diffusion processes happen in separate regions of the adsorbent and on

different physical scales, a multi-scale physics problem is created that must be resolved using multiple material balances. Each material balance resolves the transport of material on the different scales of the problem and requires a different partial differential equation. The system governing all these mechanisms is outlined in Equations 16 through 20.

$$\frac{\partial q}{\partial t} = \frac{1}{r^2}\frac{\partial}{\partial r}\left[r^2 D_c \frac{\partial q}{\partial r}\right] \tag{16}$$

$$q\big|_{r=a_c} = f(c) \tag{17}$$

$$\overline{q} = \frac{3}{a_c^3}\int_0^{a_c} q r^2\, dr \tag{18}$$

$$\varepsilon_p \alpha \frac{\partial c}{\partial t} + \rho_s \frac{\partial \overline{q}}{\partial t} = \frac{1}{R^2}\frac{\partial}{\partial R}\left[R^2 D_p \varepsilon_p \alpha \frac{\partial c}{\partial R}\right] \tag{19}$$

$$D_p \frac{\partial c}{\partial R}\bigg|_{R=a_p} = k_f (C_b - c) \tag{20}$$

On the micro-scale, the material balance (Equation 16) is governed by the diffusivity of adsorbates through the crystal (D_c). Each crystal is assumed to be spherical in shape with a nominal radius of a_c. Adsorption occurs on the outside domain of each crystal (Equation 17) and is governed by the adsorption isotherm, which is some function of the local pore space concentration of the adsorbates (c). The average adsorption ($\overline{q}$) in each crystal is resolved as an integral over each crystal domain (Equation 18) and becomes part of the macro-scale problem in Equation 19.

The macro-scale problem is controlled by pore diffusion (D_p), film mass transfer (k_f), and mass removed through the average adsorption term that is being controlled by the micro-scale. The movement of adsorbate from bulk solution (C_b) to the interior of the pellet (c) is driven by the concentration difference at the boundary (Equation 20). Rates at which the adsorbates move throughout the macro-porous binder material are further modulated by the porosity of that binder material (ε_p), the adsorbent density (ρ_s), and the fraction of the pellet that is binder material (α).

Although this bi-porous structure is common for many commercial pellets, it is not always necessary to model the adsorption mechanisms in this much detail. For instance, one may want to ignore the micro-scale diffusion portion of this problem and consider the average adsorption to just be a function of local equilibria in the pellet, which is dictated by the isotherm. To do this only requires changing the micro-scale adsorption function to the adsorption isotherm (Equation 17). Or perhaps the pellets are actually extruded cylinders instead of compressed bi-porous spheres. Under the generalized framework, it is very simple to change coordinate systems from spherical to cylindrical. This is accomplished simply by changing the value of dimensional parameter d (Equation 3) from 2 to 1.

2.3.3.2 Mass and Energy Transport in Fixed Beds

This modeling framework is also well suited for simulating mass and energy transfer during adsorption in a fixed-bed column. Fixed beds are the typical engineered adsorption

systems for the separation or recovery of dilute gases (Simo et al., 2009; Gorbach et al., 2004). They are generally cylindrical columns packed with adsorbent pellets held in place by some form of screen so that gas is allowed to pass through the system. In some cases, the outer walls of those columns are thermally controlled and, often times, the length of those columns is much larger than their diameter. In these cases, it is very suitable to model the mass and energy balance in one-dimension, since there will be very minor changes in the radial distribution of mass and heat (Tien, 1994).

The mass balance portion of the fixed-bed model is driven primarily by the interparticle transport mechanisms of advection and dispersion (Equation 21). Additionally, there is a sink term for gas phase losses caused by adsorption. Adsorption taking place in this model can be in terms of local equilibria or in terms of the kinetics of adsorption, such as bi-porous kinetics in the case of engineered commercial pellets (Equations 16 through 20). The parameters involved with mass transport include superficial gas velocity (v), bulk bed porosity (ε_b), axial dispersion (D_z), and bulk bed solids density (ρ_b). At the inlet boundary to the fixed-bed, mass flow into the problem domain is governed by the flow rate and the concentration gradient formed at the entrance to that domain between the inlet concentration (C_{in}) and the concentration inside the bed (Equation 22).

$$\varepsilon_b \frac{\partial C}{\partial t} + \frac{\partial}{\partial z}\left(\varepsilon_b v C\right) = \frac{\partial}{\partial z}\left(\varepsilon_b D_z \frac{\partial C}{\partial z}\right) - \rho_b \frac{\partial q}{\partial t} \tag{21}$$

$$D_z \left.\frac{dC}{dz}\right|_{z=0} = v\left(C_{in} - C\right) \tag{22}$$

For this model, one may also want to track how the temperature of the gas changes with adsorption. This requires the development of an energy balance between gas and solid phases as material moves through the bed and as adsorption occurs (Tien, 1994; Simo et al., 2009). The energy balance involves similar boundary conditions and mechanisms to that of the mass balance (Equations 23 and 24), but also includes thermal conductivity, heat transfer from the walls of the columns, and heats of adsorption. Since radial changes in temperature and concentration are being neglected in the 1-D case, the effect of the heating of the wall is done on an average basis. The parameters in this energy balance include heat capacity of the gas (h_g), density of the gas (ρ), heat capacity of the adsorbents (h_s), axial thermal conductivity (K_z), heat of adsorption (Q_{st}), temperature of the wall (T_w), heat transfer coefficient between the wall and the interior gases (U_w), and the inner diameter of the column (d_{in}).

$$\left(h_g \rho \varepsilon_b + h_s \rho_b\right)\frac{\partial T}{\partial t} + \frac{\partial}{\partial z}\left(h_g \rho \varepsilon_b v T\right) = \frac{\partial}{\partial z}\left(\varepsilon_b K_z \frac{\partial T}{\partial z}\right) + \rho_b \frac{\partial (Q_{st} q)}{\partial t} + \frac{4U_w}{d_{in}}\left(T_w - T\right) \tag{23}$$

$$K_z \left.\frac{dT}{dz}\right|_{z=0} = h_g \rho v\left(T_{in} - T\right) \tag{24}$$

These material balances (Equations 21 through 24) make up the bulk of the fixed-bed adsorption model. To resolve the actual amount of adsorption (q) occurring in the column, one could either assume local equilibria (i.e., apply the adsorption isotherm at each spatial location in

the domain) or use an adsorption kinetics model, such as the bi-porous pellet model. Combining the actual adsorption kinetics with these equations for mass and energy transfer creates a fully coupled model for adsorption in engineered systems.

2.3.4 Estimating Model Parameters

All the models discussed involve many different physical parameters ranging from thermal capacities to various types of diffusion. Some of these values, such as pellet density (ρ_s) and wall heat transfer coefficients (U_w), can be found by looking at various tables or published data for similar systems or particular materials (Simo et al., 2009; Gorbach et al., 2004). Other parameters, such as surface diffusion (D_c), may only be determined through experiments or listed in literature for a particular system. However, a bulk of the model parameters can be approximated through theoretical and semi-empirical considerations.

Many of the parameters involved in the bi-porous pellet kinetics model can be determined independently. Tien (1994) offers several techniques and expressions for determining the pellet diffusivity (D_p) and mass-transfer coefficient (k_f) based on the system parameters (Equations 25 through 28). The parameters for Equations 25 through 28 are as follows: ε_p is pellet porosity, τ is tortuosity, D_m is molecular diffusivity, D_k is Knudsen diffusivity, D^o_p is the idealized pore diffusivity, D_p is the corrected pore diffusivity, r_p is nominal pore radius, T is temperature, MW is molecular weight of adsorbing species, Re is the Reynolds number, and Sc is the Schmidt number.

Actual pore diffusivity (Equation 27) inside the adsorbent pellet is controlled by both Knudsen diffusion (Equation 26) and molecular diffusion, which is modified by the tortuous path that molecules take through the macro-porous binder material (Equation 25). The film mass-transfer coefficient can be approximated through empirical relationships with the dimensionless Reynolds and Schmidt numbers, along with the molecular diffusivity in the gas phase (Equation 28).

$$D_p^o = \frac{\varepsilon_p D_m}{\tau} \tag{25}$$

$$D_k = 9700 r_p \left(\frac{T}{MW}\right)^{1/2} \tag{26}$$

$$\frac{1}{D_p} = \frac{1}{D_p^o} + \frac{1}{D_k} \tag{27}$$

$$k_f = \frac{D_m}{2a_p}\left[2 + 1.1 Re^{0.6} Sc^{0.3}\right] \tag{28}$$

Each species in a gas mixture will have a different molecular diffusivity ($D_{m,i}$) that can be determined from the binary diffusivities (D_{ij}) between all species present (Equation 29). The binary diffusivities vary theoretically with temperature and the viscosity (μ_i), density (ρ_i), and molecular weight (MW_i) of each species according to Equation 30 (Wilke, 1950). Temperature relationships for the density of each species can be determined using the ideal gas law (Equation

31), and the Sutherland's equation (Equation 32) can be used to relate the viscosity of each pure species with temperature (Sutherland, 1893) using a reference state viscosity (μ_i^o) and temperature (T_i^o), as well as the Sutherland's constant (X_i). Combining all these theoretical models, then, allows one to accurately estimate the influence of diffusivity on the kinetics of adsorption.

$$D_{m,i} = \frac{1 - y_i}{\sum_{j \neq i} \frac{y_j}{D_{ij}}} \tag{29}$$

$$D_{ij} = \frac{(4/\sqrt{2})(MW_i^{-1} + MW_j^{-1})^{1/2}}{\left[\left(\frac{\rho_i^2}{1.92\mu_i^2 MW_i}\right)^{1/4} + \left(\frac{\rho_j^2}{1.92\mu_j^2 MW_j}\right)^{1/4}\right]^2} \tag{30}$$

$$\rho_i = \frac{P_T MW_i}{RT} \tag{31}$$

$$\mu_i = \mu_i^o \frac{T_i^o + X_i}{T + X_i}\left(\frac{T}{T_i^o}\right)^{3/2} \tag{32}$$

The Reynolds and Schmidt numbers (Equations 33 and 34) are also implicit functions of temperature and pressure (Wakao and Funaizkri, 1978) because they relate the kinematic viscosity (v_g) and diffusivity of the gas with the gas velocity (v) and size of the particles (a_p). To determine the kinematic viscosity of the mixed gas system requires the total dynamic viscosity of the gas (μ_g) and the total density of the gas phase (ρ). While the total density can be determined from the ideal gas law, the dynamic viscosity of the mixed gas must be determined from a theoretical model, such as that outlined in Equations 35 through 37 (Krieger, 1951). This model takes into account the mole fractions (y_i) of each species together with the binary diffusivities and a temperature correction factor (χ) to approximate the mixed gas viscosity.

$$Re = \frac{2u_s a_p}{\nu_g} \tag{33}$$

$$Sc_i = \frac{\nu_g}{D_{ij}} \tag{34}$$

$$\mu_g = \sum_{i=1}^{N} \frac{\mu_i}{1 + \frac{113.65\chi\mu_i T}{y_i MW_i}\sum_{\substack{j=1 \\ j\neq i}}^{N} \frac{y_i}{D'_{ij}}} \tag{35}$$

$$\chi = 0.873143 + (7.2375 \times 10^{-5})T \tag{36}$$

$$P^o D'_{ij} = P_T D_{ij} \tag{37}$$

Using all these relationships allows for reasonable approximation of many of the parameters involved in the bi-porous pellet kinetics model. For the fixed-bed model, many of the parameters of the energy balance (Equation 23), including wall heat transfer coefficient and heat capacities of materials, can be determined by looking up the properties of the specific materials

involved. The heat of adsorption (Q_{st}) is typically determined through the isotherm or through experiments (Llano-Restrepo and Mosquera, 2009; Ladshaw et al., 2015a).

For the mass balance portion of the fixed-bed model, the axial dispersion coefficient can be approximated through an empirical relationship with the Reynolds and Schmidt numbers (Equation 38) in a similar fashion to how the film mass transfer coefficient was determined (Rutledge, 2013; Simo et al., 2009). Most other parameters in the fixed-bed model, notably the thermal parameters such as heat capacities, conductivities, and heat transfer coefficients, must be looked up in tables or determined experimentally.

$$D_z = 2va_p\left[\frac{20}{Sc\cdot Re}+\frac{1}{2}\right] \tag{38}$$

2.3.5 Equilibria Isotherm Model

The final piece of information necessary for modeling adsorption kinetics and transport is the isotherm. Isotherms describe the relationship between the adsorbed phase and the gas phase at equilibrium. There is a variety of different adsorption models available in literature: Langmuir, Freundlich, Tóth, etc. The individual choice of isotherm will depend on the suitability of the model for describing the partition between gas and solid phases across a variety of temperatures and pressures (Ladshaw et al., 2015a).

For the work considered here, the Generalized Statistical Thermodynamic Adsorption (GSTA) isotherm model (Llano-Restrepo and Mosquera, 2009) was chosen as the equilibria model. This isotherm is very flexible and has been shown to be useful at describing the adsorption equilibria of many different systems (Ladshaw et al., 2015a; Lin et al., 2015). Additionally, this model has also been employed in mixed-gas adsorption equilibria models with great success (Ladshaw et al., 2015b). Isotherm parameters for all systems that have been modeled here were determined through an iterative procedure described in Ladshaw et al. (2015a).

2.4 Kinetic Adsorption Data Acquisition at SU

2.4.1 Adsorbents

To demonstrate the capability of the model framework for different adsorption systems, kinetic data of water vapor adsorption with a zeolite molecular sieve 3A (MS3A) and iodine gas adsorption with a reduced silver mordenite (Ag^0Z) were analyzed. MS3A is one of the classic adsorbents for removing water in gas and liquid streams, and Ag^0Z is the most promising material for iodine capture in spent nuclear fuel reprocessing plants. Both solid adsorbents were micro-porous crystalline alumina silicates that have micro pores and channels in the crystals. The commercial MS3A that were used in prior studies (Lin et al., 2014) were spherical beads with a radius of 1.18 mm, and the Ag^0Z used were in prior studies were extruded cylinders with a radius of 0.8 mm (Nan et al., 2016).

The silver mordenite contained 11.9 wt.% silver and was reduced prior to adsorption experiments in a hydrogen/argon stream at 400 ^oC and for 24 hours to achieve a better iodine

adsorption performance. Previous studies have shown that silver ions inside the mordenite crystals were reduced to metallic silver and formed silver nanoparticles on the surface of the crystals during the reduction by hydrogen (Chapman et al., 2010; Zhao et al., 2011; Aspromonte et al., 2013; Nan et al. 2016). Physical properties and chemical characteristics of the MS3A and Ag^0Z were described previously (Lin et al., 2014; Nan et al., 2016). In addition to those reported properties, the average macropore radii of MS3A and Ag^0Z were measured in this work using mercury porosimetry, which were 35 nm and 26.5 nm, respectively. Tables 1 and 2 below provide some important structural and physical parameters for modeling adsorption kinetics in both MS3A and Ag^0Z adsorbents.

Table 1: Structure parameters for the MS3A zeolite

Description	Variable	Value	Units
Crystal Radius	a_c	1.5	μm
Pellet Radius	a_p	1.18	mm
Macro-pore Radius	r_p	35	nm
Adsorbent Density	ρ_s	1.69	g/cm^3
Macro-porosity	ε_p	0.272	-
Binder Fraction	α	0.175	-

Table 2: Structure parameters for the Ag^0Z mordenite

Description	Variable	Value	Units
Pellet Radius	a_p	0.8	mm
Macro-pore Radius	r_p	26.5	nm
Adsorbent Density	ρ_s	3.06	g/cm^3
Macro-porosity	ε_p	0.384	-

2.4.2 Description of experimental systems and procedure

Both the H_2O and I_2 uptake experiments were performed with continuous-flow gas adsorption systems, which have been reported previously (Lin et al., 2014; Nan et al., 2015; Nan et al., 2016). Each of the systems had a H_2O/I_2 vapor generating unit, a microbalance unit, a heating unit, and a data acquisition system. Changing the temperature of the generating units and varying the flow rates of the carrier and dilution gas streams controlled the H_2O and I_2 vapor concentrations. A microbalance connected with a data acquisition system was used in each system for recording the mass changes of the adsorbents during the adsorption/desorption processes.

H_2O adsorption experiments were performed at temperatures between 25 to 80 ^oC, with H_2O concentrations (in terms of dew point) ranged from -69 to 17 ^oC, and I_2 adsorption experiments were conducted at 100 – 200 ^oC with I_2 vapor concentrations in the range of 9 – 52 ppmv. In each experiment, a few vacuum-dried adsorbent particles were loaded into a screen tray suspended from the microbalance. There were fairly large spaces between the particles so the adsorption data essentially represented the adsorption processes on each single particle. Details

of the procedures were reported in previous papers (Lin et al., 2014; Nan et al., 2015; Nan et al., 2016).

2.5 Modeling Results

2.5.1 Kinetics of H_2O on MS3A: Optimization and Prediction

The adsorption of water vapor on commercial MS3A zeolite adsorbents has a potential use for the capture of tritiated water (H^3HO) from the off-gas stream of nuclear fuel reprocessing facilities (Lin et al., 2014; Lin et al., 2015; Ladshaw et al., 2016). A prior study of the kinetics of water vapor on MS3A had utilized various simple kinetic models, such as linear driving force and shrinking core models (Lin et al., 2014). Using the data from that study, a model analysis was performed using the bi-porous pellet kinetics model described in the section **Models for Specific Systems**. The commercial MS3A zeolite used is the perfect structural candidate to validate the bi-porous pellet model. MS3A is a small, spherical adsorbent constructed from a macro-porous binder material that holds small zeolite crystals together, much like it was depicted in Figure 3. Important structural parameters for this pellet were given in Table 1.

For the purpose of modeling the adsorption of water vapor in this system, the relationships discussed from Equations 25 through 37 were used to approximate film mass transfer coefficients (k_f) and pore diffusivities (D_p) from the experimental conditions described by Lin et al. (2014). The value of the micro-pore diffusion coefficient (D_c), however, is not known for this system. Therefore, it was decided to first treat this parameter as adjustable and determine its optimal value for each experiment. The results of that analysis are shown in Figure 4.

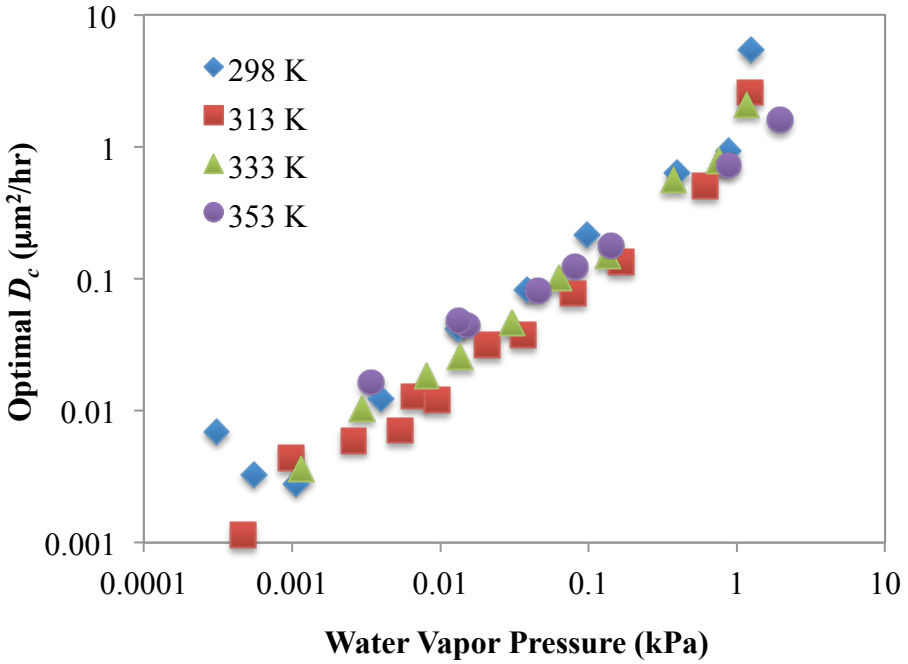

Figure 4: Plot of optimal micro-pore diffusivities versus water vapor pressures across different temperatures. Little or no relationship between diffusivity and temperature is observed, but there is a strong, linear relationship between vapor pressure and diffusivity on a log-log scale. The data analyzed to obtain these values came from Lin et al. (2014).

It is fairly clear to see from Figure 4 that there exists a strong relationship between the micro-pore diffusivity and the ambient vapor pressure. Similar trends were also observed by Lin et al. (2014) for the parameters of the kinetic models they had utilized. Comparisons between the optimized bi-porous model and select kinetic curves from the water adsorption experiments are shown in Figure 5. These curves were normalized by their respective equilibrium capacities at the given experimental conditions. This was done so that no bias would be introduced in the optimization by differences that may exist between the model equilibrium value and the equilibrium value reported by Lin et al. (2014). Overall, the bi-porous kinetic model works very well at describing the adsorption rate for water vapor on the MS3A adsorbent.

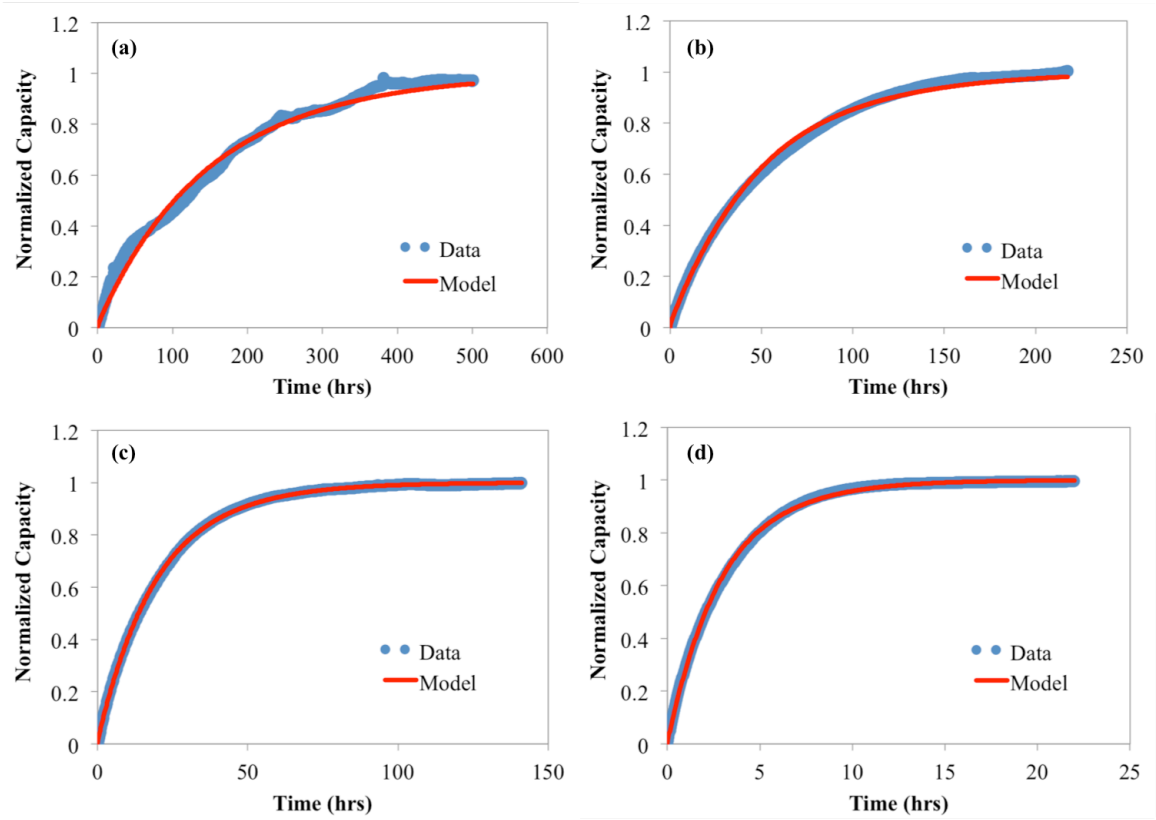

Figure 5: Comparison between data and optimized bi-porous pellet kinetic model for four different uptake curves. The uptake curves were normalized to provide the amount adsorbed divided by the equilibrium adsorption value for each experiment. (a) gas temperature of 25 ^{o}C and vapor pressure of 3.1E-4 kPa, (b) gas temperature of 40 ^{o}C and vapor pressure of 5.4E-3 kPa, (c) gas temperature of 60 ^{o}C and vapor pressure of 8.1E-3 kPa, and (d) gas temperature of 80 ^{o}C and vapor pressure of 8.1E-2 kPa.

It is easy to see that the model performs well when modeling results are fit to the experimental data to determine the optimal micro-pore diffusivity (D_c). However, the mark of a good model will be its ability to predict behavior and not just fit existing data. After the optimal values of the diffusivities have been determined (Figure 4), that information can be utilized to predict different adsorption curves for the same system at different temperatures and pressures.

To accomplish this, adsorption and desorption cycling data were analyzed to further validate the bi-porous model.

The adsorption was performed at the dew point of -10 ^{o}C followed by desorption in dry air (dew point: -70 ^{o}C) after the MS3A particles were equilibrated with H_2O vapor. Adsorption was restarted when desorption reached equilibrium and that process continued for roughly two and a half cycles (Ladshaw et al., 2016). The simulation of the cycling behavior compared to the adsorption/desorption data is shown in Figure 6. This result demonstrates the model's ability to predict the adsorption and desorption cycling behavior of water vapor on the MS3A adsorbent.

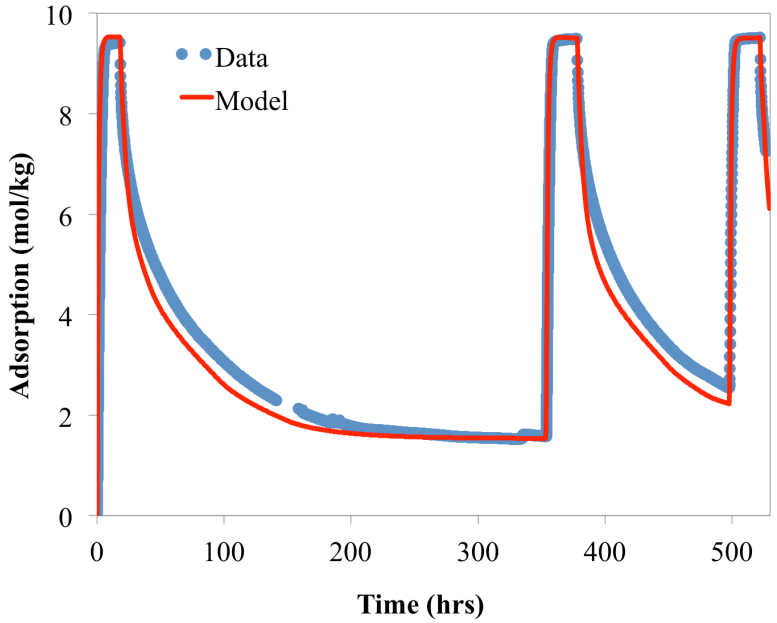

Figure 6: Comparison between adsorption cycling data and bi-porous pellet model predictions. Adsorption occurs at 40 ^{o}C and a vapor pressure of 0.34 kPa. During desorption, the temperature remains the same, but the vapor pressure drops to 7.3E-4 kPa. The data were taken from Ladshaw et al. (2016).

2.5.2 Kinetics of I_2 on Ag^0Z: Model Predictions

To highlight the flexibility and generality of this modeling approach, it will be demonstrated that the bi-porous kinetics model is suitable for predicting adsorption uptake for a completely different system. Here, the bi-porous pellet kinetics model described above has been utilized to predict the uptake rates of I_2 on Ag^0Z pellets, using data reported in a previous paper (Nan et al., 2016). However, the structural treatment of the problem is very different and some of the parameters of the model must be adjusted, as described below, to align with the physical problem.

As was mentioned in **Kinetic Adsorption Data Acquisition**, the Ag^0Z pellets are cylindrical instead of spherical. This is not an issue for the modeling framework that was developed here. Recall that the framework is based on the generalization of a one-dimensional

conservation law (Equation 3). Because of this framework approach, one can easily shift the model into different coordinate systems. This is done so by only changing the value of a single framework parameter (*d*) from a value of 2 to a value of 1.

Also recall that the reducing process involved with preparing the Ag^0Z pellets creates nanoparticles of silver on the outer surface of the adsorbent crystals inside the pellets (Nan et al., 2016). Since the I_2 adsorption occurs only at these silver sites, and those sites are formed on the outside of the micro-porous crystals, the pellet actually behaves more homogeneously. In other words, I_2 travels only through the binder of the pellets, then adsorbs onto the crystals without entering the micro-porous regions.

This can be represented mathematically in the bi-porous pellet model (Equations 16 through 20) by neglecting the micro-porous diffusion equations and replacing them with just the adsorption isotherm. Therefore, the assumption being made is that the I_2 molecules travel through the pore space of the binder, reach a silver site, and then undergo local equilibria reactions to adsorb to that site. In addition, the binder fraction (α) parameter is neglected by setting its value to 1. This will make it so that Equation 19 is exactly representative of homogenous diffusion kinetics for the case of the pore-diffusion controlled adsorption (Tien, 1994).

Since the micro-porous diffusion mechanism is neglected, there is no need for the model of this system to be calibrated with the adsorption data. All system parameters can be approximated based on the relationships in Equations 25 through 37, thereby making the model purely predictive. Then, the last pieces of information necessary to make predictions of the adsorption of I_2 by Ag^0Z pellets are the structural parameters, which were provided in Table 2.

Using the structural parameters from Table 2, as well as the diffusion and film mass transfer parameters calculated from Equations 25 through 37, based on the experimental conditions described above (Nan et al., 2016), simulations were performed to predict the I_2 adsorption kinetics and compare the modeling results to the experimental data. Figure 7 below shows select results of that analysis at different gas temperatures and partial pressures of I_2 in the gas stream. These results show that the model did very well to predict the rate of I_2 adsorption, especially since no parameter optimization was performed. However, it does appear that some of the model uptake curves predicted faster adsorption kinetics than the kinetics observed in the data.

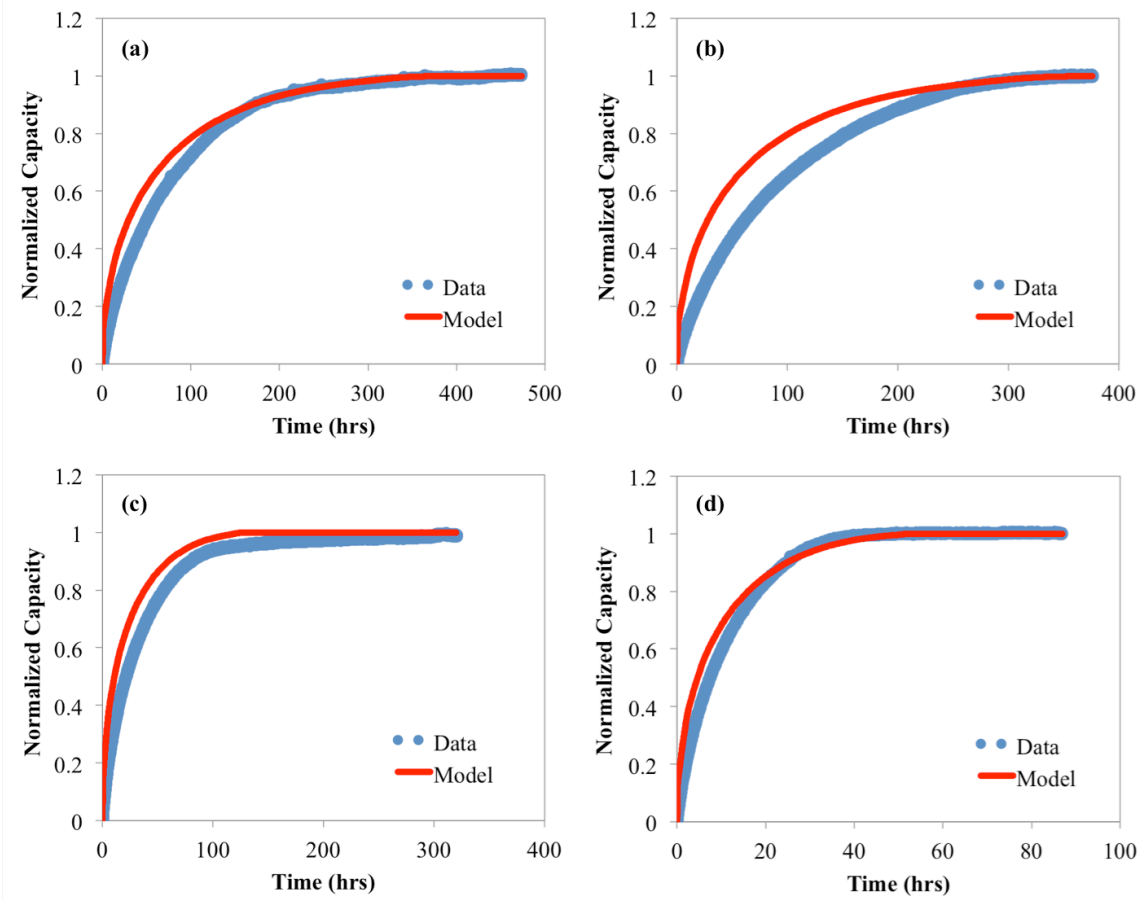

Figure 7: Comparison between data and kinetic model predictions for four different uptake curves. The uptake curves were normalized to represent the amount adsorbed divided by the equilibrium adsorption value for each experiment: (a) gas temperature of 100 ^{o}C and I_2 partial pressure of 1.3E-3 kPa, (b) gas temperature of 150 ^{o}C and I_2 partial pressure of 1.4E-3 kPa, (c) gas temperature of 150 ^{o}C and I_2 partial pressure of 3.7E-3 kPa, and (d) gas temperature of 200 ^{o}C and vapor pressure of 8.8E-3 kPa. The data shown were collected by Nan et al. (2016).

2.5.3 Fixed-bed Column Modeling

Ultimately, the goal of adsorption process modeling is to utilize models in order to design adsorption capture systems. As was previously stated, the most common configuration for removal and recovery of dilute species in gaseous streams is that of a fixed-bed adsorption column (Simo et al., 2009; Gorbach et al., 2004). To demonstrate the framework's capacity to model adsorption in fixed-beds, a fictitious scenario was devised in which the concentration and temperature breakthrough curves for water vapor adsorption in a column packed with MS3A adsorbent pellets could be modeled using this modeling framework.

Structural parameters for the MS3A adsorbent are the same as those in Table 1, and the same isotherm and parameters were used that were discussed in the analysis of the Lin et al. (2014) data set (Figures 5 and 6). The adsorption term (q) for the mass and energy balances of the fixed-bed model (Equations 21 and 23) was resolved by performing simulations with the bi-porous pellet model (Equations 16 through 20) to approximate the amount of water vapor

adsorbed at different points in the column vs time. That result was then coupled into the fixed-bed equations as a mass or energy source/sink term. The heat of adsorption (Q_{st}) was determined through the isotherm relationships described by Ladshaw et al. (2015a) and Llano-Restrepo and Mosquera (2009).

Besides the isotherm parameters and physical characteristics relevant to the MS3A adsorbent, other structural and thermal parameters needed for the fixed-bed model were determined by looking up known values or estimating some constants to take the place of otherwise unknown parameters, such as the wall heat transfer coefficient (U_w) and axial thermal conductivity (K_z). Table 3 summarizes the remaining parameters for the fixed-bed model (Equations 21 through 24) and their corresponding values that were used in the model demonstration. Additionally, for the purpose of this demonstration it was assumed that the temperature of the wall (T_w) was constant and equal to the ambient temperature.

Table 4: Parameters for the Fixed-bed Adsorption Model Demonstration

Description	Variable	Value	Units
Bulk Bed Porosity	ε_b	0.36	-
Linear Gas Velocity	v	0.10	cm/s
Bulk Pellet Density	ρ_b	1.08	g/cm^3
Inlet Concentration	C_{in}	7.80E-5	mol/L
Gas Heat Capacity	h_g	1.01	J/g/K
Gas Density	ρ	1.23E-3	g/cm^3
Pellet Heat Capacity	ρ_s	1.05	J/g/K
Axial Conductivity	K_z	0.01	J/s/cm/K
Heat Transfer Coefficient	U_w	5.00E-3	J/s/cm^2/K
Column Inner Diameter	d_{in}	1.75	cm
Wall Temperature	T_w	313.15	K
Inlet Temperature	T_{in}	313.15	K

For the fixed-bed model demonstration, a 20-hour simulation was run for water vapor adsorption in 9-cm long column given an inlet water vapor pressure of 0.203 kPa and inlet temperature of 313.15 K. Initial conditions for this simulation assumed there was no water vapor in the column prior to the simulation. After the first 10 hours, the inlet boundary conditions for the mass balance were changed to that of dry air such that the final 10 hours of the simulation would represent desorption.

The results of this simulation are summarized in Figures 8 and 9. Figure 8 shows the vapor pressure at the exit of the column over time. It is worth noting here that, in the absence of adsorption, the breakthrough should happen in about 90 seconds given the length of the column and the linear velocity of the gas. Therefore, the model demonstrates significant retardation of the flow, as mass is transferred from the gas phase to the surface sites of the adsorbent. Figure 9 shows the effect that adsorption has on the temperature of the gas stream. The model shows that the gas stream heats up above ambient levels as adsorption occurs, but decreases below ambient during desorption.

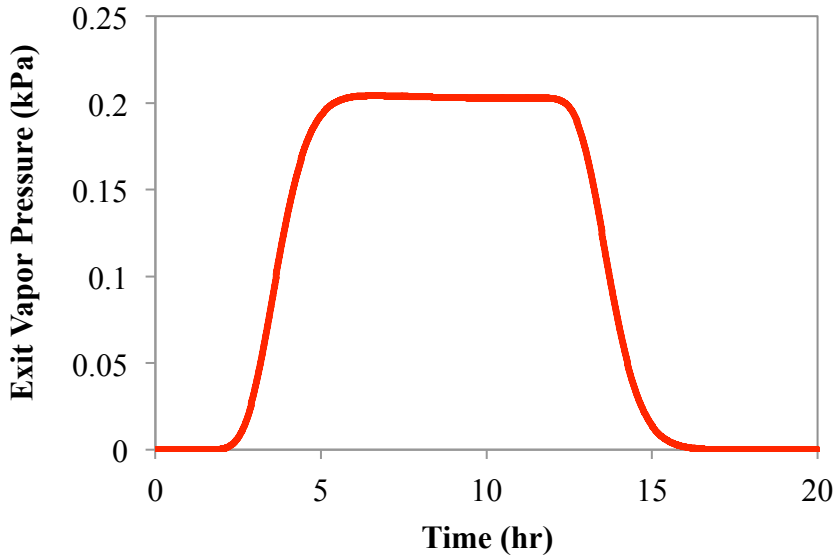

Figure 8: Water vapor breakthrough history for the 20-hour sample simulation in a 9-cm long column packed with MS3A adsorbent. After 10 hours, dry air was given to the model as the inlet boundary condition to simulate desorption of water vapor from 10 to 20 hours.

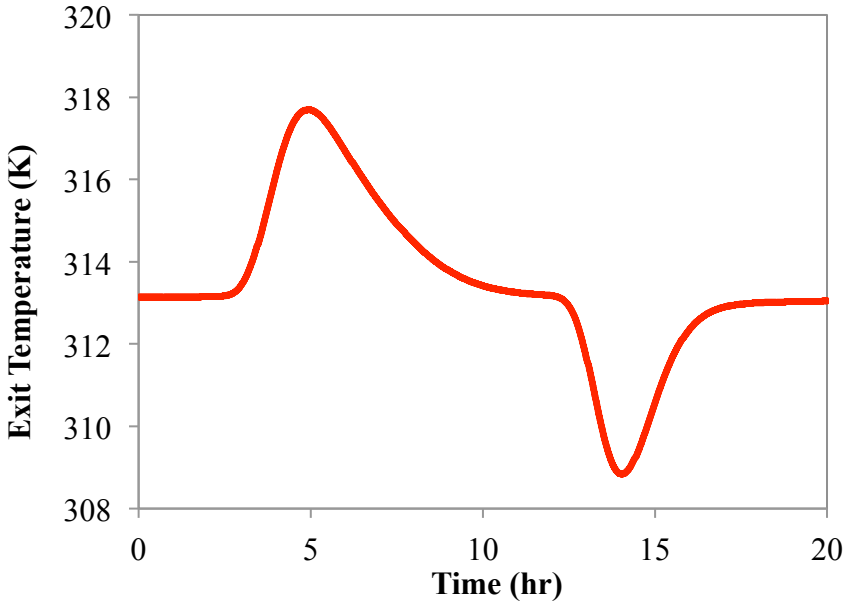

Figure 9: Gas temperature breakthrough history for the 20-hour simulation in a 9-cm long column packed with MS3A adsorbent. After 10 hours, dry air was given to the model as the inlet boundary condition to simulate desorption of water vapor from 10 to 20 hours.

2.6 Discussion

2.6.1 Kinetics of H_2O on MS3A

It is clear to see from Figure 5 that the bi-porous pellet model describes well the adsorption kinetics of water vapor by the MS3A adsorbent. The simpler models investigated by Lin et al. (2014), however, could also fit their data equally well. This comparison immediately brings up the question: Why use the more complex model, when the simpler models are just as good? The primary reason for the use of a complex model is that it will more accurately predict the cycling or desorption behavior of the system.

Let's consider the linear driving force (LDF) model (Equation 39) as a point of comparison against the bi-porous pellet model. This is a very common, very simple model for adsorption kinetics that relates the average equilibrium adsorption value (q_e) of an adsorbent pellet to a lumped mass transfer parameter (k) often referred to as the LDF parameter (Tien, 1994; Simo et al. 2009; Lin et al. 2014). One can find the optimum values for the LDF parameter in a similar manner in which the optimum diffusivity parameters are found from Figure 4. Then, using those parameters, one can model the adsorption/desorption scenario as in Figure 6 and compare those LDF results to both the data and the bi-porous model.

$$\frac{dq}{dt} = k_{LDF}(q_e - q) \tag{39}$$

Recall from the data analysis in Figure 4 that there was a strong relationship between vapor pressure and the micro-pore diffusivity. This was also true for the optimized LDF parameters reported by Lin et al. (2014). To compare LDF to the bi-porous model, LDF simulations considering two different scenarios were performed: (i) one in which there is a step change in the LDF parameter caused by the step change in the vapor pressure and (ii) one in which any change in the LDF parameter caused by changes in vapor pressure has been ignored. Comparison between the LDF model and the bi-porous model at predicting the cycling behavior of water vapor adsorbed by MS3A is shown in Figure 10.

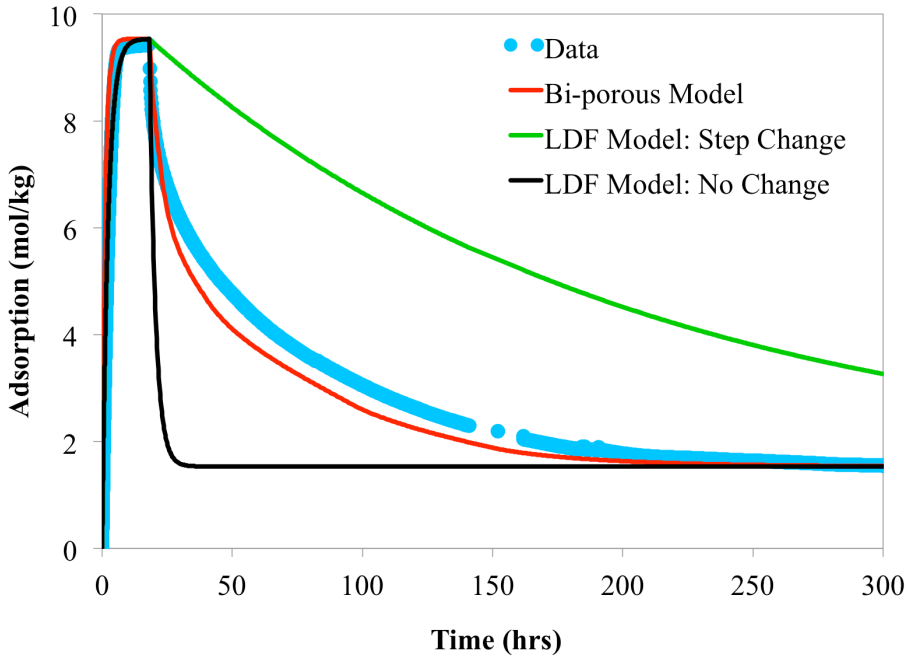

Figure 10: Comparison between the adsorption/desorption cycle behavior for water vapor on MS3A and three different models: (i) the bi-porous pellet model described in this work, (ii) the LDF model with a step change in the LDF parameter, and (iii) the LDF model with no change in the LDF parameter. The bi-porous model works well to predict the adsorption and desorption behavior, while the LDF models can only predict the adsorption curve. The data are taken from Figure 6.

When a step change in the LDF parameter was considered based on the simulation step change from high to low vapor pressure, the LDF model showed slower desorption than adsorption, but it does not accurately reflect the data (Figure 10). In contrast, if one ignores a step change in the LDF parameter, then the rate of desorption is roughly the same as the rate of adsorption. Like the LDF model with the step change, the bi-porous model does consider how changes in vapor pressure change the micro-pore diffusion parameter according to the data analysis of Figure 4. This raises the question: why does the bi-porous model perform better than the LDF model?

The reason the bi-porous model performs better than the LDF models for desorption is because of how the simulations are actually carried out and what information is being tracked throughout the simulation. In the case of the LDF model, the adsorption amount is only calculated as an average, based solely on the driving equilibrium value (q_e) and the rate constant (k). On the other hand, the bi-porous model tracks both the macro-pore gaseous concentration (c) and the micro-pore adsorption (q) as a function of time and space through the entire pellet. In this case, while the outside vapor pressure (C_b from Equation 20) undergoes a step change in the concentration level, the interior concentration of vapor in the macro-pore region of the pellet (c) starts relatively high at the time of the step change, and then decreases gradually as vapor exits the macro-pore space and leaves the pellet.

Recall that, in the bi-porous model (Equation 17), the local adsorption (q) on the crystals is based on that interior concentration (c) and not the exterior concentration (C_b). This is not the case for the LDF model because it does not track the local interior concentrations; instead it bases the average adsorption only on the exterior concentration. Therefore, by tracking how the local interior concentration varies based on the macro-pore diffusion and losses/gains to adsorption/desorption, it is possible to more accurately portray how the overall adsorption process affects the amount of material adsorbing/desorbing as changes occur in the bulk gas phase.

2.6.2 Kinetics of I_2 on Ag^0Z

The model predictions for I_2 on Ag^0Z showed exceptional accuracy for the rates of adsorption at different concentrations and temperatures, but also showed some over-estimates for how fast the system reached equilibrium (Figure 7-b and 7-c). Recall for these simulations that it was assumed once I_2 had reached a silver site, it underwent adsorption instantaneously, thereby reaching its local equilibrium value within the pellet at a given location. However, it was noted by Nan et al. (2016) that the reaction between the iodine and silver was one of the rate controlling mechanisms in the overall adsorption rate. This may explain why the model developed here showed faster adsorption kinetics, especially for Figure 7-b and 7-c.

If the rate of reaction were included, then the local adsorption of I_2, based on the interior concentration of iodine gas, would be smaller compared to the predicted concentration after assuming local equilibrium. This reduction in adsorption locally would suppress the overall rate of adsorption and could yield even better predictions for this system. Therefore, this model can be improved by including adsorption reaction rates at the silver sites instead of just applying the isotherm.

2.6.3 Fixed-bed Column Modeling

The fixed-bed modeling results in Figures 8 and 9 were produced with a fictitious adsorption scenario. This simulation was performed as a demonstration of the modeling capacity of the numerical framework developed in this work. Qualitatively, the model behaves exactly as expected for a simulation of this type. The rate at which the vapor exits the column (Figure 8) indicates that there is a strong retardation effect of adsorption, as water vapor is taken out of the bulk gas phase and adsorbed on the pellets. This is known simply by observing that, in the absence of adsorption and mass-transfer, the breakthrough time for this simulation would be approximately 90 seconds. This value is determined based on the length of the column (9 cm) and the linear velocity of the gas phase (0.1 cm/s).

Additionally, the simulated temperature breakthrough curve in Figure 9 also behaves in a manner expected for adsorption. Since adsorption of water vapor on MS3A is an exothermic process, the gas temperature in the column is expected to rise as adsorption occurs and fall as desorption occurs (Simo et al., 2009). The fixed-bed model demonstration shows this expected behavior (Figure 9).

2.7 Conclusions

While adsorption is a very complex process that can vary widely based on differences in adsorbents and adsorbates, the basic mechanisms that govern this physical-chemical process are generally the same. Regardless of the specifics of the problem, adsorption will always involve (i) interparticle transport, (ii) interphase mass-transfer, (iii) intraparticle diffusion, and (iv) surface reactions and equilibria. Therefore, the most effective and efficient way to model adsorption processes is to create a framework under which one can simulate all these mechanisms.

The basis of that framework comes from the fact that all adsorption models stem from conservation laws. Using that knowledge, a generalized conservation law model (Equation 3) was developed that serves as the basis of a framework to simulate a variety of different adsorption problems. Following this framework, the model problem is solved numerically to preserve its generality, as the numerical solution is valid regardless of whether or not the model is linear or non-linear and/or dominated by advection or diffusion.

As a demonstration of the generality and flexibility of this modeling framework, three different types of common adsorption problems were simulated: (i) spherical, heterogeneous adsorption kinetics, (ii) cylindrical, homogeneous adsorption kinetics, and (iii) one-dimensional, fixed-bed mass and energy transfer. Although these three systems are very different in terms of their structural characteristics, they are all governed by the same mechanisms and conservation laws. Therefore, they can all be modeled under the same framework approach.

Through comparisons of the modeling results produced in this work to experimental data, the validity of this modeling approach and numerical framework has been demonstrated (Figures 5 through 7). This framework gives engineers and scientists a tool by which one can approach a variety of different adsorption problems. Building off from this basic framework, it will be possible to develop a variety of other adsorption models to provide a systematic and mechanistic approach to modeling engineered adsorption processes.

2.8 Acknowledgments

This research was supported by the Nuclear Energy University Program, Office of Nuclear Energy, U.S. Department of Energy. The authors are thankful to Jack Law, Amy Welty, and Kevin Lyon from Idaho National Laboratory, and David DePaoli from Oak Ridge National Laboratory for their insightful comments.

2.9 References

1. C. Tien, *Adsorption Calculations and Modeling*, Butterworth-Heinemann, Newton, MA, 1994.
2. J. Tóth (Ed.), *Adsorption Theory Modeling and Analysis*, Marcel Dekker, Inc. New York, NY, 2002.
3. Simo, M., Sivashanmugam, S. Brown, C.J., and Hlavacek, V., "Adsorption/Desorption of Water and Ethanol on 3A Zeolite in Near Adiabatic Fixed Bed," *Ind. Eng. Chem. Res.*, 48, 9247-9260, 2009.

4. Gorbach, A., Stegmaier, M., Eigenberger, G., "Measurement and Modeling of Water Vapor Adsorption on Zeolite 4A – Equilibria and Kinetics," *Adsorption*, 10, 29-46, 2004.
5. Lin, R., Liu, J., Nan, Y., DePaoli, D.W., Tavlarides, L.L., "Kinetics of Water Vapor Adsorption on Single-Layer Molecular Sieve 3A: Experiments and Modeling," *Ind. Eng. Chem. Res.*, 53, 16015-16024, 2014.
6. Van Leer, B., "Towards the Ultimate Conservative Difference Scheme: A Second-Order Sequel to Godunov's Method," *J. Comp. Physics*, 32, 101-136, 1979.
7. Kurganov, A. and Tadmor, E., "New High-Resolution Central Schemes for Nonlinear Conservation Laws and Convection-Diffusion Equations," *J. Comp. Physics*, 160, 241-282, 2000.
8. Van Albada, G.D., Van Leer, B., Roberts, W.W., "A comparative study of computational methods in cosmic gas dynamics," *Astronomy and Astrophysics*, 108, 76-84, 1982.
9. Knoll, D.A. and Keyes, D.E., "Jacobian-Free Newton-Krylov methods: a survey of approaches and applications," *J. Comp. Physics*, 193, 357-397, 2004.
10. Wilke, C.R., "A Viscosity Equation for Gas Mixtures", *J. Chem. Phys.*, 18, 517-519, 1950.
11. Sutherland, W., "The Viscosity of Gases and Molecular Force", *Philosophical Magazine*, 36, 507-531, 1893.
12. Wakao, N. and Funazkri, T., "Effect of fluid dispersion coefficients on particle-to-fluid mass transfer coefficients in packed beds: Correlation of sherwood numbers", *Chemical Engineering Science*, 33, 1375–1384, 1978.
13. Krieger, F.J., "Calculation of the Viscosity of Gas Mixtures", *U.S. Air Force: Project RAND Research Memorandum*, RM-649, 1951.
14. Llano-Restrepo, M. and Mosquera, M. A., "Accurate correlation, thermochemistry, and structural interpretation of equilibrium adsorption isotherms of water vapor in zeolite 3A by means of a generalized statistical thermodynamic adsorption model". *Fluid Phase Equilibria*, 283, 73-88, 2009.
15. Ladshaw, A., Yiacoumi, S., Tsouris, C., DePaoli, D.W., "Generalized Gas-Solid Adsorption Modeling: Single-Component Equilibria", *Fluid Phase Equilibria*, 388, 169-181, 2015a.
16. Rutledge, V., "OSPREY Model", *U.S. DOE: Separations and Waste Forms*, Idaho National Laboratory, FCRD-SWF-2013-000086, 2013.
17. Lin, R., Ladshaw, A., Nan, Y., Liu, J., Yiacoumi, S., Tsouris, C., DePaoli, D.W., Tavlarides, L.L., "Isotherms for Water Adsorption on Molecular Sieve 3A: Influence of Cation Composition", *Ind. Eng. Chem. Res.*, 54, 10442-10448, 2015.
18. Ladshaw, A., Yiacoumi, S., Tsouris, C., "A generalized procedure for the prediction of multicomponent adsorption equilibria", *AIChE J.*, 61, 8, 2600-2610, 2015b.
19. Ladshaw, A., Nan, Y., Tavlarides, L.L., DePaoli, D.W., Tsouris, C., Yiacoumi, S., "Adsorption Modeling at the Front and Back Ends of the Nuclear Fuel Cycle," *ANS 2016 Annual Meeting*, Conference Proceedings, New Orleans, LA, June 12-15, 2016.
20. Nan, Y., DePaoli, D.W., Tavlarides, L.L., "Adsorption of Iodine on Hydrogen-Reduced Silver-Exchanged Mordenite: Experiments and Modeling," *AIChE J.*, DOI: 10.1002/aic.15432, Accepted July 2016.
21. Nan Y., DePaoli D.W., Tavlarides L.L., "Adsorption of radioactive I_2 and tritiated water from spent fuel reprocessing off-gases by reduced silver mordenite," *Proceedings of 2015 AIChE Annual Meeting*. Salt Lake City, UT. November 8-13, 2015.

22. Chapman K.W., Chupas P.J., Nenoff T.M., "Radioactive iodine capture in silver-containing mordenites through nanoscale silver iodide formation". *Journal of the American Chemical Society*, 132(26), 8897-8899, 2010.
23. Zhao H., Nenoff T.M., Jennings G., Chupas P.J., Chapman K.W., "Determining quantitative kinetics and the structural mechanism for particle growth in porous templates," The Journal of Physical Chemistry Letters.; 2, 2742-2746, 2011.
24. Aspromonte S.G., Mizrahi M.D., Schneeberger F.A., López J.M., Boix A.V., "Study of the nature and location of silver in Ag-exchanged mordenite catalysts. characterization by spectroscopic techniques," *The Journal of Physical Chemistry C*. 117, 25433-42, 2013.

Notation

Roman

a local maximum wave speed, Equ. (5)
a_c micro-sphere nominal radius, Equ. (18)
a_p macro-sphere nominal radius, Equ. (20)
c intrapellet pore space concentration, Equ. (19)
C gas phase concentration in bed, Equ. (21)
C_b bulk gas phase concentration, Equ. (19)
D dispersion coefficient, Equ. (3)
D_c micro-pore diffusion, Equ. (16)
D_{ij} binary diffusivity (cm2/s), Equ. (30)
d_{in} inner diameter of the fixed-bed, Equ. (23)
D_k Knudsen diffusivity (cm2/s), Equ. (26)
D_m molecular diffusivity, Equ. (25)
D_p macro-pore diffusion, Equ. (19)
D_z axial dispersion coefficient, Equ. (21)
$f(c)$ isotherm function, Equ. (17)
$f(u)$ advective flux function, f(u) = zdvu, Equ. (3)
G gradient flux discretization term, Equ. (8)
g gap jump ratio in sub-domain, Equ. (14)
H average advective flux into or out of a cell, Equ. (4)
h_g heat capacity of the gas, Equ. (23)
h_s heat capacity of the solids, Equ. (23)
k reaction coefficient, Equ. (3)
k_f film mass-transfer coefficient, Equ. (20)
k_{LDF} linear driving force coefficient, Equ. (39)
K_z axial thermal conductivity, Equ. (23)
MW molecular weight (g/mol), Equ. (26)
N nodal flux discretization term, Equ. (8)
p penalty term for advective flux, Equ. (5)
P^o reference state pressure (100 kPa), Equ. (37)
P_T total gas pressure (kPa), Equ. (31)
q adsorption or surface concentration, Equ. (16)
q_e equilibrium adsorption, Equ. (39)
Q_{st} heat of adsorption, Equ. (23)
r micro-sphere radial dimension, Equ. (16)

R retardation coefficient, Equ. (3)
R macro-sphere radial dimension, Equ. (19)
R ideal gas constant (J/K/mol), Equ. (31)
Re Reynolds number, Equ. (28)
r_p nominal macro-pore radius (cm), Equ. (26)
S generic source/sink or forcing function, Equ. (3)
Sc Schmidt number, Equ. (28)
t time, Equ. (3)
T gas phase temperature (K), Equ. (23)
T_w temperature of the wall, Equ. (23)
u conserved quantity, Equ. (3)
u_s superfical gas velocity (cm/s), Equ. (33)
U_w heat transfer coefficient of the wall, Equ. (23)
v advective velocity, Equ. (3)
y gas phase molefraction, Equ. (29)
z spatial dimensional quantity, Equ. (3)

Greek

α binder fraction for bi-porous pellet, Equ. (19)
χ temperature correction factor, Equ. (36)
X Sutherland's constant (K), Equ. (32)
Δ change in a quantity
ε_b bulk bed porosity, Equ. (21)
ε_p macro-scale porosity, Equ. (19)
$\phi(g)$ slope limiter function, Equ. (13)
ϑ minmod dispersion parameter, Equ. (12)
μ gas viscosity (g/cm/s), Equ. (30)
μ_g total gas viscosity (g/cm/s), Equ. (35)
ν_g kinematic viscosity (cm2/s), Equ.(33)
ρ gas density (g/cm3), Equ. (23)
ρ_b bulk bed solids density, Equ. (21)
ρ_s pellet density, Equ. (19)
τ tortuosity, Equ. (25)

Sub/Super-scripts

0 inlet boundary node, Equ. (9)
- approach value from the left, Fig. (2)
+ approach value from the right, Fig. (2)
C center node, Equ. (8)
d spatial exponent, Equ. (3)
i,j indices for different species in a mixture
in inlet or input value
l specific node in a domain
L left node, Equ. (8)
o ideal or reference state

R right node, Equ. (8)
z gradient of variable in z-dimension, Equ. (7)

ABSORPTION

3. Carbon Dioxide Absorption

3.1 Key Personnel

Jorge Gabitto (co-PI), Prairie View A&M University

3.2 Scope

Absorption of carbon dioxide is an important process in many practical applications such as carbon capture for the reduction of atmospheric greenhouse gases, chemical processing in the petroleum and chemical industries, and capture of radioactive isotopes in the nuclear fuel cycle. The goal of this part of the project is to develop a dynamic model to simulate CO_2 absorption by using different alkanolamines as absorption solvents. The model is based upon transient mass and energy balances for the chemical species commonly present in CO_2 gas-liquid absorption. A computer code has been written to implement the proposed model, and simulation results are discussed.

3.3 Task and Description of major milestones:

Develop a dynamic absorption model for $^{14}CO_2$ using different solvents.

Year 1 Milestones: (1) Extended literature search; (2) Model development; (3) Computer code development

Year 2 Milestones: (1) Computer code development; (2) Numerical results calculation; (3) Model validation; (4) Final report

3.4 Theoretical Derivation

3.4.1 Introduction

Alkanolamines have become some of the most important chemicals for the removal of acidic components, such as H_2S and CO_2 from gaseous streams. Industrially important amines are: mono-ethanolamine (MEA), di-ethanolamine (DEA), di-isopropanolamine (DIPA), and the tertiary amine N-methyldiethanolamine (MDEA). Most industrial processes are operated with aqueous amine solutions, but solvents consisting of a mixture of water and a nonaqueous solvent, e.g. sulfolane in the Shell-Sulfinol process (Kohl and Riesenfeld, 1979), are also frequently used

(Versteeg and Van Swaaij, 1988). Another alternative is the absorption of CO_2 into aqueous solutions of mixtures of solvents. Blending of different amines is considered to be attractive because, in this way, the high capacity of tertiary amines can be combined with the high absorption rates of primary or secondary amines. Blends are also more flexible than singular amines because the relative concentration of the amines can be varied (Bosch et al., 1989b). Other combinations have been considered such as, MEA and 2-amino-2-methyl-1-propanol (AMP). The latter amine is an attractive alternative since it offers higher absorption capacity and lower regeneration energy. Blending MEA with AMP is considered to combine all favorable characteristics of both amines and overcome the unfavorable characteristics (Sakwattanapong et al., 2009).

Some studies have been carried out considering the influence of the solvent mixed with the alkanolamines. Usubharatana and Tontiwachwuthikul (2009) studied the kinetics of CO_2 capture using methanol mixed into solutions of MEA.

The goal of this work is to develop a general reaction model for a generic blend of amines that can be combined with our recently proposed model for CO_2 absorption in aqueous alkaline solutions (Gabitto and Tsouris, 2014). In this way the proposed model can be used with several different individual alkanolamines as solvents and/or combinations of different solvents.

3.4.2 Kinetic Studies

In the case of primary and secondary amines, the reaction mechanism is well understood and was originally proposed by Caplow (1968) and reintroduced by Danckwerts (1979). CO_2 reacts with the amine through a two steps process. The first step proceeds through the formation of a zwitterion intermediate:

$$RNH_2 + CO_2 \xleftrightarrow{K_1} RHNH^+COO^- \qquad (1)$$

This step is slow and considered to be the rate control step, and is followed by a very fast removal of a proton by a base:

$$RHNH^+COO^- + B \xleftrightarrow{K_b} RHNCOO^- + BH^+ \qquad (2)$$

In this mechanism, the overall forward reaction rate equation can be derived using the assumption of quasi-steady-state for the zwitterion intermediate (Versteeg and. van SwaaiJ, 1988b):

$$r_1 = \frac{k_1[CO_2][RNH_2]}{1 + \frac{k_{-1}}{\sum k_b[B]}} \quad (3)$$

In eq. (3), the summation term represents the reaction of the zwitterion with all the bases present in the solution. For example in dilute aqueous solutions, the amine, OH- ion, and water act as bases, while in non-aqueous solvents, only the amine can be considered a base (Versteeg and. van SwaaiJ, 1988b).

In the case of high amine concentration in the solvent, eq. (3) is simplified to:

$$r_1 = k_1[CO_2][RNH_2] \quad (4)$$

For aqueous MEA solutions the overall reaction rate is second order and is first order with respect to the amine. This finding indicates that the deprotonation of the zwitterion by the bases present in the solution is very fast compared to the reverse reaction. Therefore, Eq. (4) is considered the main reaction in the absorption of CO_2 in high concentration aqueous alkanolamine solutions. In the case of low concentration solutions, more complex rate equations hold (Greer, 2008). Sada et al. (1985) and Alvarez-Fuster et al. (1980) showed that changes in the solvent lead also to changes in the order of reaction.

A different mechanism applies to the reaction of CO_2 with ternary amines. According to Littel et al. (1990), the reaction of CO_2 with tertiary amines can be described satisfactorily using the base-catalysis reaction mechanism proposed by Donaldson and Nguyen (1980):

$$R_1R_2R_3N + CO_2 + H_2O \xleftrightarrow{K_1} R_1R_2R_3NH^+ + HCO_3^- \quad (5)$$

This mechanism is essentially a base-catalyzed hydration of CO_2 and, therefore, tertiary amines cannot react directly with CO_2. This finding was confirmed by Versteeg and Van Swaaij (1988c) who studied the absorption of CO_2 into a solution of MDEA and ethanol without water present.

In all the cases discussed above, the following CO_2 reactions also occur:

$$CO_2 + H_2O \xleftrightarrow{K_2} HCO_3^- + H^+ \quad (6)$$

$$CO_2 + OH^- \xleftrightarrow{K_3} HCO_3^- \quad (7)$$

Reaction (6) is very slow and can be neglected in most circumstances. However, reaction (7) is fast and can enhance mass transfer even when the concentration of hydroxyl ion is low (Bosch et al., 1989).

3.4.2.1 Reaction Scheme

The components in the gas phase are RNH_2, $R_1R_2R_3N$, CO_2, H_2O, N_2, and O_2 while the species considered in the liquid phase are RNH_3^+, $RNCOO^-$, RNH_2, $R_1R_2R_3N$, $R_1R_2R_3NH^+$, CO_2, H_2O, N_2, O_2, HCO_3^-, OH^-, and H_3O^+. The ionic species remain in liquid phase while the others are transferred from one phase to the other according to the scheme shown in Figure 1.

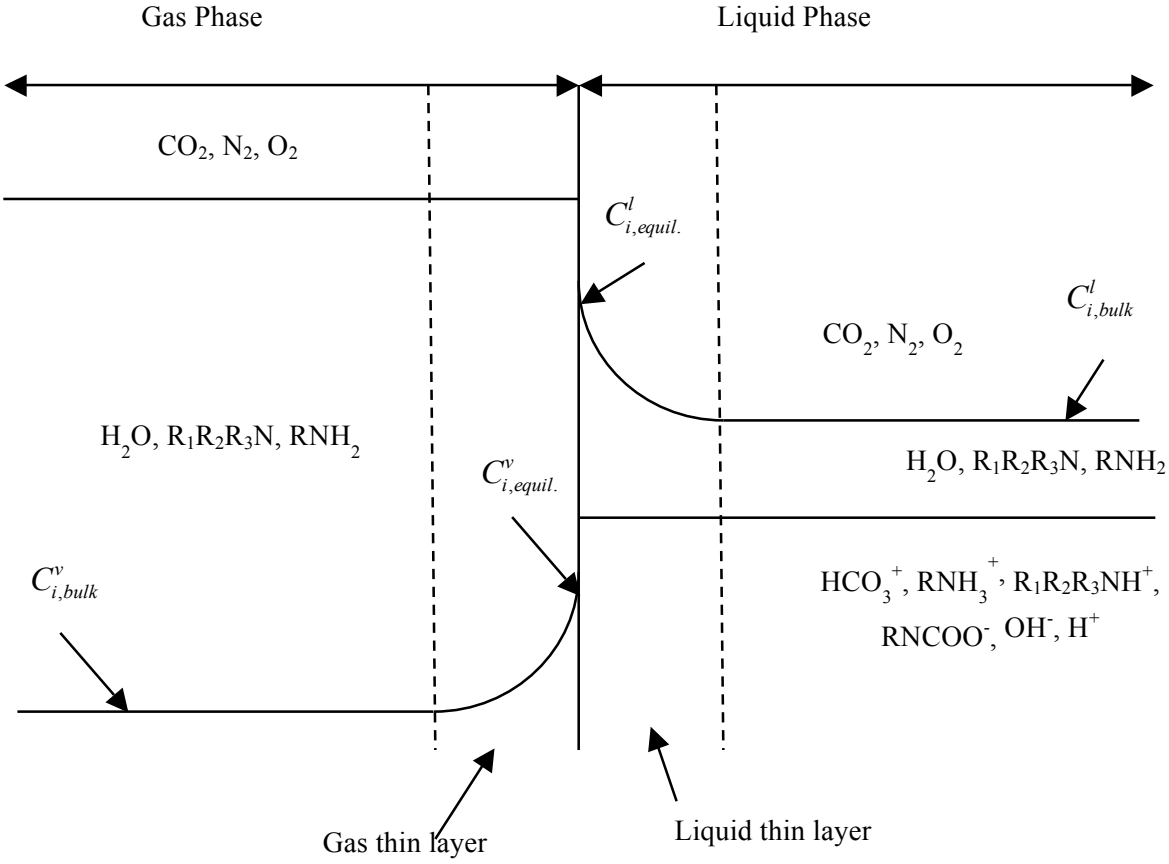

Figure 1. Concentration gradients at the vapor-liquid interphase.

Mandal et al. (1995) and Benamor et al. (2005) proposed the following set of reactions occurring in the aqueous amine solution. One phase equilibrium and six chemical equilibrium equations are introduced to describe the chemistry involved in CO_2 absorption:

$$2\,RNH_2 + CO_2 \xleftrightarrow{K_1} RNHCOO^- + RNH_3^+ \quad (8)$$

$$CO_2 + H_2O \xleftrightarrow{K_2} HCO_3^- + H^+ \quad (9)$$

$$CO_2 + OH^- \xleftrightarrow{K_3} HCO_3^- \quad (10)$$

$$H_2O \xleftrightarrow{K_4} OH^- + H^+ \quad (11)$$

$$RNH_3^+ \xleftrightarrow{K_5} RNH_2 + H^+ \quad (12)$$

$$RNHCOO^- + H_2O \xleftrightarrow{K_6} RNH_2 + HCO_3^- \quad (13)$$

$$CO_2(gas) \leftrightarrow CO_2(liq.) \quad (14)$$

Following Bosch et al. (1989b), who studied blends of alkanolamines, we added reaction (5) catalyzed by ternary amines and reaction (15) to account for the decomposition of the ternary ammonium ion:

$$R_1R_2R_3NH^+ \xleftrightarrow{K_{15}} R_1R_2R_3N + H^+ \quad (15)$$

Reactions (5), (8), and (10) are the main reactions in CO_2 absorption. The other reactions are required to complete the total reaction mechanism (Bosch et al., 1989b). The loading rate of CO_2 to the alkanolamines determines the relative weight of all reactions. For CO_2 loading rates below 0.5, equation (8) is the main reaction. In the case of loading rates above 0.5, reaction (10) dominates, while reaction (5) will be important only for big amounts of ternary amine in the feed. In this work, we are interested on small loading rates and significant amounts of ternary amine present; therefore, absorption into the amines will be the most important reaction. In Table 1, we included all the species calculated in the model. Reaction (14) is given by the corresponding Henry's law constant for CO_2 (H_{cc}).

Table 1. List of compounds participating in the reaction scheme.

Compound No	Gas	Liquid
1	N_2	$RNHCOO^-$
2	O_2 (g)	RNH_3^+
3	CO_2 (g)	HCO_3^-
4	H_2O (g)	OH^-
5	RNH_2 (g)	RNH_2 (l)
6	$R_1R_2R_3N$ (g)	CO_2 (l)
7	----	H^+(l)
8	----	$R_1R_2R_3N$ (l)
9	----	$R_1R_2R_3NH^+$ (l)

We collected kinetic data using a general primary-secondary amine that follows the zwitterion mechanism represented by Caplow (1968) and Danckwerts (1979). The forward reaction (8) is thought to occur through a two-step mechanism. Initially, a CO_2 and an alkanolamine molecule form a zwitterion intermediate, which in a second step reacts with another alkanolamine molecule. The second step is much faster than the first step, hence the first step is rate limiting and second order. The reaction rate is given by:

$$-r_1 = k_{1f}\,[CO_2]\,[RNH_2]\ (\text{mol s}^{-1}\ \text{m}^{-3}) \quad (16)$$

The specific forward rate constant k_{1f} is calculated using (Jamal et al., 2006):

$$k_{1f} = \text{Exp}[24.4 - 6864./T_l]\ (\text{m}^3\ \text{mol}^{-1}\ \text{s}). \quad (17)$$

Bicarbonate formation, reaction (10), is the most important reaction for CO_2/Alkanolamine loadings above 0.5. It is of second order given by:

$$-r_3 = k_{3f}\,[CO_2]\,[OH^-]\ (\text{mol s}^{-1}\ \text{m}^{-3}) \quad (18)$$

The forward rate for the formation of bicarbonate is significantly fast, but the overall rate is usually quite small due to the low concentration of OH^- ions used. At CO_2/alkanolamines loadings above 0.5, this becomes the dominant reaction for CO_2 removal. The forward rate is calculated from (Freguia and Rochelle, 2003):

$$k_{3f} = \text{Exp}[31.396 - 6658.0/T_l]/1000\ (\text{m}^3\ \text{mol}^{-1}\ \text{s}^{-1}) \quad (19)$$

In order to complete the rate calculations, we collected literature data corresponding to the equilibrium rate constants of reactions (8) to (13), from Bedelbayiev et al. (2008) and Greer (2008). In order to deal with reactions (5) and (15) for ternary alkanolamines, we followed many investigators including Haimour et al. (1987), Critchfield (1988), Littel et al. (1990), and Rangwala et al. (1992) who fit the rate constant of the reaction as a function of temperature by:

$$k_I = k_I^o \exp\left[\frac{-E}{R}\left(\frac{1}{T} - \frac{1}{298.15}\right)\right] \quad (20)$$

Table 2 summarizes all the rate equations used in the model:

Table 2. Information used in the solution of the proposed reaction model.

Eqn. No Reaction	Forward Rate (k_{fi})	Equilibrium Constant	Reverse Rate (k_{ri})
5 (7)	$k_{7f} = 2.5E\text{-}3\ Exp(23.17\text{-}6894.8/T_l)$	$K_7 = K_2/K_9$	$K_{7r} = (k_{7f})/K_7$
8 (1)	$k_{1f} = Exp(24.4\text{-}6864/T_l)$	$K_1 = K_2/(K_5*K_6)$	$k_{1r} = (k_{1f})/K_1$
9 (2)	$k_{f2} = 0.024$	$K_2 = 1E6*Exp(231.465\text{-}12092.1/T_l\text{-}36.782*Ln(T_l))$	$k_{2r} = (k_{2f})/K_2$
10 (3)	$k_{3f} = Exp[31.396\text{-}6658./T_l]*1E\text{-}3$	$K_3 = Exp(31.396\text{-}6658/T_l)/1000$	$k_{3r} = (k_{3f})/K_3$
11(4)	$k_{4f} = 2.E\text{-}5$	$K_4 = 9.234E19*Exp(0.0772*T_l)$	$k_{4r} = (k_{4f})/K_4$
12 (5)	$k_{5f} = 0.1$	$K_5 = 1E6*Exp(0.8\text{-}8094.8/T_l\text{-}0.00748*T_l)$	$k_{5r} = (k_{5f})/K_5$
13(6)	$k_{6f} = 0.1$	$K_6 = 2.E5*Exp(1.283\text{-}3456.2/T_l)$	$k_{6r} = (k_{6f})/K_6$
15(8)	$K_{8f} = 0.1$	$K_8 = 1E6*Exp(0.8\text{-}8094.8/T_l\text{-}0.00748*T_l)$	$K_{8r} = (k_{8f})/K_8$

The equations used to calculate the forward and reverse reactions are:

$$-r_{1f} = k_{1f}\,[CO_2]\,[RNH_2] \quad (mol\ s^{-1}\ m^{-3}) \qquad (21)$$

$$-r_{2f} = k_{2f}\,[CO_2]\,x_{H2O} \quad (mol\ s^{-1}\ m^{-3}) \qquad (22)$$

$$-r_{3f} = k_{3f}\,[CO_2]\,[OH^-] \quad (mol\ s^{-1}\ m^{-3}) \qquad (23)$$

$$-r_{4f} = k_{4f} \quad (mol\ s^{-1}\ m^{-3}) \qquad (24)$$

$$-r_{5f} = k_{5f}\,[CO_2]\,[RNH_3^+] \quad (mol\ s^{-1}\ m^{-3}). \qquad (25)$$

$$-r_{6f} = k_{6f}\,[RNHCOO^-] \quad (mol\ s^{-1}\ m^{-3}) \qquad (26)$$

$$-r_{7f} = k_{7f}\,[CO_2]\,[R_1R_2R_3N]\,x_{H2O},\ (mol\ s^{-1}\ m^{-3}) \qquad (27)$$

$$-r_{8f} = k_{8f}\,[R_1R_2R_3NH^+]\ (mol\ s^{-1}\ m^{-3}) \qquad (28)$$

$$-r_{1r} = k_{1r}\,[RNH_3^+]\,[RNHCOO^-]\ (mol\ s^{-1}\ m^{-3}) \qquad (29)$$

$$-r_{2r} = k_{2r}\,[HCO_3^-]\,[H^+] \quad (mol\ s^{-1}\ m^{-3}) \qquad (30)$$

$$-r_{3r} = k_{3r} [HCO_3^-] \quad (\text{mol s}^{-1} \text{ m}^{-3}) \tag{31}$$

$$-r_{4r} = k_{4r} [OH^-] [H^+] \quad (\text{mol s}^{-1} \text{ m}^{-3}) \tag{32}$$

$$-r_{5r} = k_{5r} [H^+] [RNH_2] \quad (\text{mol s}^{-1} \text{ m}^{-3}) \tag{33}$$

$$-r_{6r} = k_{6r} [HCO_3^-] [RNH_2] \quad (\text{mol s}^{-1} \text{ m}^{-3}) \tag{34}$$

$$-r_{7r} = k_{7r} [HCO_3^-] [R_1R_2R_3NH^+] \quad (\text{mol s}^{-1} \text{ m}^{-3}) \tag{35}$$

$$-r_{8r} = k_{8r} [R_1R_2R_3N] [H^+] \quad (\text{mol s}^{-1} \text{ m}^{-3}) \tag{36}$$

Here, x_{H2O} is the water molar fraction in the feed solvent phase.

Assuming pseudo-steady state for every chemical species, we can calculate the generation terms that enter into the chemical species mass balances. In order to simplify the calculations, it is better to determine an overall rate per reaction according to:

$$R_{ai} = r_{if} - r_{ir} \tag{37}$$

Every generation term (R_{gen}) is calculated by a molar balance using:

$$R_{gen1} = R_{a1} - R_{a6} \tag{38}$$

$$R_{gen2} = R_{a1} - R_{a5} \tag{39}$$

$$R_{gen3} = R_{a2} + R_{a3} + R_{a6} \tag{40}$$

$$R_{gen4} = R_{a4} - R_{a3} \tag{41}$$

$$R_{gen5} = R_{a5} + R_{a6} - 2\,R_{a1} \tag{42}$$

$$R_{gen6} = R_{a7} - R_{a4} - R_{a5} \tag{43}$$

$$R_{gen7} = R_{a2} + R_{a4} + R_{a5} \tag{44}$$

$$R_{gen8} = R_{a8} - R_{a7} \tag{45}$$

$$R_{gen9} = R_{a7} - R_{a8} \tag{46}$$

Carbon dioxide absorption is accompanied by strong chemical reactions. Therefore, the calculation of the CO_2 flux term requires the use of an enhancement factor (E) to account for the enhanced mass transfer. The enhancement factor is defined as the mass transfer rate under absorptive reaction divided by the mass transfer rate under non-reactive absorption conditions (Perry and Green, 1999). The CO_2 molar flux term ($\dot{N}_{CO2}$) is given by (Bedelbayiev et al., 2008; Greer et al., 2008; and Greer, 2008):

$$\dot{N}_{CO2} = - k_{l,CO2}\, E\, a_w\, H^{cc}\, C^{g}_{CO2} \tag{47}$$

Here, H^{cc} ($H^{cc} = C_i^l / C_i^g$) is the concentration based Henry's constant. The enhancement factor (E) is given by the Hatta number defined as:

$$Ha = \frac{\sqrt{D_{CO2}\,(k_{1f}\,C_{RNH2} + k_{3f}\,C_{OH^-} + k_{7f}\,C_{R1R2R3N})}}{k_l} \qquad (48)$$

Here, D_{CO2} is the diffusion coefficient and k_l is the liquid-layer mass transfer coefficient. The influence of the reaction on the total rate of CO_2 absorption is considered by the enhancement factor E. The enhancement factor is a function of the Hatta number (Ha). This number is the ratio of the rate of homogeneous reaction relative to the rate of gas dissolution. Ha is also a measure of the amount of dissolved gas that reacts inside the diffusion film near the gas-liquid interface compared to that which reaches the bulk of the solution without reacting. When Ha=0 we have purely physical absorption. The higher the value of the Hatta number, the stronger is the effect of chemical reaction on mass transfer. In the case of Ha > 2, the enhancement factor E is directly equal to the Ha number. In this case all the reaction is confined to a small liquid film on the liquid side of the interface. The reaction model is given by:

$$A(g) + B(l) \xrightarrow{k_r} \text{Products} \qquad (49)$$

The chemical species B is the active liquid phase solute that reacts with the adsorption species originally in gas phase, CO_2 in our case. This formulation leads to the following general equation for the Hatta number:

$$Ha = \frac{\sqrt{D_A\,k_r\,C_B^l}}{k_A^l} \qquad (50)$$

Versteeg et al. (2006) recommended a different definition of the Ha number including C_{CO2} instead of C_{NaOH} in eq. (48) to calculate the enhancement factor when all RNH_2 is consumed and reaction (3) is the dominant CO_2 removal reaction. Other authors have used *both* formulations with similar results (Bedelbayev et al., 2008; Mores et al., 2010; Gomèz et al., 2003, van Elk et al., 2006, among others). In this work, however, we preferred to use equation eq. (50), which is based upon the general definition of the Ha number.

3.4.2.2 Mass Transfer Model

Mass Balances

The mass balance of component i in the liquid phase was calculated using (Gabitto and Tsouris, 2014):

$$\frac{\partial C_i^l}{\partial t} = u \frac{\partial C_i^l}{\partial z} - \dot{N}_{i,diff} + R_{gen,i} \qquad (51)$$

where the $R_{gen,i}$ term represents moles of species i generated/consumed by interphase reaction per unit volume and $\dot{N}_{i,diff}$ is the mass flux of component i from the gas phase into the liquid phase. In the model presented in this work, the effect of the reaction on CO_2 absorption is considered through the use of the enhancement factor. In the cases of ionic species, there is no interphase mass transfer; therefore, for these reactions, eq. (51) becomes:

$$\frac{\partial C_i^l}{\partial t} = u \frac{\partial C_i^l}{\partial z} + R_{gen,i} \qquad (52)$$

The generic amines (RNH_2 and $R_1R_2R_3N$) were the only chemical species for which we had to calculate a generation term plus an interfacial mass-transfer term ($\dot{N}_{RNH_2,diff}$ and $\dot{N}_{R_1R_2R_3N,diff}$).

Energy Balances

The reactions given by equations (8) and (10) are highly exothermic; therefore, an energy balance has to be solved in order to consider temperature changes. The heat of reactions used for equations (8) and (10) were 65 kJ/mol CO_2 and 20 kJ/molCO_2, respectively. The first value was taken from Greer (2008) and the second from Pinsent et al. (1956).

A two equation model for the transient energy balance in the control volume depicted in Figure 1 leads to the following equations for all the components shown in the figure (Greer, 2008; Greer et al., 2008; Lawal et al., 2009):

$$\frac{\partial T^l}{\partial t} = - u_l \frac{\partial T^l}{\partial z} - \dot{N}_{CO2} \Delta H_R / \sum_i C_i^l C_{pi}^l - U_T a_w \left(T^l - T^v\right) / \sum_i C_i^l C_{pi}^l \qquad (53)$$

$$\frac{\partial T^v}{\partial t} = - u_v \frac{\partial T^v}{\partial z} + U_T a_w \left(T^l - T^v\right) / \sum_i C_i^v C_{pi}^v \qquad (54)$$

Here, C_{pi}^v and C_{pi}^l are the heat capacities of component i in the mixture, U_T is the global heat transfer coefficient, ΔH^{vl} is the latent heat for the change of phase, u_l and u_v, are the convective velocities inside the liquid and vapor phases, and ΔH_R is the heat released by the chemical reaction. The CO_2 molar flux term ($\dot{N}_{CO2}$) is given by eq. (47), while the enhancement factor (E) is given by the Hatta number defined in eq. (48).

Thermodynamics

The mass flux of component i from the gas phase into the liquid phase ($\dot{N}_i^v$) is calculated using:

$$\dot{N}_{i,diff} = k_l a_w \left(C_i^b - C_i^*\right) \quad (55)$$

where k_l is the liquid-side mass-transfer coefficient, a_w is the interphase surface area per unit volume, C_i^b is the liquid bulk concentration, and C_i^* is the interfacial liquid equilibrium concentration. In order to evaluate C_i^*, we used an iterative scheme in the previous version of our model that relied upon a vapor-liquid equilibrium model (Gabitto and Tsouris, 2014). In this work, we used a formulation based upon the calculation of gas and liquid fugacity values (Greer, 2008). This formulation avoids the use of an iterative procedure as the fugacity values can be calculated directly by:

$$\dot{N}_{i,diff} = \frac{k_i^v a_w}{\varphi_i^v Z^v R T^v} (f_i^l - f_i^v) \quad (56)$$

This expression for the diffusion flux is valid for the RNH_2, $R_1R_2R_3N$, and H_2O components when the resistance is assumed to be in the gas liquid film (Greer, 2008). A similar expression for CO_2, O_2, and N_2 can be also be derived by:

$$\dot{N}_{i,diff} = \frac{k_i^l a_w}{\varphi_i^l P} (f_i^v - f_i^l) \quad (57)$$

3.5 Results and Discussion

3.5.1 Simulation Results

A computer code was developed modifying the one prepared for the previous work on CO_2 absorption using high pH alkaline aqueous solutions (Gabitto and Tsouris, 2014). Validation of the computer code was achieved by comparing calculated parameters with experimental data from the literature, especially with the work from Greer (2008). A global mass balance for the amines and their reaction products gives:

$$u_1 A_{sec.} [RNH_2]_{IN} = u_1 A_{sec.} ([RNH_2]_{IOUT} + [RNH_3^+]_{OUT} + [RNHCOO^-]_{OUT}) \quad (58)$$

and $$u_1 A_{sec.} [R_1R_2R_3N]_{IN} = u_1 A_{sec.} ([R_1R_2R_3N]_{IOUT} + [R_1R_2R_3N^+]_{OUT}) \quad (59)$$

The difference between both sides in eqns (58) and (59) is used as a way of estimating the accuracy of the reaction scheme.

The time change of the CO_2 concentration is depicted in Figures 2, 3, and 4. In Figure 2, we show typical axial concentration profiles. The concentration of CO_2 is highest at the base of the column, z = 0, and drops as we approach the top, z = 1. The results in Figure 2 show that, as time increases, the concentration of CO_2 decreases as we approach the top. We can also see that at long times steady-state is achieved. The CO_2 concentration in the gas phase is associated with the

concentration of produced $[HCO_3^-]$ as the bicarbonate ions appear due to the consumption of CO_2 and the stoichiometric ratio is one to one. The corresponding bicarbonate ion profile is shown in Figure 3.

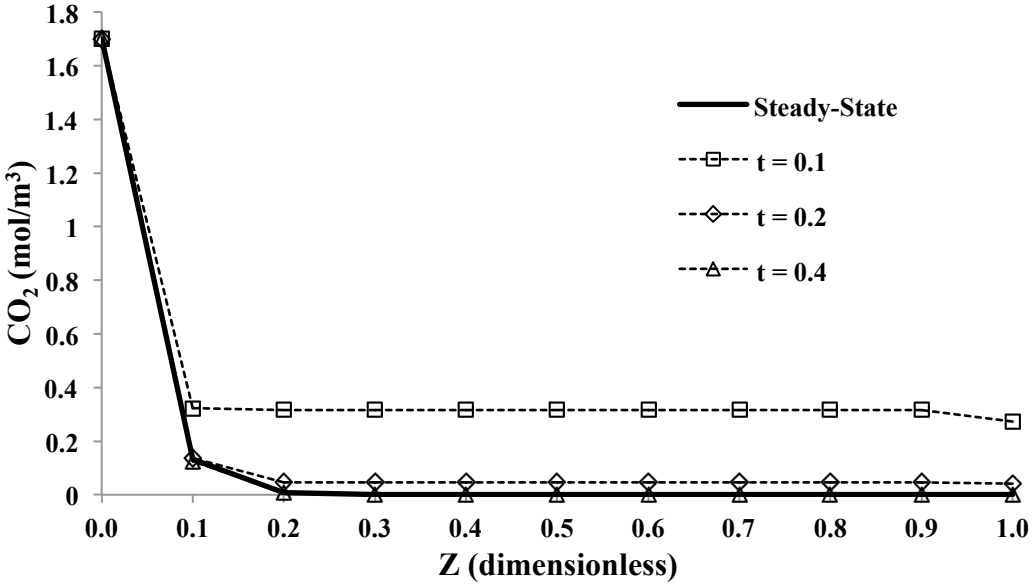

Figure 2. Carbon dioxide axial concentration profile.

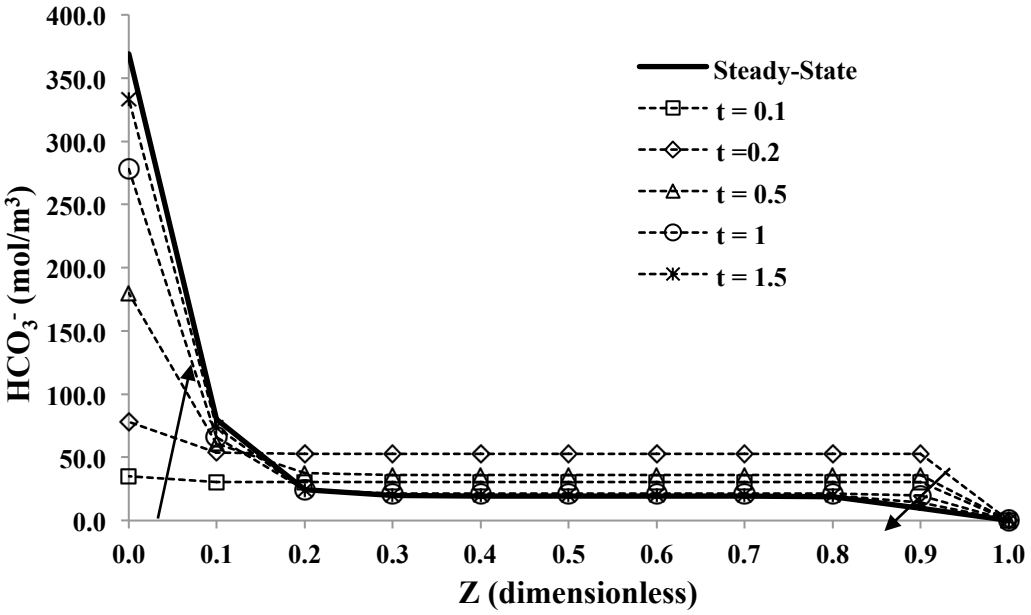

Figure 3. Bicarbonate ion concentration profile.

Figure 3 shows that the time evolution of the carbonate profile in the liquid phase is more complex than the corresponding CO_2 profile in the gas phase. Initially, the values of the ion concentration are higher than the steady-state values at the top of the column while the reverse is true at the bottom of the column. As times increases, the concentration of carbonate ion

decreases in the top region, while the concentration in the bottom region increases until converging to the steady-state solution. The results shown in Figure 3 suggest intense axial mass transport for the carbonate ions. Similar results were reported by Gabitto and Tsouris (2014).

The time evolution of the CO_2 concentration profile is shown in Figure 4. The depth axis depicts the axial variation of the concentration from the top to the bottom, i.e., it is a view from the top. The horizontal axis shows the time change of the concentration profile. Low values are represented by blue colors, while high values are represented by red colors. The 'back' wall represents CO_2 input values, while the left-side wall represents initial conditions. The results in Figure 4 show that, for a column height equal to 10 m, the CO_2 concentration decreases very rapidly and then remains constant at the steady-state value. This result is consistent with other calculations, not shown here, which prove that the removal rate decreases as the column height decreases. All these results have been calculated using a relatively tall column (10-m height).

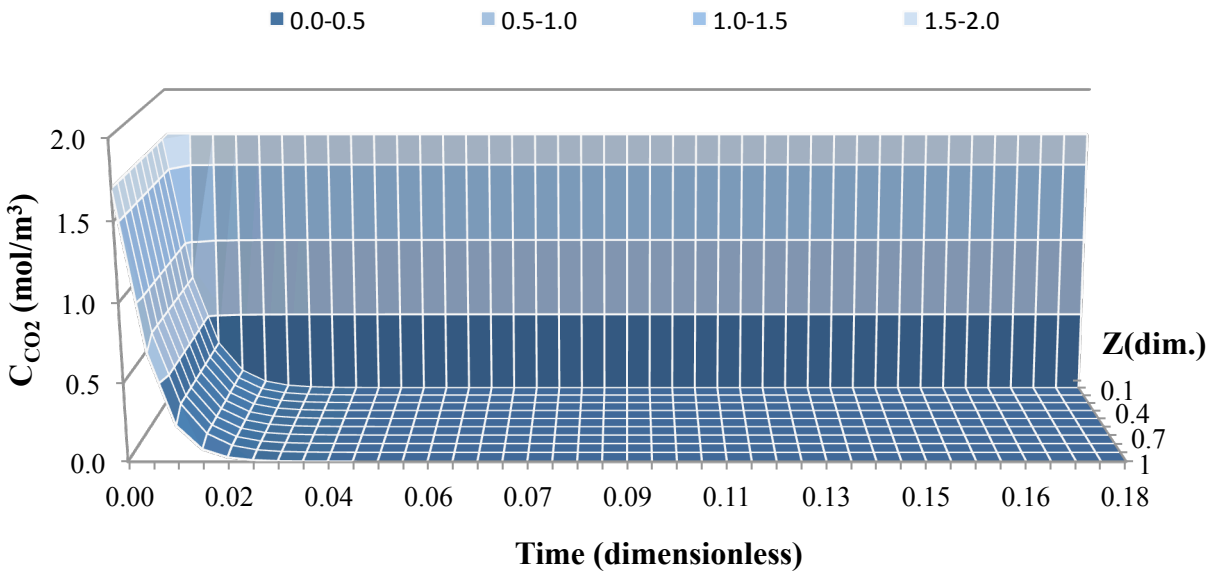

Figure 4. Contour plot depicting the time evolution of the CO_2 axial concentration profile.

In order to study the time evolution of the generic amine we chose to use mono ethanol amine (MEA) due to the high amount of data available for this particular chemical compound. MEA reacts with CO_2, following reaction (8). Two ions, $[RNH_3^+]$ and $[RNHCOO^-]$, are produced by this reaction and consumed by reactions (12) and (13), respectively.

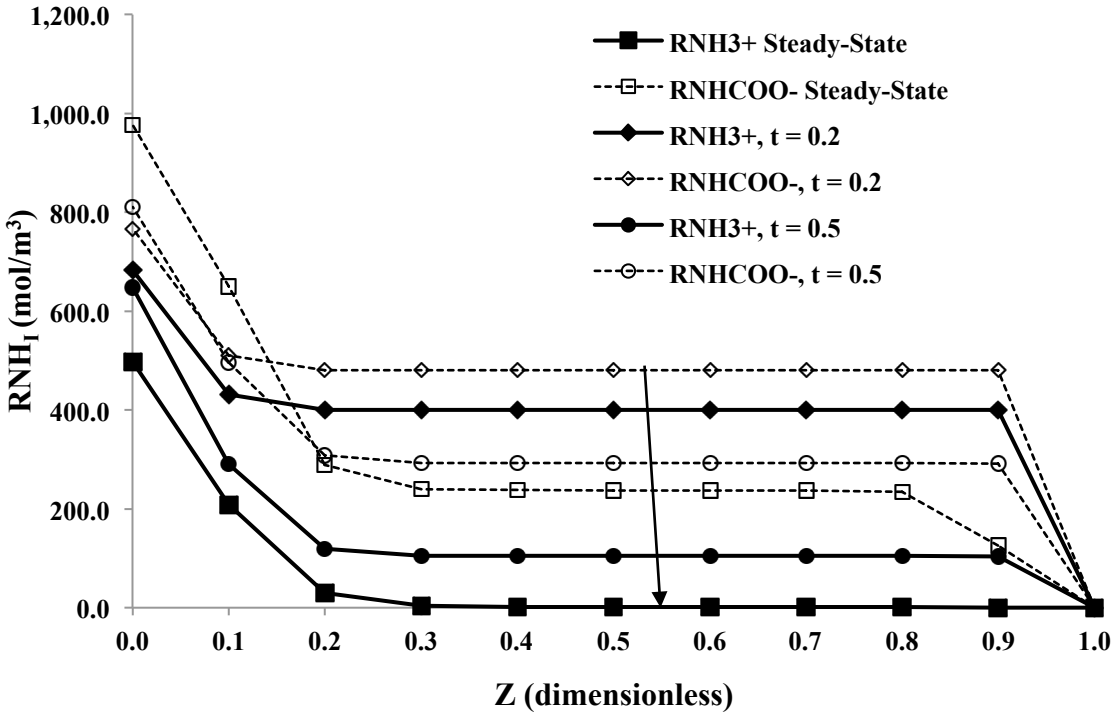

Figure 5. Alkanolamine ion axial concentration profiles.

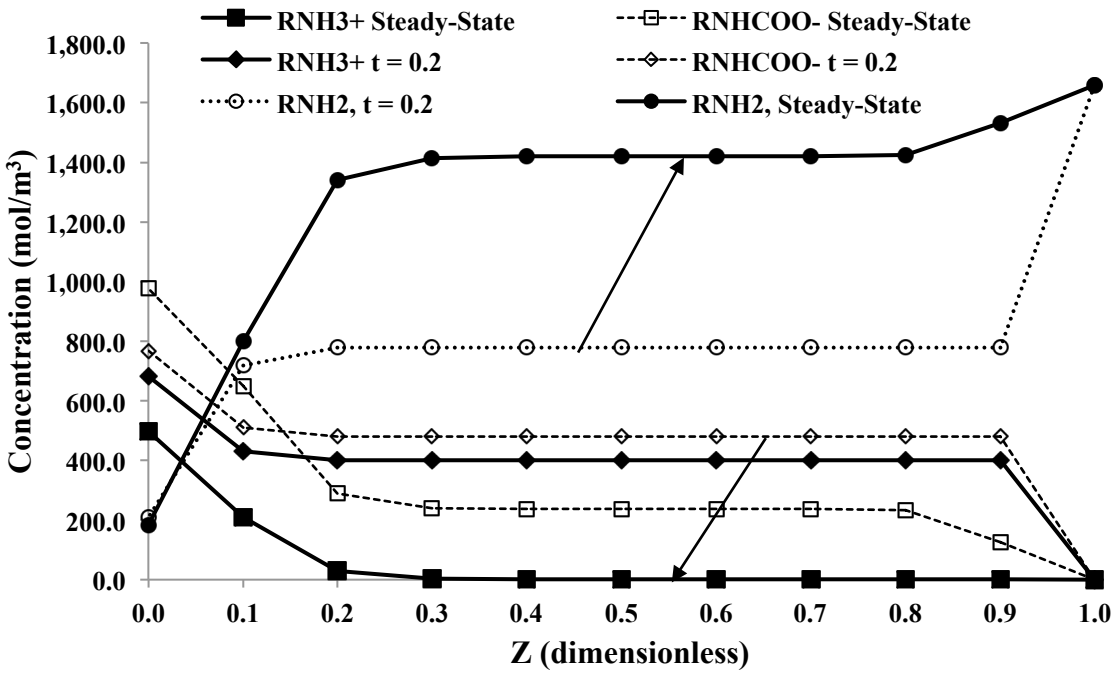

Figure 6. MEA and ions axial concentration profiles.

Figure 5 depicts the time evolution of the ammonium-like ($[RNH_3^+]$) and the carbamate ($[RNHCOO^-]$) ions. Both ions are not present in the input solution at the top (z = 1), their concentration increases as they encounter CO_2 moving upwards in the gas phase, until a

maximum is reached at the bottom coinciding with the highest CO_2 concentration at the bottom of the column (z = 0). Figure 5 also shows that, as time increases, a steady-state solution is approached. However, the different values of the kinetic parameters in reactions (12) and (13) determine a faster approach to steady-state for the ammonium-like ion. The concentration values of the ammonium-like ion were also higher than the carbamate concentration values in all our simulations. In all the simulation results presented in this report, the mass balance condition given by eq. (50) held up to the numerical error of the computer code. The relationship between MEA and its reaction products is depicted in Figure 6. As the amount of the reaction products increases, we can expect that the amount of the free amine will decrease. The equilibrium reactions between the amine and its reaction products are very fast and, therefore, the values of the amine and the ions will approach equilibrium. Calculations, not shown here, corroborate this conclusion.

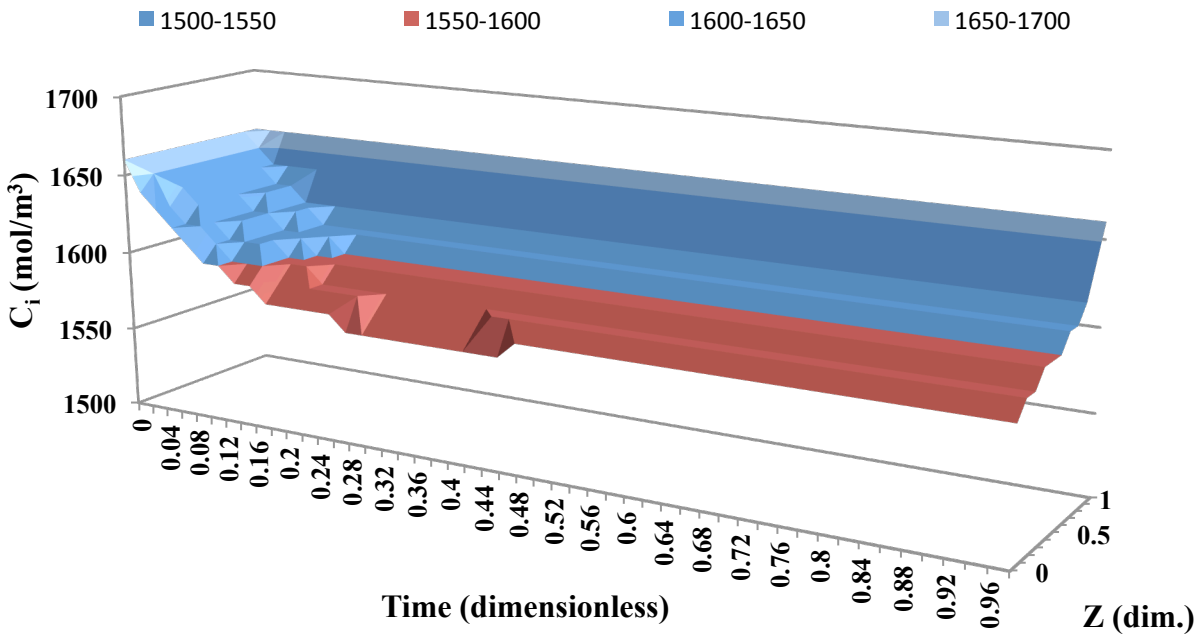

Figure 7. Time evolution of the MEA axial concentration profile.

The time change of the MEA concentration is shown in Figure 7. The figure presents a bottom view of the column. The 'back' wall is the input value at all times. The 'side' wall represents the initial condition assumed to be constant and equal to the input. We can see that there is a sharp decrease in the amount at the bottom of the column due to a region of high reaction rate due to the CO_2 input being located in that zone; then, the amount increases as the CO_2 amount decreases until reaching the input value. The figure also shows that the amine amount increases as time increases.

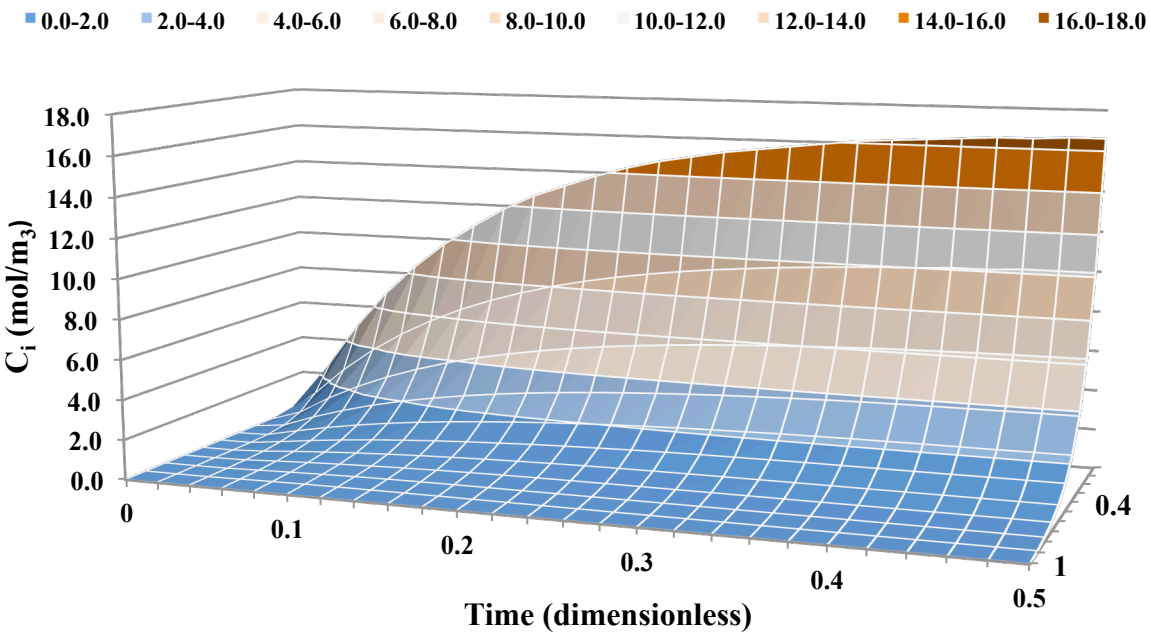

Figure 8. Time evolution of the MEAmide ion axial concentration profile.

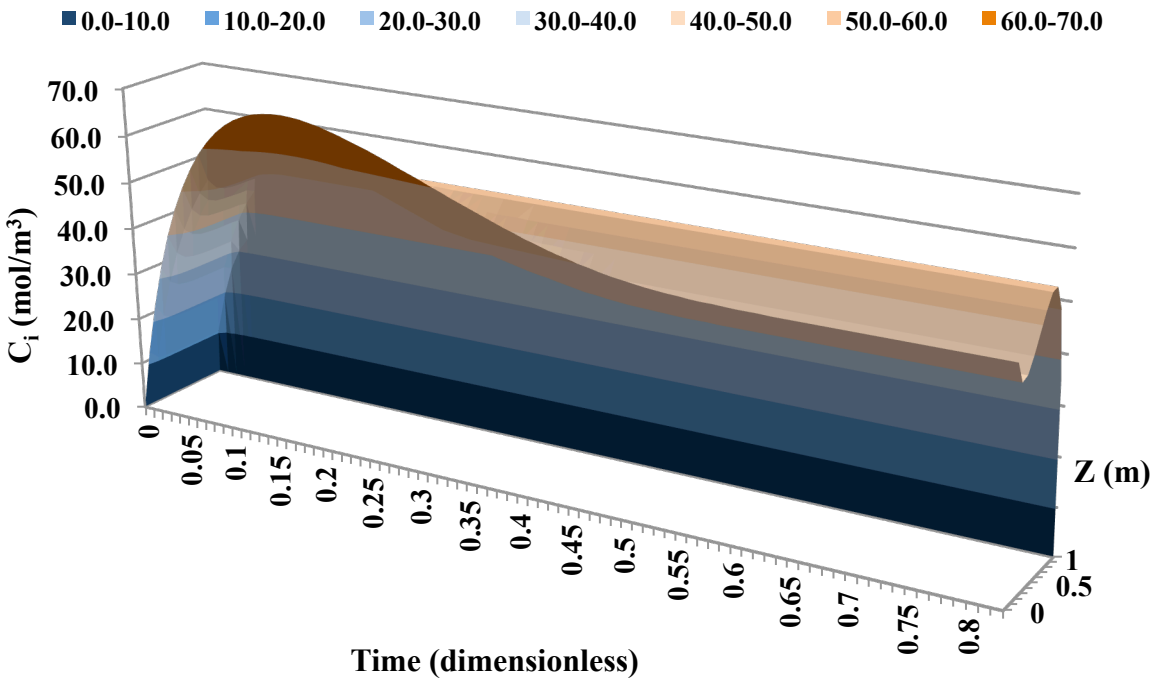

Figure 9. Time evolution of the RNH_3^+ ion axial concentration profile.

Figures 8 and 9 depict the time evolution of the axial concentration profiles of the MEAmide and the MEAmonium ions. These two ions are the products of the chemical reaction given by eq. (8). The mass balance given by eqn. (58) has been satisfied until a relative error value equal to 10^{-5}. Figure 8 depicts the contour plot corresponding to the carbamate ion. We can see that the ion concentration increases with time until reaching a steady-state value. We can also observe that the rate of production is higher at the bottom of the column due to the higher value of the gaseous CO_2 input concentration.

Figure 9 depicts the contour plot corresponding to the RNH_3^+ ion. We can see that the time evolution of the axial concentration profile follows a similar trend to the carbamate ion. However, there is a minimum at the center of the column produced by the presence of reaction 5, which decreases the amount of the ion. In the top part of the column, the ion concentration is very small.

The time evolution of the ternary amine solvent is shown in Figure 10. We can see that the ion concentration reaches a maximum at the top and there is a small decrease due to reaction 7 that leads to formation of $R_1R_2R_3NH+$. The maximum decrease is observed at the top; however, the regeneration of the solvent due to reaction 8 keeps the concentration approximately constant.

In the case of the ternary amine, the mass balance given by eqn. (59) has been also satisfied until a relative error value equal to 10^{-5}. The corresponding mass balance for CO_2 has been satisfied until a relative error equal to 10^{-5}.

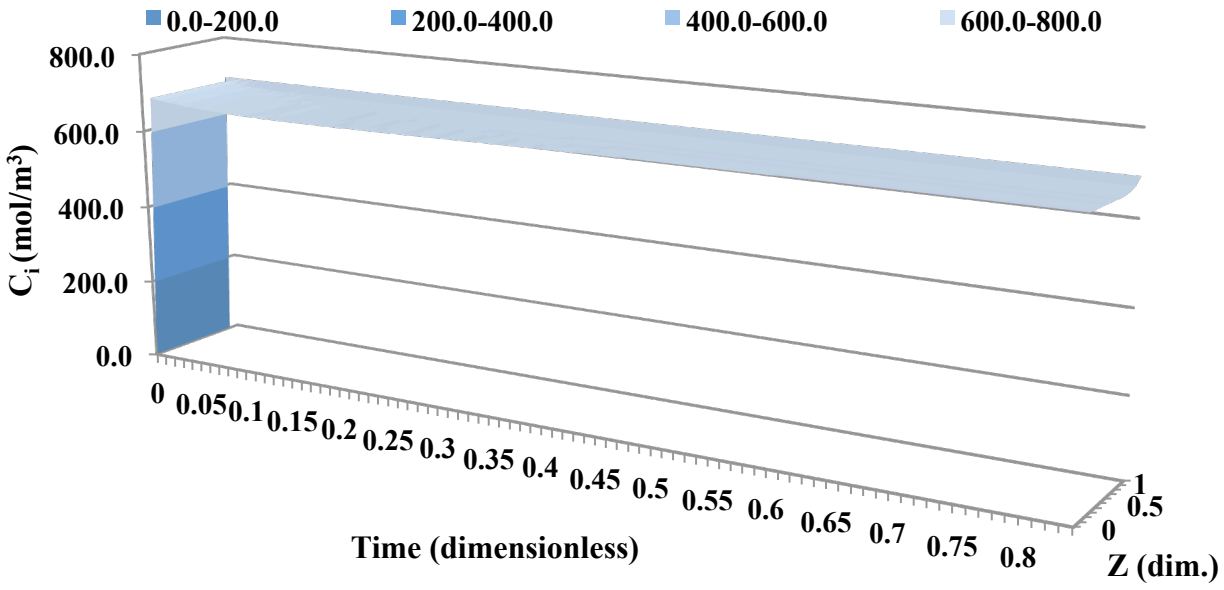

Figure 10. Time evolution of the ternary alkanol amine axial concentration profile.

3.6 Conclusions

A model for the dynamic behavior of reactive CO_2 absorption using alkanolamine solvents has been successfully developed. The model is based upon transient mass and energy balances for several different chemical species commonly present in CO_2 gas-liquid absorption. Phase equilibrium has been considered using a thermodynamic model and through the use of experimentally based Henry's law values. Typical values for the geometric parameters of the absorber and the packing characteristics have been collected. A reaction scheme that takes into account the different reactions between CO_2 and blends of amines in an alkaline environment has been proposed. A computer code has been written to implement the proposed model. The computer code has been properly validated by thoroughly checking all the values of parameters calculated and comparing results to literature data. The mass balances for CO_2 and the alkanol amine solvents have been closed with less than 10^{-4} relative error. Results have been collected and they are logical and agree with equivalent literature results.

3.7 References

Aboudheir, A., Tontiwachwuthikula, P., Chakmab, A., and Idema, R. "Kinetics of the Reactive Absorption of Carbon Dioxide in High CO_2-Loaded, Concentrated Aqueous Monoethanolamine Solutions," *Chem. Eng. Sci.,* **58**, 5195-5210, 2003.

Alatiqui, I., Sabri M. F., Bouhamra W., and Alper E. "Steady-State Rate-Based Modeling for CO_2/Amine Absorption-Desorption Systems," *Gas Separation & Purification*, **8**, 4-11, 1994.

Alvarez-Fuster, C., Midoux, N., Laurent, A., and Charpentier, J. C. "Chemical Kinetics of the Reaction of Carbon Dioxide with Amines in Pseudo m-nth Order Conditions in Aqueous and Organic Solutions." *Chem. Eng. Sci.,* **35***,* 1717-1723, 1980.

Aroonwilas, A., Chakma, A., Tontiwaxhwuthikul, P., and Veawab, A. "Mathematical Modeling of Mass-Transfer and Hydrodynamics in CO_2 Absorbers Packed with Structured Packings," *Chem. Eng. Sci*., **58**, 4037-4053, 2003.

Bedelbayev, A., Greer, T., and Lie, B. "Model Based Control of Absorption Tower for Carbon Dioxide Capturing," *Proceedings SIMS 2008*, Oslo University College, October 7-8, 1420-1440, 2008.

Benamor, A. and Aroua, M. K. "Modeling of CO_2 Solubility and Carbamate Concentration in DEA, MDEA and their Mixtures using the Deshmukh-Mather Model," *Fluid Phase Equilibria,* **231**, 150-162, 2005.

Bosch, H., Versteeg, G. F., and. van SwaaiJ, W. P. M. "Gas-Liquid Mass Transfer with Parallel Reversible Reactions-I. Absorption of CO_2 into Solutions of Sterically Hindered Amines." *Chem. Eng. Sci.,* **44**, 2723-2734, 1989a.

Bosch, H., Versteeg, G. F., and. van SwaaiJ, W. P. M. "Gas-Liquid Mass Transfer with Parallel Reversible Reactions-III. Absorption of CO_2 into Solutions of Blends of Amines." *Chem. Eng. Sci.,* **44**, 2745-2750, 1989b.

Caplow, M. “Kinetics of Carbamate Formation and Breakdown.” *J. Am. Chem. Soc.,* **90***,* 6795-6803, 1968.

Critchfield, J. E. “CO_2 Absorption/Desorption in Methyldiethanolamine Solutions Promoted with MEA and D2EA. Mass Transfer and Reaction Kinetics.” *Ph. D. thesis*, University of Texas, Austin, TX USA, 1988.

Danckwerts, P. V. “The Reactions of CO_2 with Ethanolamines.” *Chem. Eng. Sci.,* **34**, 443-446, 1979.

Donaldson, T. L. and Nguyen, Y. N. “Carbon Dioxide Reaction and Transportation in Aqueous Amine Membranes.” *Ind. Eng. Chem. Fundam.,* **19**, 260-266, 1980.

Freguia, S. and Rochelle, G. T. “Modeling of CO_2 Capture by Aqueous Monoethanolamine,” *AIChE Journal*, **49**, 7, 2003.

Gabitto, J. and Tsouris, C. “Dynamic Simulation of CO_2 Absorption in a Packing Tower.” *AIChE Annual Meeting*, Atlanta, GA, Nov. 11, 2014.

Greer, T., Bedelbayev, A., Igreja, J. M., Pereira Gomes, J. F., and Lie, B. “A Dynamic Model for the De-Absorption of Carbon Dioxide from Monoethanolamine Solution,” *Proceedings SIMS 2008*, Oslo University College, October 7-8, 2008.

Greer, T., “Modeling and Simulation of Post Combustion CO_2 Capturing,” *Ms. Thesis*, Telemark University College, Faculty of Technology, 2008.

Gòmez, C., Borio, D. O., and Schbib, N. S. “Simulation of an Industrial Packed Column for Reactive Absorption of CO_2.” *Latin American Applied Research*, **33**, 201-205, 2003.

Hagewiesche, D. P., Ashour, S. S., Al-Ghawas, H. A., and, Sandall, O. C. “Absorption of Carbon Dioxide into Aqueous Blends of Monoethanolamine and Methyldiethanolamine,” *Chem. Eng. Sci.*, **50**, 1071-1079, 1995.

Haimour, N., Bidarian, A., and Sandall O. “Kinetics of the Reaction between Carbon Dioxide and Methyldiethanolamine.” *Chem. Eng. Sci.,* **42**, 1393-1398, 1987.

Lawal, A., Wang, M., Stephenson, P., and Yeubg, H., “Dynamic modeling of CO_2-absorption for post combustion capture in coal-fired power plants,” *Fuel,* **88** (12), 2455-2462, 2009.

Littel, R. J., van SwaaiJ, and Versteeg, W. P. M.. “Kinetics of Carbon Dioxide with Tertiary Amines in Aqueous Solution.” *AIChE Journal*, **36**, 1633-1640, 1990.

Littel, R. J., van SwaaiJ, and Versteeg, W. P. M.. “Kinetics of CO2 with Primary and Secondary Amines in Aqueous Solution-I. Zwitterion Formation Deprotonation Kinetics for DEA and DIPA in Aqueous Blends of Alkanolamines.” *Chem. Eng. Sci.*, **47**, 2027-2035, 1992.

Littel, R. J., van SwaaiJ, and Versteeg, W. P. M.. “Kinetics of CO_2 with Primary and Secondary Amines in Aqueous Solution-II. Influence of Temperature on Zwitterion Formation and Deprotonation Rates.” *Chem. Eng. Sci.*, **47**, 2037-2045, 1992.

Liu, Y., Zhang, L., and Watanasiri, S. “Representing Vapour-Liquid Equilibrium for an Aqueous MEA-CO2 System Using the Electrolyte Non-random-Two-Liquid Model.” *Ind. Eng. Chem. Res*., **38**, 2080-2090, 1999.

Mandal, B. P., Guhab, M., Biswasb, A. K., and Bandyopadhyaya, S. S. "Removal of Carbon Dioxide by Absorption in Mixed Amines: Modelling of Absorption in Aqueous MDEA-MEA and AMP-MEA Solutions," *Chem. Eng. Sci.,* **56**, 6217-6224, 2001.

Perry R. H. and Green D. W., *Chemical Engineers Handbook. 7th edition*, McGraw-Hill, New York, 1999.

Pinsent B. R. W., Pearson, L., and Roughton, F. J. W. (1956). "The Kinetics of Combination of Carbon Dioxide with Hydroxide Ions." *Journal of the Chemical Society, Faraday Transactions,* **52**, 1512–1520, 1956.

Rangwala, H. A., Morrell, B. R., Mather, A. E., and Otto, F. D., "Absorption of CO_2 into Aqueous Tertiary Amine/MEA Solutions. *AIChE National Meeting*, New Orleans, LA, March 8, 1988.

Sada, E., Kumazawa, H., Osawa, Y., Matsuura, M. and Han, Z. Q. "Reaction Kinetics of Carbon Dioxide with Amines in Non-Aqueous Solvents." *Chem. Eng. J.* **33**, 87-95, 1986.

Sakwattanapong, R., Aroonwilas, A., and Veawab, A. "Reaction Rate of CO2 in Aqueous MEA-AMP Solution: Experiment and Modeling." *Energia Procedia*, **1**, 217-224, 2009.

Usubharatana, P. and Tontiwachwuthikul, P. "Enhancement Factor and Kinetics of CO_2 Capture by MEA-Methanol Hybrid Solvents." *Energia Procedia*, **1**, 95-102, 2009.

Vaidya, P. D., and Kenig, E. Y. "CO_2-Alkanolamine Reaction Kinetics: A Review of Recent Studies," *Chem. Eng. Technol.,* **30**, 11, 1467-1474, 2007.

Van Elk, E. P., Knaap, M. C., and Versteeg, G. F. "Application of the Penetration Theory for Gas-Liquid Mass Transfer without Liquid Bulk Differences with Systems with a Bulk,"*IChemE Symposium Series*, No **152**, 2006.

Versteeg, G. F. and. van SwaaiJ, W. P. M. "Solubility and Diffusivity of Acid Gases (CO_2, N_2O) in Aqueous Alkanolamine Solutions." *Journal of Chem. Eng*., **33**, 29-34, 1988a.

Versteeg, G. F. and. van SwaaiJ, W. P. M. "On the Kinetics between CO_2 and Alkanolamines both in Aqueous and Non-Aqueous Solutions- I. Primary and Secondary Amines." *Chem. Eng*. Sci., **43**, 573-585, 1988b.

Versteeg, G. F. and. van SwaaiJ, W. P. M. "On the Kinetics between CO_2 and Alkanolamines both in Aqueous and Non-Aqueous Solutions- II. Ternary Amines." *Chem. Eng*. Sci., **43**, 587, 1988c.

Versteeg, G. F., Snijder, E. D., te Reile, M. J. M., and van SwaaiJ, W. P. M. "Diffusion Coefficients of Several Aqueous Alkanolamine Solutions." *Journal of Chem. Eng. Data*, **38**, 475-480, 1993.

Versteeg, G. F., Holst, J. V., Politiek, P. P, and Niederer, J. P. "CO_2 Capture from Flue Gas using Amino Acid Salt Solutions," [Online] June 2006 available from *http://www.co2-cato.nl/doc.php?lid=317* accessed [2/04/2015].

Xiao, J., Li, Ch., Li, M. "Kinetics of Absorption of Carbon Dioxide into Aqueous Solutions of 2-Amino-2-Methyl-1- Propanol+Monoethanolamine," *Chem. Eng. Sci.*, **55**, 161-175, 2000.